Carbon-coated nanoparticles and their application in high performance polymer nanocomposites

Submitted by **Nannan Wang** to the University of Exeter

as a thesis for the degree of

Doctor of Philosophy in Engineering

In January 2018

I certify that all material in this thesis which is not my own work has been identified and that no material has previously been submitted and approved for the award of a degree by this or any other University.

Signature: ……..

Abstract

Shrinking down into nanoscale, materials exhibit huge property advantages over their bulk form. New forms of carbon at nanoscale have occupied the prominent position in modern materials research. With a very long history accompanying our human civilisation, carbon as a wonder material has once again contributed to our technological advances, as evidenced by the discoveries and research attractions in the last a few decades. Research into fullerenes (C60, C70, *etc.*), carbon nanotubes (CNTs) and graphene has been continued raising, because of the numerous novel properties associated with these new carbon forms[1-3]. On top of their excellent electronical, physical and chemical properties, CNTs and graphene also exhibit excellent mechanical properties including ultra-high tensile strength, Young's Modulus, as well as high thermal conductivities. Research into carbon has also promoted the flourish of many new non-carbon nanomaterials, and typical examples include the inorganic fullerene-like tungsten disulphide (IF-WS_2) nanoparticles (NPs), numerous oxide NPs and nanowires that also exhibit various remarkable properties, such as high hardness and anti-oxidation stability.

To combine the outstanding performances of both carbon and non-carbon nanomaterials by marrying nanoscale carbon with various metal oxide particles, which forms the backbone of my thesis by carrying out the intensive investigations. In my project it have further validated the advantages of the resulting new carbon-coated NPs in different polymeric matrix composites. The main findings are as follows:

1. A home-made rotary chemical vapour deposit (RCVD) system has been modified and this versatile facility has been applied successfully to

produce different types of graphitic carbon-coated nanocomposite particles, from micro- down to nano-scale, including IF-WS_2, TiO_2, ZnO, Y_2O_3, Cr_2O_3, CeO_2 and ZrO_2 *etc*. The production can be up to 30 g/per batch, which is 10s times more than using a traditional static furnace, by avoiding severe agglomeration.

2. The resulting coating consists of a few layered graphitic carbon with lattice space 0.34 nm. The thickness of the coating is simply controllable between 1-5 nm, depending on the deposition time (10~60 min), precursor injection flow rate (1.2~2.4 ml/L) and heating temperature (700~900 ^oC). Furthermore, the oxide core of ZnO@C was removed by heating under the H_2/Ar atmosphere, and have successfully generated nano- to micro-scale, hollow, closed, and all-carbon structures.
3. The commercial Nylon 12 is applied to fabricate the metal oxide polymer composite. Using ZnO@C-Nylon 12 composite as an example, at 2 wt% content, the composites have achieved with the ultimate tensile strength increased by 27% (from 47.9 to 59.6 MPa), In particular, at 4 wt% content, the ZnO@C showed an impressive improvement in thermal conductivity of nearly 50% (From 0.21 t0 0.31 $W \cdot m^{-1} \cdot K^{-1}$), comparing 16% improvement for ZnO-Nylon 12 composite.
4. Apart from investigations of nylon composite, intensive studies of the Poly ether ether ketone (PEEK), an important high performance engineering thermoplastics polymer, and its nanocomposites reinforced by IF-WS_2 and IF-WS_2@C have been carried out in this thesis. The IF-WS_2/PEEK composites exhibited not only an improvements of 24% (From 77.6 to 96.7 MPa) in the tensile strength (2 wt%), but also showed

an extraordinary increase in thermal conductivity by 190%, from 0.248 to 0.719 $W \cdot m^{-1} \cdot K^{-1}$ at 8 wt%, higher onset decomposing temperatures (54 ^{o}C) against the plain PEEK.

5. Moreover, owing to the better dispersal capacity of IF-WS_2@C NPs, the ternary IF-WS_2@C-PEEK nanocomposites produced in this thesis displayed impressive mechanical properties, increased by 51% (From 77.6 to 120.9 MPa, at 2 wt%), and extremely greater thermal conductivity, with 235% (From 0.248 to 0.831 $W \cdot m^{-1} \cdot K^{-1}$ at 8 wt%), and better stability than the comparison IF-WS_2-PEEK composites. The parameters influencing the coating quality and thickness have also been investigated. Further, their interface studies based on the FTIR and XPS techniques have verified the formation of chemical bonding (C=S bonding and carbon π-π bonding), rather than physically bonded together.

The successful application of the generic RCVD process can be further extended to the processing of many new particles for an ultrathin carbon coating. Considering the vast amount of literature focusing on carbon, the project further processing of carbon-coated materials in composites could easily be tailored to achieve desired surface contacts with different matrices and leading to the better desired performance, as verified in this thesis for the advanced binary and ternary composites. Finally, this research is expecting to expand the application potentials of PEEK-based nanocomposites in critical areas where thermal conductivity and thermal stability are important.

Publications

1. **N. Wang**, Z. Yang, Y. Wang, K. Thummavichai, Y. Xia, O. Ghita, Y. Zhu. (2017). Interface and properties of inorganic fullerene tungsten sulphide nanoparticle reinforced poly (ether ether ketone) nanocomposites, *Results in Physics*, doi.org/10.1016/j.rinp.2017.07.018.
2. **N. Wang**, Z. Yang, K. Thummavichai, F. Xu, C. Hu, H. Chen, Y. Xia, Y. Zhu. (2017). Novel graphitic carbon coated IF-WS2 reinforced poly (ether ether ketone) nanocomposites, *RSC Advances*, 7(56), 35265-35273.
3. **N. Wang**, Z. Yang, F. Xu, K. Thummavichai, H. Chen, Y. Xia, Y. Zhu. (2017). A generic method to synthesise graphitic carbon coated nanoparticles in large scale and their derivative polymer nanocomposites, *Scientific Report*, doi: 10.1038/s41598-017-12200-1.
4. K. Thummavichai, **N. Wang**, L. Lem, M. Phillips, C. Ton-That, H. Chang, C. Hu, F. Xu, Y. Xia, Y. Zhu. (2017). Lanthanide-doped $W_{18}O_{49}$ nanowires: Synthesis, structure and optical properties, *Materials Letters*, Doi.org/10.1016/j.matlet.2017.12.022
5. K. Thummavichai, L. Trimby, **N. Wang**, C. David Wright, Y. Xia, Y. Zhu. (2017). Low temperature annealing improves the electrochromic and degradation behavior of tungsten oxide (WOx) thin films, *J. Phys. Chem. C*, DOI: 10.1021/acs.jpcc.7b06300.
6. F. Xu, T. Kobayashi, Z. Yang, T. Sekine, H. Chang, **N. Wang**, Y. Xia, Y. Zhu. (2017). How the toughest inorganic fullerene cages absorb shockwave pressures in a protective nanocomposite: Experimental evidence from two In Situ investigations, *ACS Nano*, DOI: 10.1021/acsnano.7b02943.

7. Z. Yang, H. Chen, **N. Wang**, Y. Xia, Y. Zhu. (2017). Permeability studies on 3D Ni foam/graphene composites, *Journal of Physics D: Applied Physics*, doi.org/10.1088/1361-6463/aa8078.
8. G. Wu, P. Song, D. Zhang, Z. Liu, L. Li, H. Huang, H. Zhao, **N. Wang**, Y. Zhu. (2017). Robust composite silk fibers pulled out of silkworms directly fed with nanoparticles, *International Journal of Biological Macromolecules*, 104, 533-538.
9. Ahmad, S. Ahmed, T. Subhani, K. Saeed, M. Islam, **N. Wang**, Y. Zhu. (2016). Synergic influence of MWCNTs and SiC nanoparticles on the microstructure and properties of Al_2O_3 ceramic hybrid nanocomposites, *Current Applied Physics*, 16(12), 1649-1658, DOI:10.1016/j.cap. 2016.10.009.
10. F. Xu, **N. Wang**, H. Chang, Y. Xia and Y. Zhu. (2014). Continuous Production of IF-WS2 Nanoparticles by a Rotary Process, *Inorganics*, 2(2), 313-333.
11. G. Song, C. Jiang, **N. Wang**, M. Jiang, J. Nie, G. Ma. (2014). Visible light photopolymerization induced by triazine derivative, *Polymer Science Series B*, 56(5), 577-582.
12. M. Wang, D. Fang, **N. Wang**, S. Jiang, J. Nie, Q. Yu, G. Ma. (2014). Preparation of PVDF/PVP core–shell nanofibers mats via homogeneous electrospinning. *Polymer*, 55(9), 2188-2196.
13. K. Thummavichai, **N. Wang**, Y. Xia, Y. Zhu, (2016). Effect of Low Temperature Treatment of Tungsten Oxide (WOx) Thin Films on the Electrochromic and Degradation Behavior, *2016 IEEE NANO-TECHNOLOGY MATERIALS AND DEVICES CONFERENCE*

Conference Presentation/Poster

1. **N. Wang**, Y. Xia, Y. Zhu. Fabrication and Property Investigation of Inorganic Fullerene Tungsten Sulphide Nanoparticle Reinforced Poly (ether ether ketone) IF-WS_2/PEEK Nanocomposites, *BIT's 3rd Annual World Congress of Smart Materials-2017*, March 2017, Bangkok, Thailand
2. **N. Wang**, Y. Xia, Y. Zhu. Inorganic fullerene tungsten sulphide nanoparticle reinforced poly(ether ether ketone) IF-WS_2/PEEK nanocomposites, *The 23rd Joint Annual Conference of CSCST-SCI*, September 2016, University of Nottingham, UK.
3. **N. Wang**, Y. Xia, Y. Zhu. Synthesis and characterization of novel nanoparticles coated with carbon, *12th International Conference on Material Chemistry (MC12)*, 20 - 23 July 2015, University of York, UK
4. **N. Wang**, Y. Xia, Y. Zhu. A general method to synthesize nano-carbon coated nanoparticles in large scale, *The 21st Joint Annual Conference of CSCST-SCI*, October 2014, University of Surrey, UK

Acknowledgement

It is my great pleasure to say thank you to Prof. Yanqiu Zhu, my best supervisor ever. With his encouragement and inspiration as well as his kind and patient guidance, in the last continuous 4 years, I have learned not only the eligible skills in the field of functional nanomaterials, but also to be optimistic to face life. His strong enthusiasm and deep curiosity really has taught me how to stay inquiring like a baby and always keep calm and use our mind to find out the truth behind each thing. I would also like to appreciate Dr. Yongde Xia, my second supervisor, who gave me many useful and valuable suggestions when I met the challenges in academic research.

Secondly, I wish to thank my friends from our Harrison advanced material research group. Dr. Zhuxian Yang, Dr. Fang Xu, Dr. Binling Chen, Dr. Bahareh Yazdani Damavandi, Dr. Sakineh Chabi, Dr. Yat-Tarng (Tommy) Shyng, Dr. Yuan Wang, Dr. Oluwafunmilola Ola, Dr. Iftikhar Ahmad, Dr. Guiping Ma, Ms Kunyapat Thummavichai, Ms Zheng Huang, Ms Xuan Lu, Ms Ke Bao, Mr Yu Chen, Mr Laicong Deng, Mr Zahid Hussain, Mr Pablo Martinez Pancorbo and many others.

I would like to take the opportunity to thank Prof. Oana Ghita and Dr Luke Savage, who are from “Exeter Advanced Technology” centre (X-AT), for their constant technical support of my project.

I also wish to thank Dr. Hong Chang from Harrison building imaging suite and Prof. Xianghui Hou’s group from University of Nottingham for their valuable help in various material characterisation support, including TEM, SEM, XRD, AFM and XPS etc.

Last but not least, I will show my deepest gratitude to my parents for their selfless love to me and the good care of me from my childhood. Without they gave me the life and full support, I would have no chance to be here to see how wonder this world is. Many Thanks again!

Table of Contents

List of Figures

List of Table

List of Symbols and Abbreviations

0D	Zero-dimensional
1D	One-dimensional
2D	Two-dimensional
2θ	2 theta (degree)
2H-WS_2	Two-layer hexagonal WS_2
3D	Three-dimensional
Ar	Argon
AFM	Atomic force microscopy
AIBN	2,2'-Azobisisobutyronitrile
BET	Brunauer-Emmett-Teller
BSE	Back scattered electron
C	Carbon
Cr_2O_3	Chromium oxide
CeO_2	Cerium oxide
Co_3O_4	Cobalt oxide
CNTs	Carbon nanotubes
CNP	Graphene
CVD	Chemical vapour deposition
DSC	Differential scanning calorimetry
DVB	Divinylbenzene
DMAA	N,N-dimethylacrylamide

EDS	Energy-dispersive X-ray spectroscopy
FWHM	Full width half maximum
FTIR	Fourier-transform infrared spectroscopy
H_2	Hydrogen
H_2S	Hydrogen sulphide
HRTEM	High-resolution TEM
HV	Vickers hardness testing
IF	Inorganic fullerene-like particle
INT	Inorganic nanotube
IF-WS_2	Inorganic fullerene-like WS_2
JCPDS	Joint committee on powder diffraction
N_2	Nitrogen
NH_3	Ammonia
NWs	Nanowires
NPs	Nanoparticles
MS_2	M=Mo or W, including MoS_2 and WS_2
MX_2	M=Mo or W, X=S, Se *etc.*
MO_X	TiO_2, ZnO, Y_2O_3, Cr_2O_3, CeO_2, ZrO_2 *etc*.
MO_X@C	Carbon coating metal oxide particles
PA 12	Polyamide 12 (Nylon 12)
PEEK	Poly ether ether ketone
PMMA	Polymethylmethacrylate
PS	Polystyrene
PVD	Physical vapour deposition

S	Sulphur
St	Styrene
SE	Secondary electron
SEM	Scanning electron microscopy
TC	Thermal conductivity
TEM	Transmission electron microscopy
TGA	Thermogravimetric analysis
TiO_2	Titanium dioxide
UV-Vis	Ultraviolet–visible spectroscopy
W	Tungsten
WS_2	Tungsten disulphide
WNx	Tungsten nitride
WOx	Tungsten oxide
WOxNy	Tungsten oxynitride
XPS	X-ray photoelectron spectroscopy
XRD	X-ray diffraction
Y_2O_3	Yttrium oxide
ZrO_2	Zirconium dioxide
ZnO	Zinc oxide

Chapter 1. Introduction

As the rapidly development of nanoscience and nanotechnology, further modification and reinforcement of conventional functional materials become available. Especially the carbon based materials have attracted a large amount of interests in the last few decades and the related research will be further enhanced in the near future.

The aim of this project is to investigate the principles and features of nano carbon materials and novel nano-onion inorganic NPs to be a particularly filler in composite reinforcement. With the particle size going down to 100 nm, the carbon materials will show the extremely different promoting potential properties apart from their bulk form, due to the negligible quantum effect becoming essential factor in nanomaterials. For example, the zero-dimensional (0D) materials like different kinds of tiny nanoparticles, fullerene, graphene quantum dot (C60, C70) and carbon-tube cluster[4-7]; the one-dimensional materials (1D) carbon nano-tube (CNT) and nanowires[8-10]; the two-dimensional (2D) nanosheets such as the hottest material graphene (GNP) like structure, borophene and metal dichalcogenides and three-dimension (3D) nano porous/sphere[11-16], displayed the attractive changes in both physical and chemical properties. Metal oxide and the carbon based material are the most common and economical use materials to strengthen the polymer matrix[17-21]. And then the most efficient method to combine the advantages from both metal oxide and carbon is to fabricate the ternary composite, by using the nanoparticles of metal oxide and nano-carbon[22]. However, even the binary nanocomposite is not easy to achieve, the ternary nanocomposite is significantly complex in theoretical and practical operation. Hence, it is necessary to develop an efficient and effective in a simple way to synthesize this kind of ternary nanocomposite in large scale.

In the present thesis, we also reported one famous 0D material - inorganic fullerene like tungsten disulphide (IF-WS_2), a typical metal dichalcogenides

showed MX_2 type (M=W, Mo and X=S, Se *etc.*) ,which was been successful synthesized by Tenne *et al*[23]*.* in 1992 and also explored the potential application as the super solid lubricant with its extraordinary structure[24]. Their significant tribological and mechanical properties hence are promising potential to prepare the new high performance nanocomposite[25-27]. However, there are diverse approaches to synthesize the WS_2 and the WS_2 has different classes of structure such as 1T, 2H and INT[28]. Therefore, it is the challenge to enlarge the production of IF-WS_2 nanoparticles to meet the application requirement of commercial high performance composite. Moreover, the recent existing method created by Tenne is remained complicating technique problems to produce the continuous synthesis process and still need the effective solution to utilize the HsS gas.

The research objectives are: to prepare the nano carbon reinforced metal oxide composites; to develop a simple, versatile, efficient and large-scalable technique to continuously produce IF-WS_2 and its derivative C-coating NPs and to fabricate the related high performance PEEK composites[29-31]. And further intense investigations for the IF-WS_2 and its related derivative IF-WS_2@C nanoparticles reinforced poly ether ether ketone (PEEK) high performance polymer nanocomposite have been done and focused on their great mechanical property enhancement, incomparable thermal conductivity and stunning tribological performance[32].

This thesis contains seven main chapters. Chapter 1 introduces the overall innovation, inspiration and motivation of this thesis and the project objectives. Chapter 2 provides the comprehensive background and literature review of metal oxide/carbon reinforced nanocomposites, mechanism of synthesis of IF-WS_2 and the fabrication of their derivative high performance polymer nanocomposites. Chapter 3 briefly describes the property characterisation techniques and the experimental processing in this project. Chapter 4 demonstrates the modified experimental technique for the general method of

nano-carbon coating via the chemical vapour deposition (CVD) technique. And Chapter 5 releases the related verified experiment of C-coating metal oxide nylon composite. Chapter 6 presents the reaction factors and mechanisms of forming the IF-WS_2 nanoparticles and the formation of IF-WS_2/PEEK binary high performance nanocomposites. Chapter 7 further investigates the novel synthesis procedure of IF-WS_2@C and its mechanisms and properties and studies the fabrication and property characterisations of IF-WS_2@C-PEEK ternary nanocomposites. Finally, chapter 8 ends with the conclusions of the thesis and the recommendations for future work in related research areas.

Chapter 2. Background and Literature review

Part-I Nano-carbon coating metal oxides (MO_x@C) and their reinforced nanocomposites

In an effort to combine the advantages of the chemical and physical properties of both carbon and non-carbon nanomaterials, a lot of investigations has been carried out by bonding the nanoscale carbon with numerous metal oxide particles, such as TiO_2, ZnO, ZrO_2, Y_2O_3, CeO_2, Co_3O_4 and *etc*[33-39]. The new composite particles indeed showed outstanding mechanical, thermal and electrical properties. Generally, three types of such carbon-metal oxide structures can be classified, including carbon shell coating the particles, carbon-metal oxide blending with each other, and carbon core structures[40, 41]. In addition, when sizes of the materials go down to nanoscale, quantum effects would result which makes the combination of carbon and metal oxide nanocomposites more interesting[42]. Further numerous investigations have been focused on reporting the metal oxide- or carbon-reinforced polymer matrix composites, and their improved mechanical properties, pointing to many promising applications. Based on the separate successes in metal oxide- or carbon-reinforced polymer matrices, the carbon-coated metal oxide composite nanoparticles, as a core-shell structured reinforcement, could lead to intrigue potentials for the development of high performance polymer nanocomposites, which has not been investigated previously[19, 21, 43, 44].

2.1 Nano-carbon reinforced metal oxide nanocomposites

Carbon exists as many different allotropes because of the flexible chemical valence available in its structures, of which the most famous nano-carbon forms are fullerene (0D), carbon nanotubes (1D) and graphene (2D), which exhibited extraordinary electronic, optical, thermal and mechanical properties[45-49]. These carbon nanomaterials are also considered as extraordinary additives that are used to prepare supercapacitor and battery electrodes, nanodevices and composites[50-54]. Meanwhile, metal oxide materials have been continuously investigated for a long time. On one hand, research has been focused on the fundamental studies about the potentials of various oxide in catalysts, sensing, semiconducting and corrosion/oxidation protection[55-58]. On the other hand,

investigations have concentrated on practical applications in high performance composites, based on the intrinsic properties of specific oxides, such as the superior hardness, excellent thermal resistance and high chemical stability[59-63]. During the past few decades, the rapid development of nanotechnology brings in new research for the metal oxides, endeavouring to discover and explore their functionalities[64-67].

Effectively joining carbon and metal oxide could be a logical way to combine and realise the advantages of both materials. We will summarise the various techniques that have been reported for the fabrication of such composite particles, as follows.

Typical existing carbon reinforced metal oxide composites (Coating, Hybrid /Mixed and Cored)

A wide range of choices for the carbon-based materials is available for the creation of C-metal oxide composite particles, including activated carbon, graphite, fullerene, CNTs and graphene[68-72]. The coating strategy has been successfully used to synthesise composite particles. For example, Inagaki *et al.* who first produced a controllable thickness of polyvinylchloride (PVC) outside the target particles and then treated them at high temperature over 1000 ^{o}C to form an activated carbon coating mixture[73]. This is an easy and commonly used method for the preparation of carbon-ceramic particles in large scales. However, the PVC coating showed some localised shrinkages during the hot treatment process, and normally ended up with non-uniform coatings. Further, the pyrolysis of PVC as a carbon source made the thickness of the coating on the particles uncontrollable, because the amount of carbon surrounding the target particles and the rational structure of the final products are unpredictable. As shown in Fig. 2.1, the black patterns in the HRTEM show theTiO_2 nanoparticles coated with a thin carbon layer, however the uneven lattice patterns of carbon demonstrate that the coating is amorphous and carbon residues are remaining within the sample.

By using a modified arc-discharge generator, multi-layered carbon coating on the outer surface of a metal/metal oxide was produced by using the arc-evaporation method, which was first introduced by Saito and his co-workers in

1994[74]. In the arc-evaporation technique, accurate and uniform graphical carbon nano-capsules were resulted, however the appearance of space between the carbon coating and oxide nanoparticles had revealed the poor bonding between them, which can be obviously found on the top part of the particle in Fig. 2.2. Although the mechanical property of these particles are not high enough because of the potential of collapse subjecting to large external loading, this sort of graphitic carbon cages and the core crystal structure has a great potential for applications in catalyst, capacitors and in polymer composites as a supporting filler.

Graphene is a single layer of carbon atoms with all sp^2 bonding forming a honeycomb structure[11], and it is the newest advanced material that intensively investigated in the past decade. Graphene-reinforced metal oxide composite has exhibited great potentials as electrode materials and catalyst, in the construction of optical device and supercapacitor, and for energy storage applications. Very recently, the graphene-coated metal oxide hybrids were reported by Su *et al.,* and they have demonstrated them as a promising anode material for super-battery with enhanced lithium storage[75]. The hybrid 2D core-shell structures have shown very good electric conductivities, shown in Fig. 2.3. The uniformly sized nanoparticles are inserted into the carbon membrane with part of their surfaces exposed which make them suitable for electric applications. However, due to the coating is not continuous, this sort of sheet structure is instable, thus is unsuitable for applications in composite aiming to improve the strength.

CNTs and fullerene are the two star materials prior to graphene, and both have intriguing electronic, chemical and mechanical properties. Since Sun *et al.* developed the metal oxide nano-coating deposited outside the CNTs in 2007 by using a sol-gel technique, in Fig. 2.4 shown the very thin nano-caoting of Ce_2O_3[76]. Banerjee *et al.* produced single-walled CNT-reinforced TiO_2 nanoparticles via an amide-forming reaction[77]. Furthermore, Ajayan *et al.* reported a method of using CNT templates to grow V_2O_5 and formed a metal oxide coated CNT composite[78]. Moreover, Satishkumar *et al.* had further expanded the applicable metal oxide range for the preparation of many metal oxide nanorods or nanotubes by using CNTs, such as WO_3, MoO_3, Sb_2O_5,

MoO_2, RuO_2 and IrO_2, with a reasonably high production yield and displayed the clear boundary of coating of metal oxide respectively[79]. Fig. 2.5 shows a different metal oxides coating on a CNT, and the shape of the bonding edge demonstrates that the coating is not damaged. This method widened their potential applications in supercapacitors. Cox *et al.* have recently shown the creation of isolated single and multi-layered fullerenes sheathing MgO particles, respectively[80].

Compared with the large number of literatures of CNTs and graphene, reports on metal oxides are fewer for their uses in composites, and this limitation increases the workload for the preparation of advanced composites. A critical review on the dispersal ability of metal oxides in different solutions is highly desirable, to offer guidance for researchers to work efficiently to achieve a uniform dispersion in composites. The highly sensitive and selective adsorption features of a dispersal suspension to certain organic micro-molecules such as ethanol and acetone can be used as an indicator of the dispersal quality.

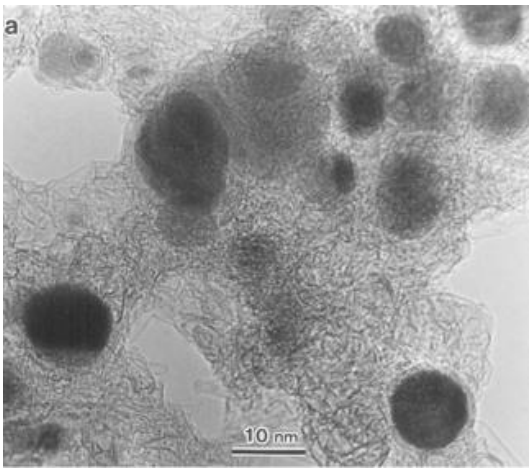

Fig. 2.1 The core-shell coating by carbonization of PVC[73]

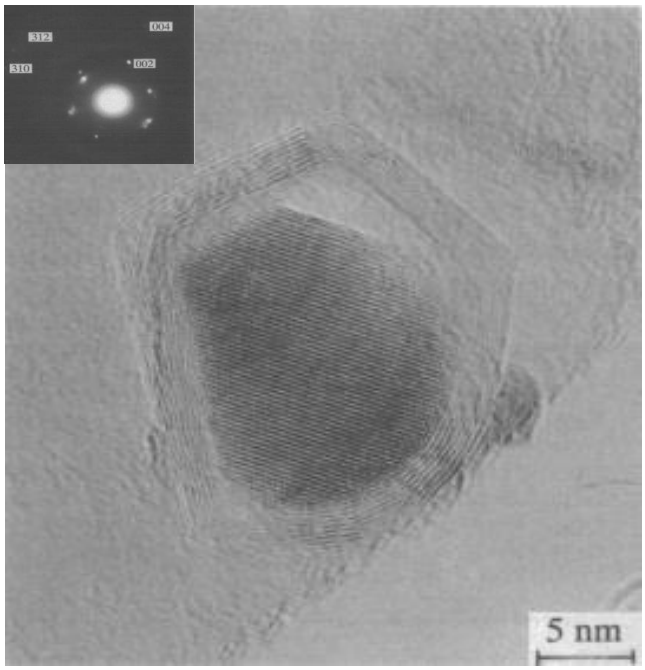

Fig. 2.2 Carbon coating prepared by the arc-evaporation method[74]

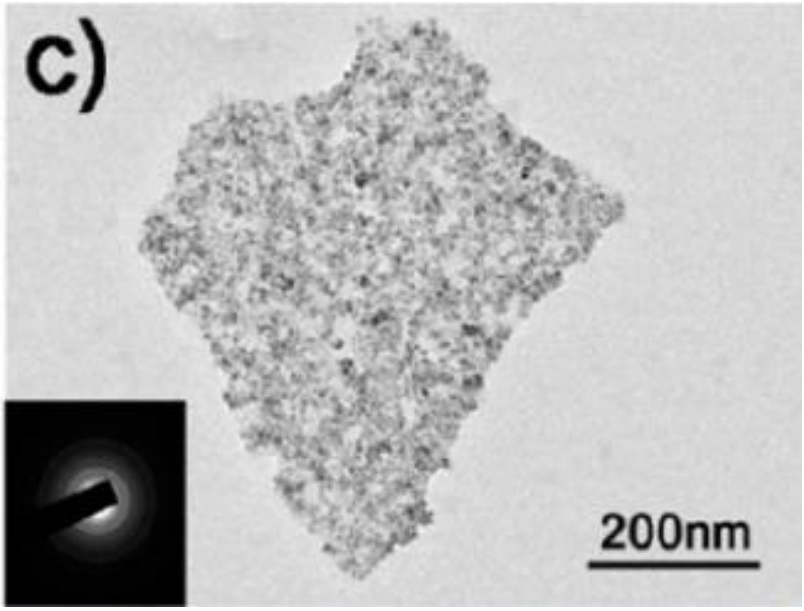

Fig. 2.3 2D core-shell structure[75]

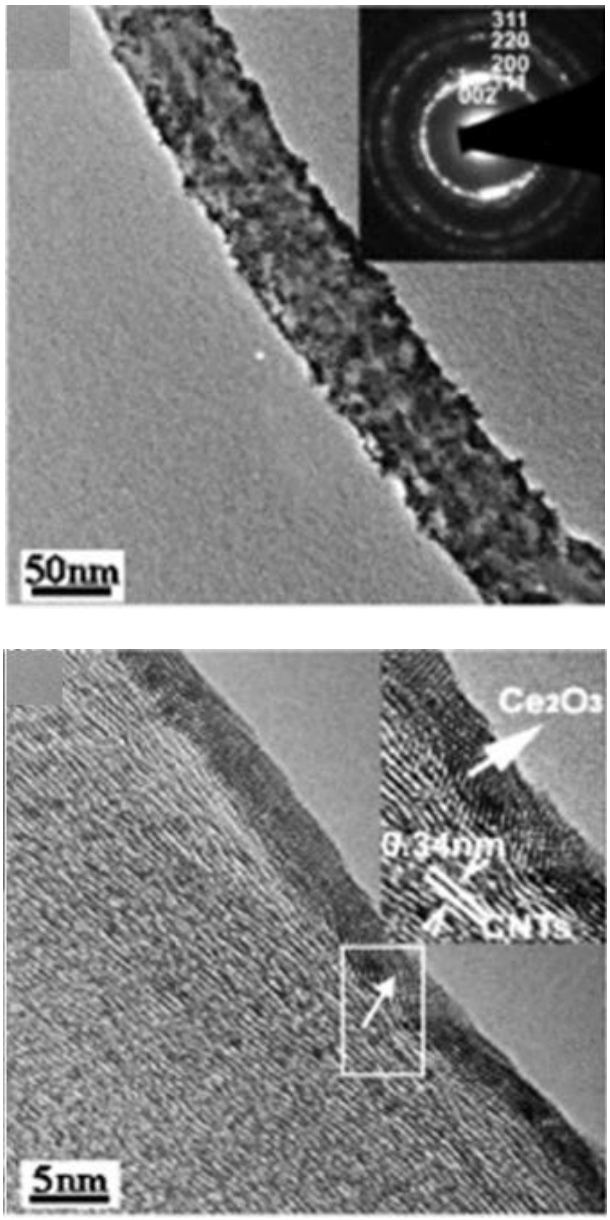

Fig. 2.4 Nano-layer of Ce_2O_3-coated CNTs[76]

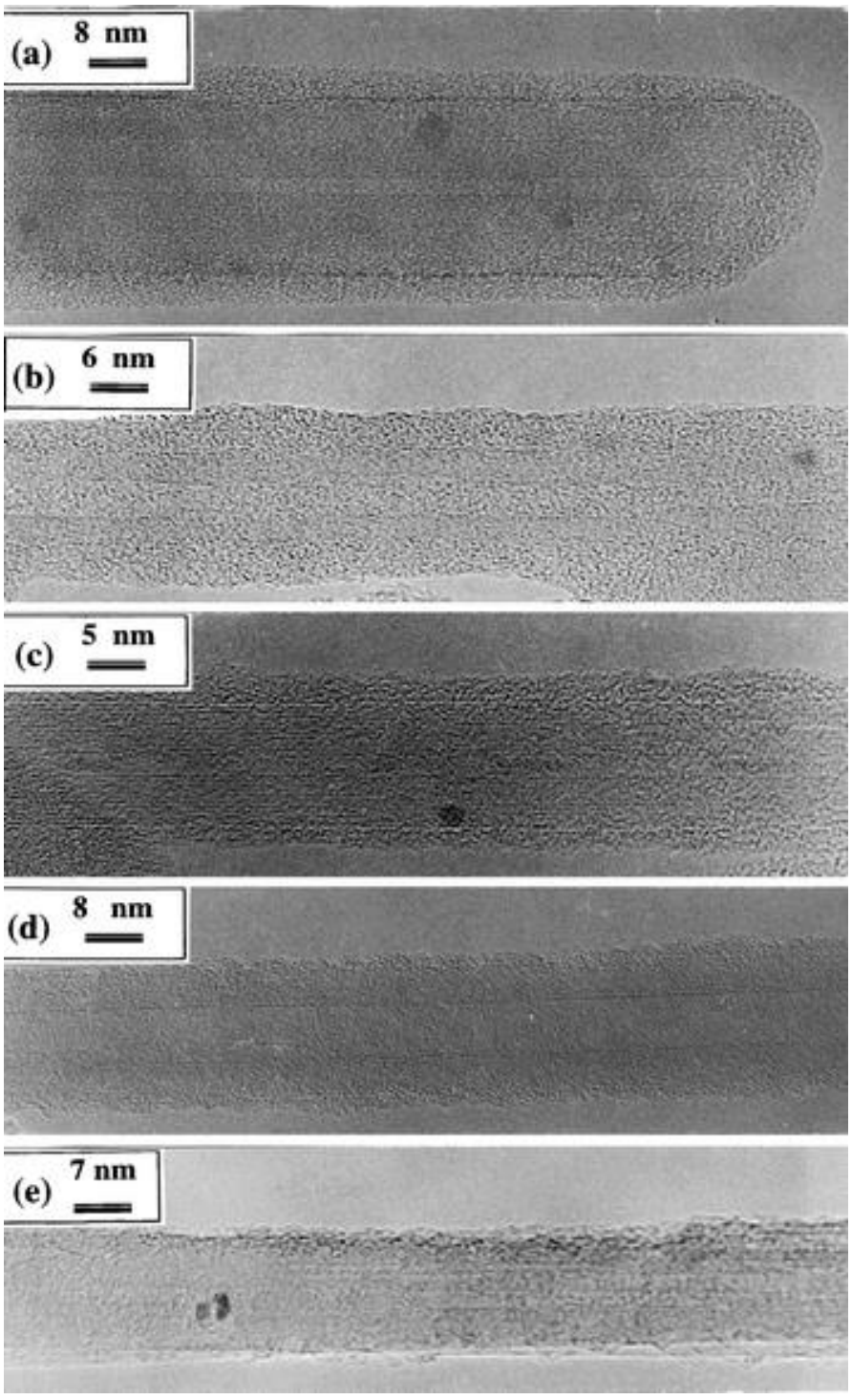

e. (a) V_2O_5, (b) WO_3, (c) MoO_3, (d) RuO_2 and (e) IrO_2 coatings of CNT

Fig. 2.5 Various carbon-reinforced metal[79]

2.2 Metal oxide-reinforced polymer nanocomposites

Within the last two decades, the geometric dimension of many materials went down below 100 nm, which allowed the composite engineering to gain an increased attraction by tailoring various forms of new materials. Promoted by this advance, polymeric nanocomposites reinforced by nanofillers indeed showed promising physical, chemical and mechanical properties[81-86]. As a result, the composites can be used in microelectronic actuators and sensors, electrolytes, anodes and biomedical scaffold[87-91]. To some extent, the properties of a polymeric matrix composite are defined by the type of reinforcing fillers, which include the sizes and intrinsic properties of the fillers. Therefore, developing new nanofillers with favourable features for dispersion and bonding with the matrix is of highly importance for composite engineering.

2.2.1 Fabrication of metal oxide nanoparticles reinforced polymer matrix

Generally, the composite preparation can be separated into two big sections, ex-situ and in-situ processes respectively. In this part, we will briefly introduce the most important fabrication method for the formation of polymer matrix nanocomposites.

2.2.1.1 Ex-situ processing

The most commonly used method to fabricate composites is the ex-situ process. As shown in Fig. 2.6, this typical synthesis starts from preparing the filling nanoparticles in the external step which are then transferred into or mixed with the monomer completely by using stirring and sonication treatments, or with the aid of surfactants in order to achieve a uniform dispersion[92]. The final synthesis step is typically the polymerization processing[93]. The strategy for this ex-situ method is to prepare the molecular precursor first and fabricate the bulk sample at the end. This technique is suitable for processing soluble or monomer polymers.

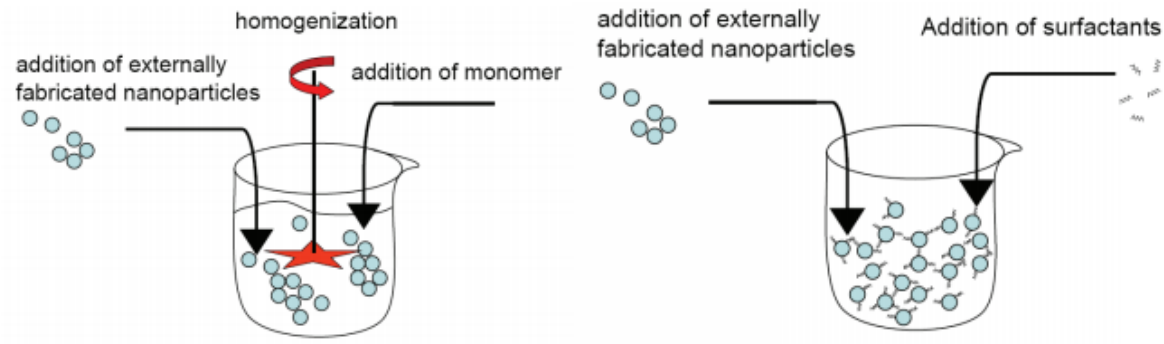

Fig. 2.6 Sketch diagram of the dispersing of ex-situ process[92]

In this case, the most difficult challenge is to reduce the agglomeration of nanoparticles. The general low-cost physical methods are stirring or sonication, and this simple mixing is also capable of forming batched mixtures as a precursor. Aided with surface chemical modification, the results could be better. Musikhin *et al.* prepared luminescent polymer composites using various surface functionalized Y_2O_3, ZnO, Sb_2O_3 and SnO_2 nanoparticles[94]. Blending with the nanoparticles and monomer directly can also lead to uniform polymer composites by tailoring different polymerization treatments. Wang *et al.* used an electron irradiation approach to form the TiO_2-reinforced polymer nanocomposite[95]. Zhang *et al.* applied a plasma polymerization process to obtain a core/shell polymer-coated ZnO composite[96]. Compared Wang *et al.* utilised a plasma induction technique to deposit a thin film of polymer with ZrO_2 filler.

Although the ex-situ approach is widely used to fabricate polymeric composites, its drawback is also obvious, as the composites normally suffer from severe particles agglomeration at moderately high load. The agglomeration and uneven particles distribution restrict the full property gains of the composites, and the filler loading is generally low especially for solvent-free composites.

2.2.2.2 In-situ processing

The in-situ method can also be considered as physical and chemical methods, respectively.

a.Physical in-situ method

The common features for physical in-situ method are to prepare the encapsulated nanoparticles without chemical reactions being involved. The physical in-situ approach allows for the precursor to change or modify the surface of particles with organic coating — the encapsulation compounds. A general system has been established by Vollath *et al.* to combine the plasma and microwave techniques for the creation of hybrid core/shell structured nanocomposites[97]. The principle of this method is using the microwave energy to activate the volatile ceramic cores, thereby forming the polymer coating shell via the UV of the plasma, as displayed in Fig. 2.7 on the left synthesis part, where the small organic compounds were polymerized together to form the coating. However, even the first step is purely a physical process (microwave), the UV treatment process for the polymerization still involves some chemical processes.

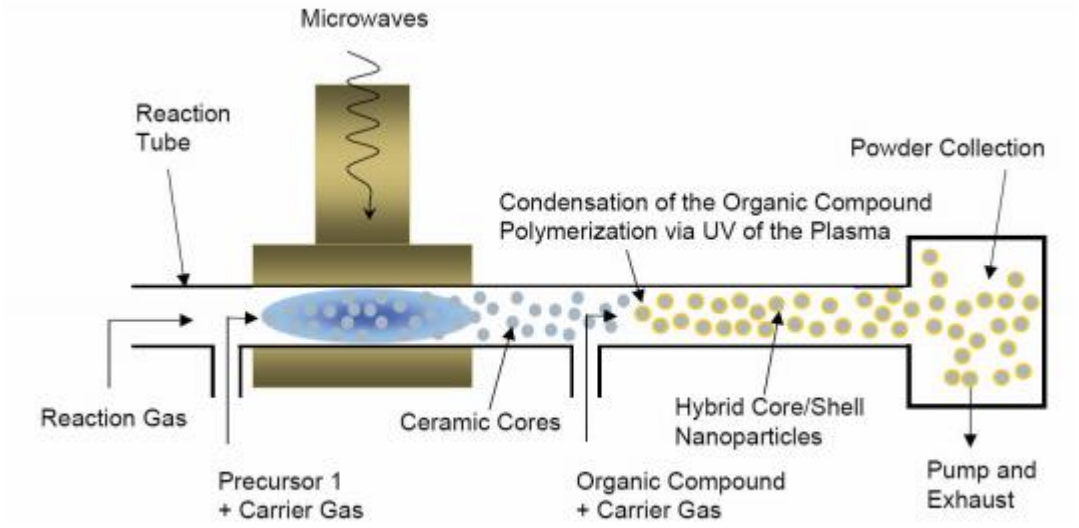

Fig. 2.7 A Sketch of the microwave/plasma system[97]

This kind of physical vapour deposition (PVD) can also be applied to form an in-situ polymer coating on nanoparticles. Because of lacking chemical bonding, the coating was normally deposited based on weak physical bonding, and the resulting samples however showed a uniform coating. Traditional microwave plasma can be replaced by the PVD technique. Srikanth *et al.* developed a one-step microwave/plasma reactor[98]. And Qin *et al.* improved the system and applied a dual-plasma processing[99]. The target particles could be deposited

with an organic compound coating via arc evaporation and plasma polymerization[100].

b.Chemical in-situ method

Apart from the physical method, chemical in-situ method is focusing on solvent-based reactions, through which nanocomposites are fabricated. Althues *et al.* published a comprehensive review that introduced a variety of chemical in-situ synthesis approaches[101]. By realizing Fe_2O_3 nanoparticles into the cross-linked resin, Ziolo *et al.* developed a one-step method to disperse the particles within a polystyrene matrix by ion-exchange between the resin and iron-chloride water solution[*102*]. Recently, hydrothermal/solvothermal in-situ one-pot methods were also widely reported for the creation of core/shell nanocomposites. For example, the Fe_3O_4/PMMA nanocomposite with great superparamagnetic property was synthesized by Cao *et al.*[*103*] Although numerous research groups have investigated the hydrothermal method, only a few studies was focused on bulk polymers. Furthermore, Guan *et al.* reported a bulk sample of ZnS-reinforced polymer composites, and achieved an amazing transparent property as shown in Fig. 2.8a and their HRTEM is also displayed in Fig.2.8b[*104*]. The ZnS NPs were mixed with some kinds of monomers like DMAA (N,N-dimethylacrylamide), St(Styrene), DVB(Divinylbenzene), *etc.* and after the heating AIBN (Azobisisobutyronitrile) treatment process, the surface modified ZnS NPs were formed inside the polymer matrix. The HRTEM image of ME@ZnS NPs shows the homogenous distribution of ZnS in the polymer matrix.

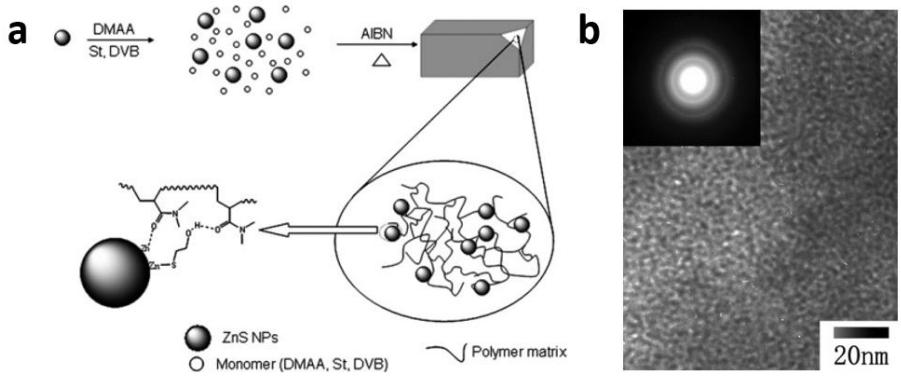

Fig. 2.8. Sketch of the preparation process of ME@ZnS nanoparticles, and b. TEM and SAED pattern of the ME@ZnS nanoparticles[*104*]

Owing to its versatile and controllable features, the sol-gel method is emerging as and becoming a common route for the in-situ synthesis of nanocomposites or hybrid nanoparticles from 1971, in which both filler nanoparticles and the resin matrix can be formed at the same time[105]. Fendler *et al.* prepared an iron colloidal solution first, and then mixed it with polypyrrole (PPy)[106]. After the polymerization process, a uniform nanocomposite was achieved, which has great potentials as a range of electro-conductive polymer composites. Chang *et al.* reported an in-situ sol-gel spin coating method[107]. By using PMDA-ODA/SiO_2 and the polyamic acid, they prepared a polyimide-silica hybrid nanocomposite thin film. In addition, Xiong and co-workers modified this method by controlling the water content and pH values, and they obtained an organic–inorganic hybrid resin by mixing the TiO_2 sol and dissolved acrylic resin[108].

After the precursor synthesis process, re-agglomeration can still occur owing to the Van der Waals attraction of molecules[109]. The main challenge in nanocomposites preparation is to obtain a good dispersion of fillers into the matrix and a strong bonding between them. Although numerous investigations have attempted to eliminate this issue, only a few highly successful reports have been documented for high filling contents in nanocomposites. The other challenge is to disperse the nanoparticles into different polymer matrix with homogeneous distributions, and also to achieve an highly even polymeric crystallization structure with good interfaces.

2.3 Carbon materials reinforced polymer nanocomposites

Polymers and their derivative carbon reinforced polymeric composites have been applied in many industrial sectors, including airplane, motor-vehicle, aerospace, industry, biomedical prosthesis, structure supporting and infrastructure materials[110-114]. This originates from their high specific tensile strength, light-weight and extraordinary durability *etc*. Various CNT-reinforced polymer composites have been studied before, such as epoxy (Bal *et al.*), thermoplastics (Coiai *et al.*), gels (Liu *et al.*) and poly(methyl methacrylate)(PMMA) (Yeh *et al.*)[115-118]. We summarised the recent advances in this area.

2.3.1 CNT-reinforced polymer nanocomposites

Since Iijima et al. found the CNTs in 1991, CNTs became the star materials, owing to their amazingly high mechanical and electrical properties[8]. And the Ajayan *et al.* first had reported CNTs reinforced polymer composites in 1994[119]. Meanwhile, there are two types of CNTs, single-walled nanotubes (SWNTs), a single graphitic carbon sheet wrapped into a cylindrical hollow tube, and multi-walled nanotubes (MWNTs) consisting of a stack of concentric SWNTs, respectively, as shown in Fig. 2.9[120].

Inside a CNT, all the carbon–carbon bonds are sp^2-hybridized, which possesses a nearly defect-free structure of the carbon atoms. The π-π bonding between adjacent carbon atoms demonstrated a very high tensile strength, stiffness, as well as high electric conductivity, which have been confirmed by both experimental studies and theoretical simulations.

There are two main mechanisms for the fabrication of CNT reinforced polymer composites:

a) Physical bonding (Weak Van der Waals bonding)

b) Chemical bonding (Surface modification of the CNT adhere to polymer matrix)

A wide range of studies has concentrated on utilizing CNTs as a filler in polymer composites, and the results have shown a substantial improvement in the thermal conductivity, anti-corrosion resistance and most of the mechanical properties including tensile strength, elasticity, hardness and Young's modulus, although the toughness and ductility have been reported to reduce in some cases. The ultrahigh electric conductivity of CNTs offers the opportunity for high electrical conductive polymer matrix, especially with aligned CNTs along certain directions. At much lower CNT loadings in polymer composites than conventional conductive fillers, the new composites showed great potentials for applications in electrostatic protection, shielding electromagnetic field, and engineering where specific conductive polymer are needed.

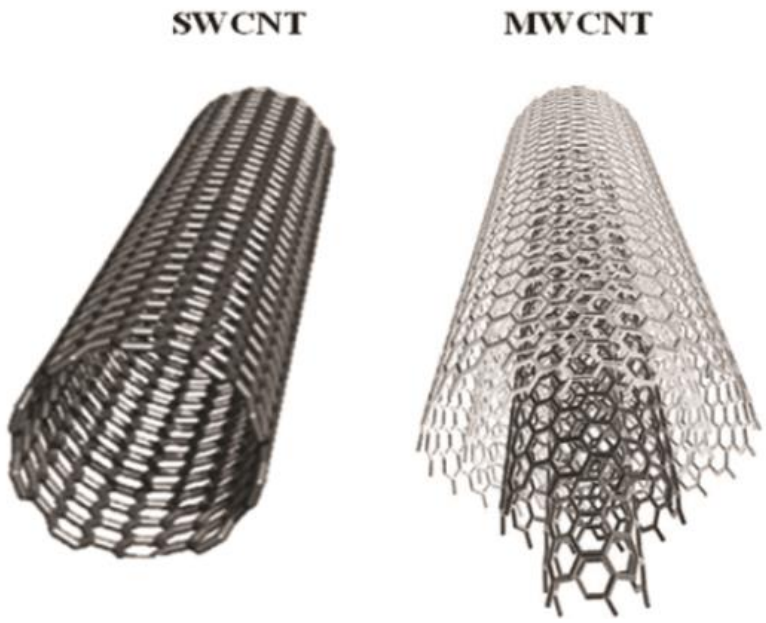

Fig. 2.9 Structure of a SWNT and a MWNT[120]

2.3.2 Carbon@NPs reinforced polymer composites

Recently, carbon membrane material, especially graphene, has attracted remarkable attentions because of its outstanding mechanical, electrical and thermal properties that the carbon coated NPs reinforced polymer ternary composites therefore quickly became a hot subject of research[121].

Because of the efficiency produce the graphene by mechanical exfoliated method or CVD synthesis method is low. And both techniques are not viable for composite fabrication[122-125]. A typically saleable procedure to produce graphene has been derived from the graphene oxide reduction method. As shown in Fig. 2.10a, the isolated GO flakes were introduced into the polymer matrix, further by reduction process to form the rGO inside the polymer matrix. Fig. 2.10b. the in-situ images corresponding to the sketch of fabrication process. Fig 2.10c. the EBSD pattern for the rGO/PVDF nanocomposite[126]. The thickness and lateral dimensions of the resulting graphene are highly depending on the use of appropriate approaches. Several methods have been described, such as rapid heating, microwave or sonication treatment after acid washing procedure. These types of graphene are low in electric conductivity compared with other types of graphene, however they offer a practical solution for their large-scale applications in composite fabrications.

Similar to CNT-reinforced polymer nanocomposites, the graphene-reinforced polymer nanocomposites are also based on two main mechanisms.

a) Non-covalent bond with in-situ polymerization (Non-covalent dispersion methods)

b) Covalent bonds (Graphene Oxide (GO) bonded with the polymer matrix)

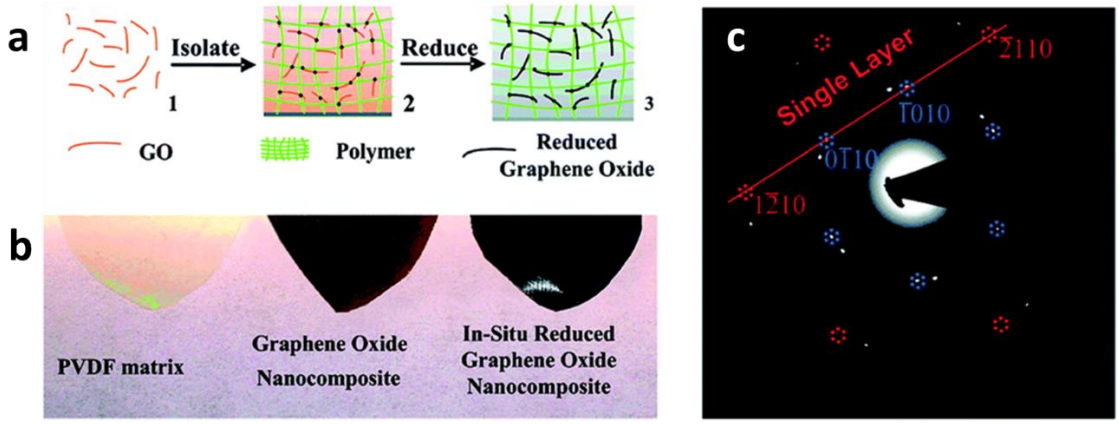

Fig. 2.10 a) Scheme of compositing process of in-situ polymerization bond with rGO (Isolated GO flakes were introduced into the polymer matrix, further by reduction process to form the rGO inside the polymer matrix); b) the in-situ images corresponding to the sketch of fabrication process; c) the EBSD pattern for the rGO/PVDF nanocomposite[126]

In this project we applied the novel nano-onion structure material IF-WS_2, the special carbon coating technique and the high performance polymer PEEK together to make the new ternary polymer nanocomposite.

2.3.3 Limitations and challenge

Both CNT- and graphene-reinforced polymer nanocomposites are believed to be the promising material for future engineering. However, there still various challenges need to be tackled. On one hand, the interface interactions between the polymer and filler need more direct investigations to elucidate what exactly happens and to achieve the ideal interface structure. On the other hand, agglomerates or bundles of nanofiller, such as CNTs and graphene, may severely limit the full improvement potentials for the composites in their performance. In order to counter these two challenges and to optimize the

properties of polymer nanocomposites, improvements of dispersion and proper surface functionalization require further investigations.

Part-II Inorganic fullerene tungsten sulphide (IF-WS_2) and polyetheretherketone (PEEK) nanocomposites

2.4 Structures of metal dichalcogenides nanoparticles

2.4.1 Crystal structure of layered WS_2

Recent reports have shown that different sorts of metal dichalcogenides MX_2 (M = Mo, W, Zr and Ti. and X = S and Se) have the similar structure of stacking hexagonal shape layers, as shown in Fig. 2.11, reported in Science in 1987[127]. In a graphite structure, the in-plane atomic layers form the basic unit as a hexagonal honeycomb cell, which has the strong covalent bonds between the in-plane atoms. Whereas a related weak Van der Waals force (dashed line between each plane) forms the bond between each adjacent layer. Similar to the graphite structure, MX_2 compounds also exhibit the hexagonal honeycomb cell structures, however each layer consists of a 'sandwich-like' unit cells with 3 stacked atomic planes. For example, the 2H-WS_2 is a typical form with this 'sandwich-like' structure. Each unit cell is composed of one middle plane of W atoms and other two outside planes of S atoms, forming S-W-S. As a result of this stacking sequence, the metal dichalcogenide has two main different crystal structures: 2H hexagonal and 3R rhombohedral polymorphs[28, 128]. Compared with the 3R polymorph, the 2H hexagonal structure has the continue sequence of BaBBaB in the crystal, which is one of the most stable phases for these sorts of compounds.

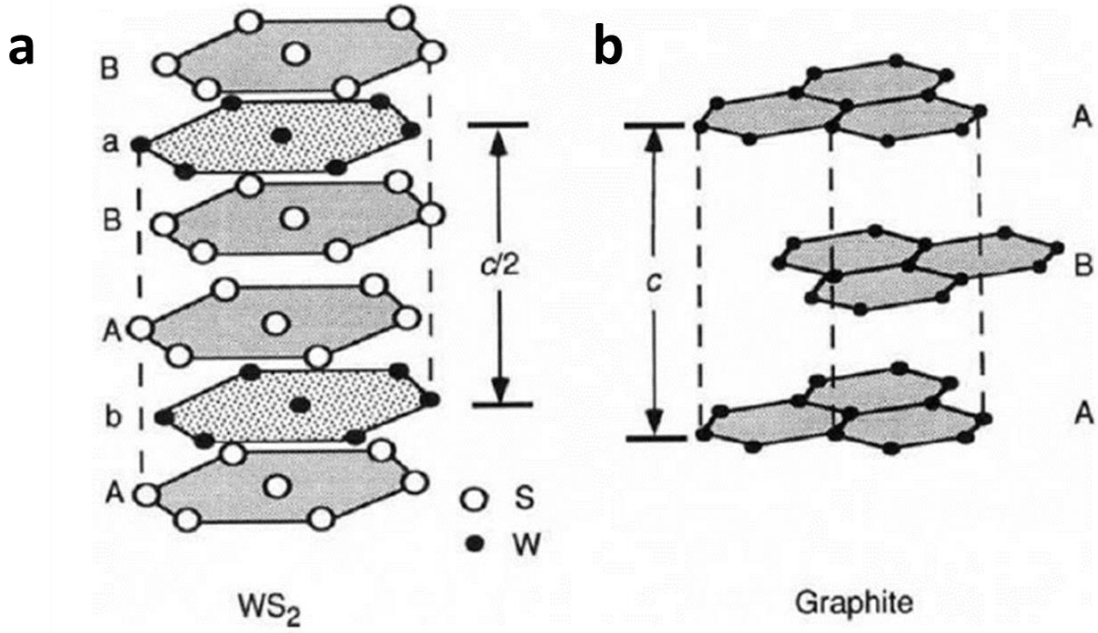

Fig. 2.11 Different atomic structures of metal dichalcogenides and graphite structure. a. 2H hexagonal WS_2 structure has the continue sequence of BaBBaB in the crystal; b. classical Graphite ABA structure[127]

After Geim and Novoselov *at el.* successfully discovered graphene, similarly stable and graphene-like MX_2 have also been investigated at a few layers level[11]. Ramakrishna Matte *et al.* reported the only 2 or 3 layers of MoS_2 and WS_2 with graphene-like structure by using the intercalation and exfoliation methods[129]. As shown in Fig. 2.12, the thin layer of WS_2 sheet was clearly displayed with the bright colour in the AFM image, followed by height measurement with only around 1 nm in thickness, which demonstrates the 2 layers of the WS_2 sheet. Akin to graphite, bulk forms of MX_2 are also known for their good lubricating properties. Furthermore, graphene-like nanoflakes of MX_2 have also shown excellent catalytic performance in oxygen evolution reaction (OER) and/or the hydrogen evolution reaction (HER). Even though the other properties of graphene-like MX_2 nanoflakes have yet to be fully confirmed, these materials have a good potential to be used as nanofillers to reinforce various matrices to fabricate advanced nanocomposites.

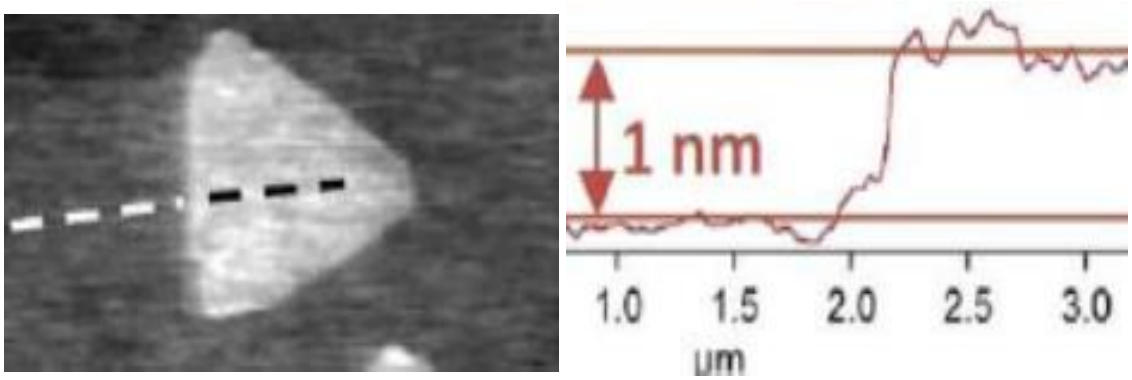

Fig. 2.12 AFM image of graphene-like WS_2 sheet. (The thin layer of WS_2 sheet was clearly displayed with the bright colour, followed by height measurement showed 1 nm in thickness, which illustrates the WS_2 sheet only has 2 layers)[129]

2.4.2 Structure of inorganic fullerene (IF) WS_2

Similar to the structure of carbon allotrope, dichalcogenides exist equivalent structures to fullerenes and CNTs. Because these structures contain no carbon, they are called inorganic fullerene (IFs). As shown in Fig. 2.13a, the typical IF-MS_2 named IF-WS_2 could arrange the seamless nano spherical structure[130]. In Fig. 2.13b, a clear HR-TEM IF-WS_2 nano hollow-onion structure with lattice distance of 0.62 nm is shown[131]. Generally, the size of the synthesised IF-MS_2 is always below 200 nm, due to thermodynamic reason. Otherwise, it is easier to form the more stable structure of nanoplate MS_2. Moreover, compared with the multi-walled structure, the synthesis of single-walled IF-MS_2 structures is possible only theoretical. Because the basic structure of MS_2 is the 2H and shown in Fig 2.11 and it is cannot realize single layer IF-MS_2 unless applied some templates[132]. To date, the multi-walled IF-MS_2 are used in both industrial and laboratory experimental applications. The novel structure of IF-MS_2 has shown excellent lubricating properties and been considered as an alternative lubricant for their flake forms of MS_2, due to their extra rolling mechanism to reduce friction. These new IF-MS_2 nanoparticles also have high specific surface areas, therefore they can be potentially used in hydrogen storage technologies.

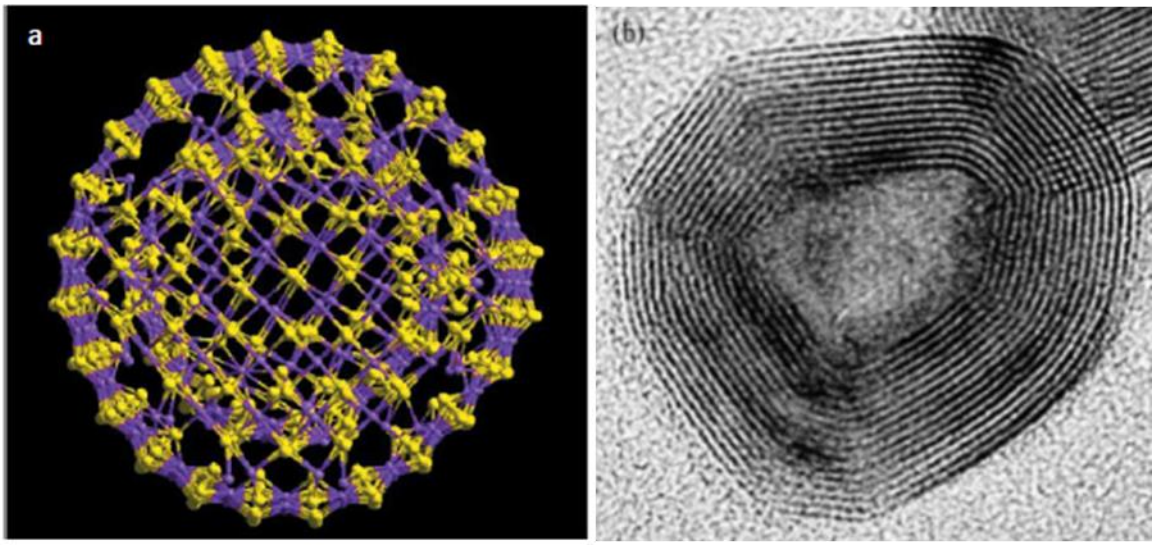

Fig. 2.13 Scheme of IF-WS_2 and HRTEM images of IF-WS_2 nanoparticles[130, 131]

2.5 Preparation of IF-WS_2 nanoparticles

So far, there are diverse approaches for the synthesis of IF-WS_2 nanoparticles, however the effective method that are suitable for scalable manufacturing is quite limited. Four main strategies for IF-WS_2 nanoparticles production will be summarised here[133].

2.5.1 Gas-phase reaction

In the gas-phase reaction, IF-WS_2 (or INT-WS_2) structures can be achieved by reacting H_2S with various vaporised tungsten-containing chemicals, such as WCl_n (n=4, 5, 6) at high temperature. As shown in Fig. 2.14, Margolin *et al.* have shown that the reducing H_2S gas and the protective gas N_2, will carry the precursors of WCl_n into the reactor, where they will react with H_2S to form the final products which can be collected from the other side of the reactor[134]. Recently, the mechanism of forming IF-WS_2 from a diverse range of WCl_n has been studied intensively, and it is found that WCl_4 and WCl_5 are the most suitable precursors to produce IF-WS_2 nanoparticles.

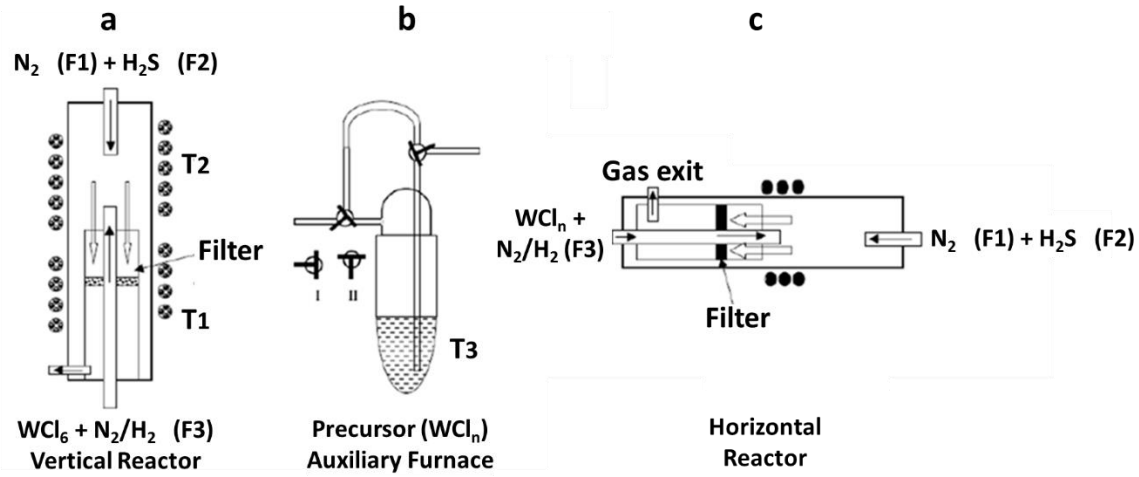

Fig. 2.14 Scheme of gas-phase reaction reactor and the synthesis path of the IF/INTs-WS_2.[134]

2.5.2 Chemical vapour deposition (CVD)

The tungsten source from the WCl_n gas phase can be oxidised to form solid state WO_3, and then to react with either S or H_2S, so that IF-WS_2 (or MoS_2) nanomaterials can be synthesised during these reactions. This process is named as the CVD, which has nowadays been used for numerous nanomaterials synthesis. However, CVD carried out normally in a static furnace reactor, and agglomeration, sintering and incomplete or non-uniform formation are often observed. Tenne's group created a static reaction setup with multi-tube combination system, as shown in Fig. 2.15 for the static reactor. A set bundle of tube reactors (Diameter 7mm) are placed in the one large tube (Diameter 40 mm) and it can produce about 1 g IF-WS_2 per batch[135]. This method attempts to gain the production by simply adding the number of reactors in the per unit time.

To counter these challenges, Feldman *et al.* and Tenne from the same Israel research group created a vertical heating furnace synthesis system with a falling bed reactor, where the temperature profile is along to the vertical axis and it can significantly improve the yield of the IF-WS_2[136, 137]. In this design, the gas (N_2) feeding system for the precursor of WO_3 can be applied by the gravity effect and realized the semi-continuous production, as shown in Fig. 2.16a. Based on the same principle, the fluidised bed reactor was also created and

displayed in Fig. 2.16b. Furthermore, Feldman *et al.* reported a similar work in which can synthesise IF-MoS_2 nanoparticles with size ranging from 20 to 80 nm, at 800 to 950°C. Increasing the reaction temperature above 900 °C would lead to some open-ended INT- MoS_2 structures, rather than IF structures. Because the sulfuration reaction occurred on surface of the WO_3 particles, where the higher reaction temperature is, the higher surface activated energy will be. The contacted WO_3 particles are easier to form the tube structure.

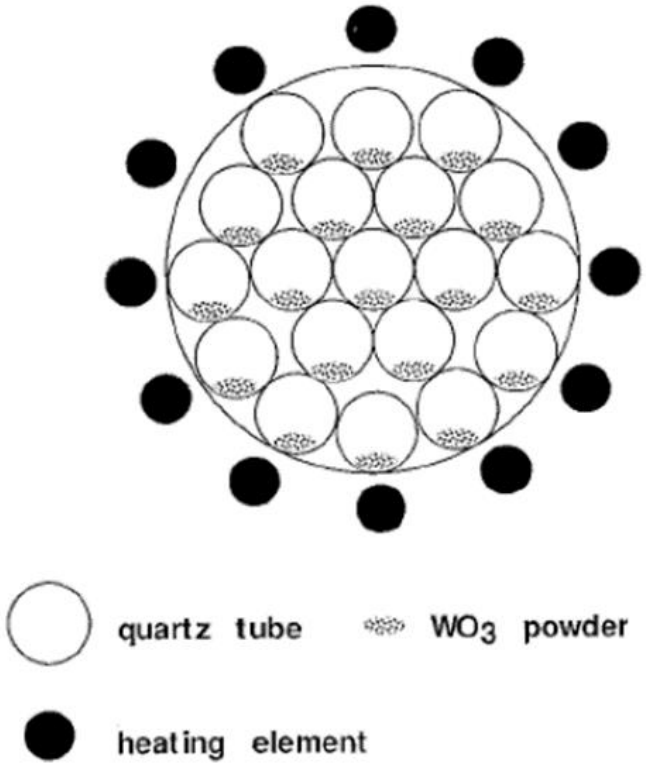

Fig. 2.15. The cross-section of the multiple bundle of static tubes setup for IF-WS_2 synthesis[135].

Xu *et al.* further developed a rotary chemical vapour deposition (RCVD) method (Fig. 2.17)[138]. The key feature of the RCVD, as implied by its name, is the rotary motion introduced into the reactor so that constant physical movement will help to disperse the raw precursors thereby achieving complete and uniform nanostructures without varying about the sintering effect. Further, the furnace can be added with a specially designed feeding and collecting system while rotating, to realise continuous manufacture. The pressure for all experiments is

just remained the positive pressure, which is a little bit higher than the environment outside. In the RCVD process, the precursor particles of WO_3 were blown into the reactor continuously by N_2/Ar carrying gases. Then the H_2S and N_2/Ar mixture gas will be fed in to participate in the reaction between H_2S and WO_3. The typical reaction temperature ranges from 750 to 900 °C, with a controllable heating period of 30 to 120 min. At the end of the reaction, IF-WS_2 nanoparticles were deposited at the end of the collection part of the long reaction tube. Depending on the raw precursor, the size of the IF-WS_2 nanoparticles was tuneable, typically around 50 nm.

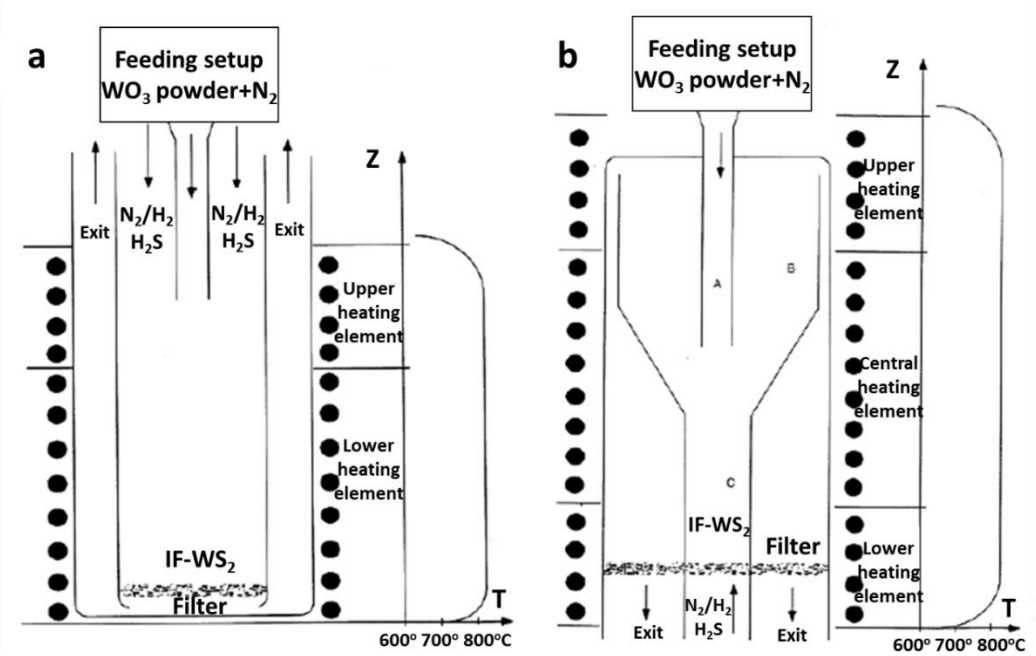

Fig.2.16. Schematic images of: a. falling bed reactor; and b. fluidised bed reactor[136, 137].

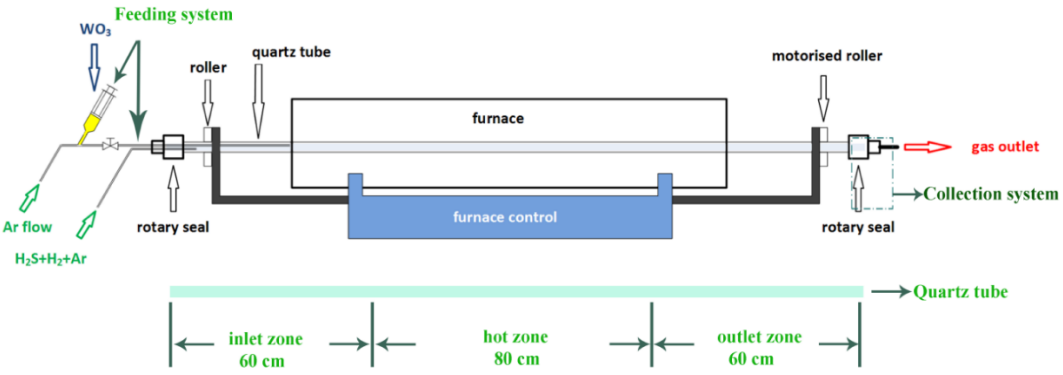

Fig. 2.17. A schematic of the RCVD system[138].

2.5.3 Metal organic chemical vapour deposition (MOCVD)

The metal organic chemical vapour deposition (MOCVD) is a modified CVD method, defined by the use of the typical metal hexacarbonyls precursor type. These metal organic precursors react with chalcogenides in a protective gas environment to form new materials[139]. Compared with metal-halides (MCl), metal hexacarbonyls have relative lower melting and boiling points[140]. Consequently, they can be easily evaporated under heating. Chung *et al.* demonstrated the use of MOCVD to produce WS_2 thin films. In a typical process, the $W(CO)_6$ powders were evaporated first in a bubbler[139]. Then, the resulting vapour was delivered into a quartz reactor by Ar or N_2 mixed with H_2S gas flow. A Si substrate was placed in the middle part of the quartz tube reactor, which was heated to around 600 °C by a halogen lamp. After the $W(CO)_6$ was completely reacted with H_2S, a thin layer of well-crystallised WS_2 on the Si substrate resulted in. The orientation of the crystals in the product exhibited two modes: parallel to the basal planes of the substrate and nonparallel. The thicknesses of the WS_2 thin films was controllable by tuning the reaction time (1.5 to 5h), ranging from 65 to 350 nm.

Using similar technique, other research groups reported thin films of WSe_2, MoS_2, $MoSe_2$, even without the use of a substrate[141-143]. A modified process by using mixing $Mo(CO)_6$ and S powders to react in a sealed stainless-steel container at 750°C for 1 to 3 h has also been documented. The average thickness of the final product ranges from 20 to 100 nm. However, this technique has less potentials in enlarged IF-MX_2 synthesis, because of the cost of precursor.

2.5.4 Other Methods

Hydrothermal/solvothermal reaction

The hydrothermal or solvothermal technique is a common route for the production of uniform nanoparticles, which utilises the condition of high-temperature and high pressure within certain solvents. This approach can be classified into two types, dependent on the choice of the solvents: the water-

based solvent-hydrothermal synthesis and the non-water-based solvent-solvothermal synthesis[144, 145]. In this versatile technique, different types of reactant solution can react together in a sealed vessel under high temperature therefore pressure conditions, which can arrive a few times higher than the normal boiling point of the solvents under ambient pressure. Due to the entire sealed system can prevent the evaporation of solvent out of the vessel, high pressure will be created inside the container. By combined the advantages of both high temperature and high pressure together, this technique has been used to generate many homogenous novel nanoparticles.

The MX_2 can be produced by decomposing from the precursors of analogue metal chalcogenide. To synthesise MX_2 by using the hydrothermal method, $(NH_4)_2MS_4$ have been chosen due to their great water solubility and contained S source. Taking MoS_2 as an example, we briefly show how this was carried out by using $(NH_4)_2MoS_4$ as a precursor. Firstly, $(NH_4)_2MoS_4$ and $Na_2S_2O_4$ were mixed completely with thioacetamide under an ammonia environment. The mixture was then transferred to and sealed in an autoclave with a Teflon liner vessel, followed by heating to 180 °C for 1 h. Finally, the resulting product showed a novel flower-like structure, with sizes ranging from 200 to 1000 nm. These flower-like MoS_2 consisted of tens of hundreds of the self-assembled petals growing in all directions. Furthermore, each petal displayed the nanoflake structure with size around 100-200 nm and thickness of 5-10 nm approximately. Similarly, the WS_2 nanoflowers could be synthesised by using $(NH_4)_2WS_4$, $NaBH_4$, pyridine and trioctylamine. Moreover, nanoflakes could be prepared from nanoflowers by annealing them at 850 °C, and discrete WS_2 would be resulted.

Although the hydrothermal method had been applied to synthesise a wide range of metal chalcogenide materials, only a few investigations had been focused on the IF-MX_2 production. Because the structures of folding and recrystallization involved in the IF-MX_2, higher demand for energy would be required as compared with flake formation.

2.6 The mechanism of IF-WS_2 growth

After a few decades of exploration, the understanding of the mechanism for the formation of IF- MX_2 nanoparticles from their corresponding oxides reacting with H_2S is quite clear. Fig. 2.18 explains the conversion of MoO_2/WO_3 to their corresponding IF nanoparticles, with three main steps[135].

Taken the IF-WS_2 as sample and shown in Fig. 2.18b. Firstly, the surface of a metal oxide will be reduced to its corresponding state of sub-oxides rapidly, and this process just lasts for a few seconds, or even less. In the case of WO_3, the surface atoms of WO_3 react with H_2S at high temperature to form a closed WS_2 thin layer immediately sheathing the remaining oxide core. This newly formed WS_2 layer is chemically stable, therefore it tends to prevent the surface of neighbouring nanoparticles from merging together and growing into larger particles.

Secondly, because of the heating process, the inner WO_3 oxide cores will further reduce to $W_{18}O_{49}$, and this stage lasts for a few min. After this reduction process, the WS_2-encapsulated $W_{18}O_{49}$ core is formed, the very thin and tiny WS_2 crumbles to create reactive dangling bonds which promote the WS_2 layers thickening simultaneously. As a result, the final product will be IF-WS_2, instead of 2H-WS_2 structures.

Thirdly, the sulphidation process of the oxide core is by gradual sulphur inwards diffusion, to form the inner layers of the IF-WS_2 spherical/polygonal structure. Depends on different sizes of the raw nanoparticles and the reaction temperatures, the required reaction time varies from 30 min to 3 h. For WO_3 nanoparticles with typical sizes < 100 nm, the reaction time is 1 to 2 h. Because of the stable WS_2 shell formed outside the initial WO_3 during the first stage, the final size of IF-WS_2 is thus pre-determined by that of the precursor. Meanwhile, the density difference between the WO_3 and the WS_2 will also leads to a volume shrinkage internally, hence resulting in hollow IF-WS_2 nanoparticles, with 5-10% of the total volume of the particle being hollow.

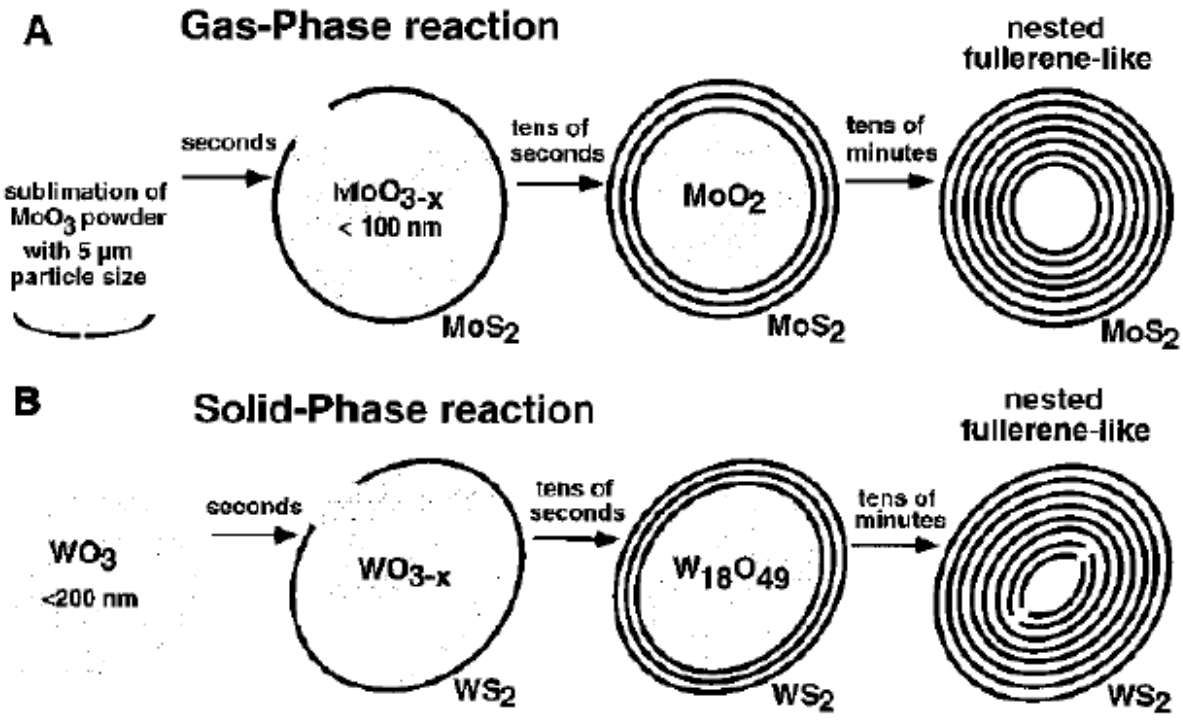

Fig. 2.18 Illustrations of the growth mechanism of IF structure from their corresponding precursor oxides. A. MoS_2 and B. WS_2[135].

2.7 Properties and applications for IF-WS_2

2.7.1 Mechanical properties

The bending and tensile properties of the INT/IF-WS_2 have been reported, and an individual INT-WS_2 has shown a very high bending modulus of ~217 GPa which was measured by using an electric-field-induced resonance method. A high-resolution SEM electron microscope image (HR-SEM) in Fig. 2.19 shows that an INT-WS_2 was bent when compressed against a Si wafer[146].

In contrast, the tensile testing can be applied to the WS_2 NPs (Fig.2.20a). The tensile stress-strain plots clearly show the individual INT-WS_2 elastic deformation, which allows to calculate its mechanical properties[147].

As the slope of the stress–strain curve shown in Fig. 2.20b, the tensile strength is about 20 GPa and strain at 8.5%, and calculated the ultimate elastic Young's modulus is approximately 235 GPa[147].

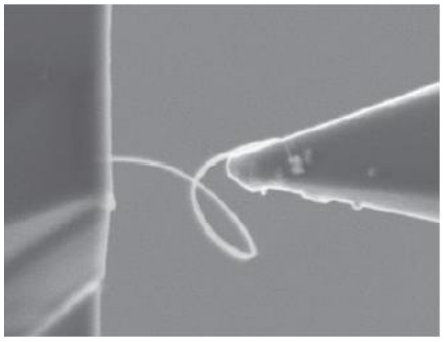

Fig. 2.19 HR-SEM image of a bent INT-WS_2 compressed against a Si wafer[146]

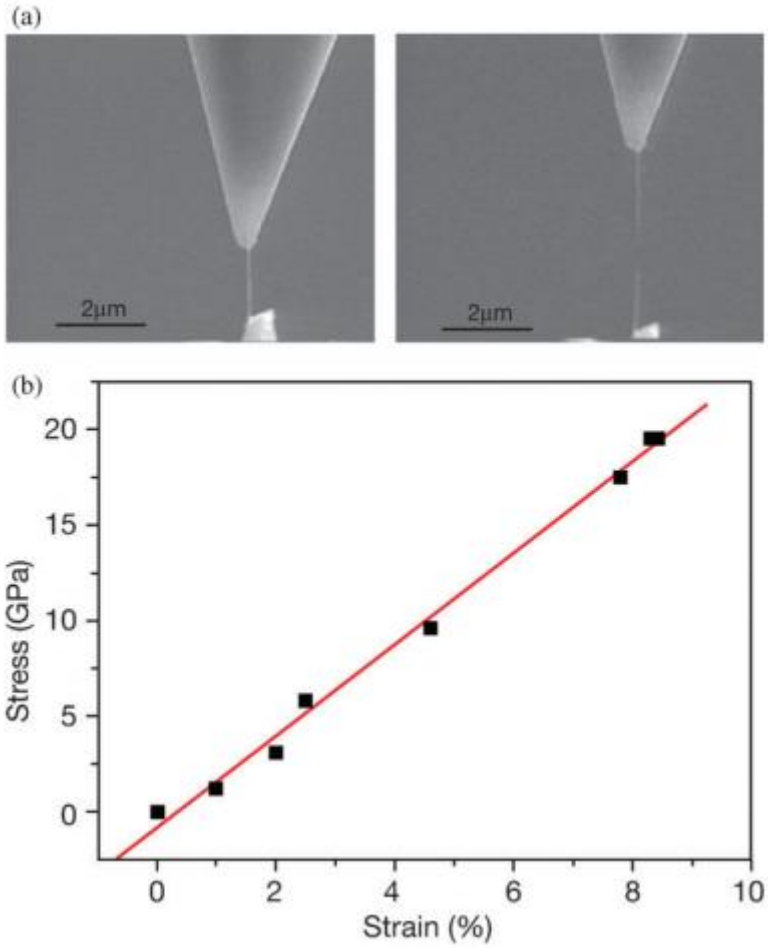

Fig. 2.20 a) HR-SEM image of a tensile test of an INT-WS_2, and b) the corresponding stress–strain curve[147]

2.7.2 Tribological property

Due to the hollow cage feature and the graphite-like layered structure of IF-MX_2, they have shown stunning lubricating performance, compared with their 2H flakes or bulk form. These novel materials could have 3 different modes of

friction, as shown in Fig. 2.21, rolling, sliding and exfoliation, respectively[148]. Therefore their properites are considered as an ideal lubricating material. Many studies have recently reported the great lubricating performance of INT/IF-MX_2, and in 2008 the use of IF-WS_2 as a core additive in commercial lubricating oil was realized[134]. These nanoscale additives could bring in distinct advantages in lubricating oil. First, the small size of the IF-WS_2 particles makes them easier to be dispersed in oil to form a stable and homogenous suspension, compared with the larger sized flakes. Moreover, the nano-lubricant could easily gain accesses into the gap between the wear couples than larger particles[131].

Agglomeration of the nanoparticles in oil remains a big issue, since it affects the dispersal ability and the product shelf-life, particular at higher concentration. Several attempts based on surface modification have recently been reported to counter this issue. For example, the alkyl-silane or alkyl-amine chains were attached to the surface of IF-WS_2, resulting in improved solubility in certain solution.

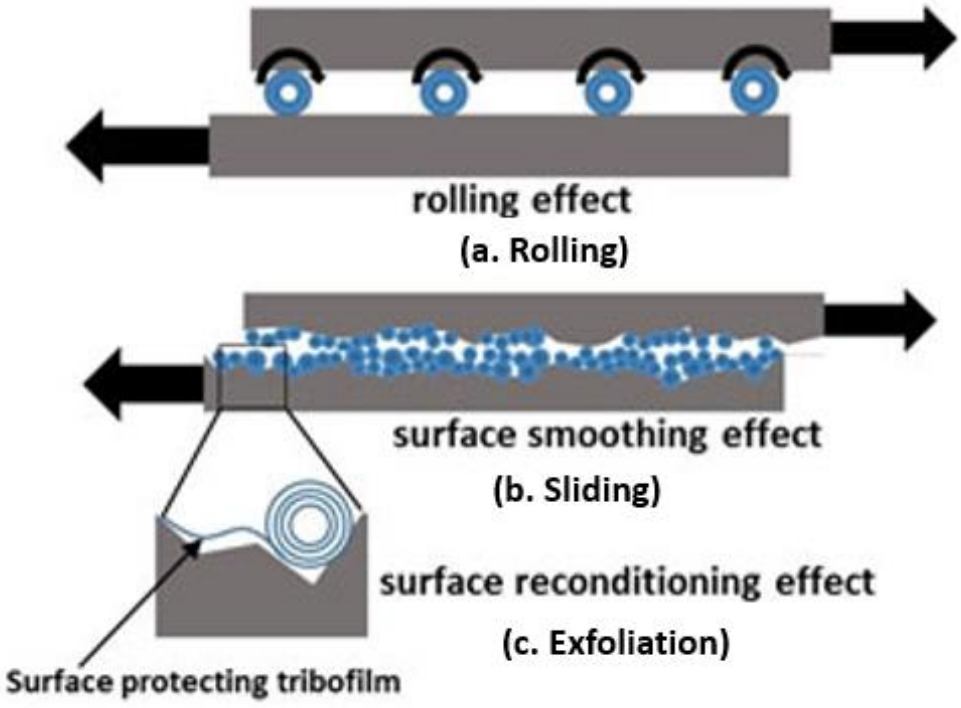

Fig. 2.21 Three main friction mechanisms for IF-WS_2 nanoparticles: (a) rolling, (b) sliding, and (c) exfoliation[148].

2.7.3 Shock absorbing properties

When a projectile is launched and hits a sample at high speed, shockwaves will be generated and propagate within the target sample. Meanwhile, the high shockwave pressures transmitting though the sample will also cause concurrent high temperatures. Using shock recovery experiments, Zhu and his co-workers have first reported the superb shock absorbing performance of IF-MX_2 nanoparticles, especially the IF-WS_2[149]. The particles have survived temperatures closing to 1000 °C under a shockwave pressure of more than 25 GPa. They have also demonstrated that the IF-WS_2 nanoparticles are the toughest caged molecules in this world. Also, the spherical caged structures can persist against a static pressure up to 30 GPa[150].

Fig.2.22 briefly demonstrates the shock recovery experiment[151]. Firstly, the sample was fully filled in the middle of the capsule with steel spacer. Secondly, a plastic projectile with steel impactor head was applied to hit the sample. According to the principle of restriction of thermal diffusive speed, this decay time of thermal transmission through the sample will take much longer than the time of shockwave spread in the sample. Therefore, this is an in-situ technique to identify the material shock recovery property, without the impacting heat influence.

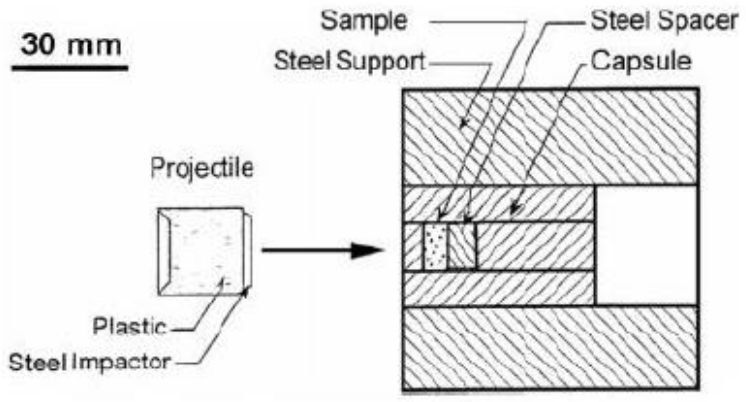

Fig. 2.22 A single-stage gun assembly of the shock recovery experiment for IF-WS_2 nanoparticles against the high shockwave pressure[149].

Based on the results of a series of high pressure shock recovery experiments, Zhu *et al.* proposed two possible destructive mechanisms for the IF-MX_2

nanoparticles[151]. The first one is the direct stress-induced breakage failure, and the other is the diffusion-controlled oxidation. These two modes either appear separately or combined together. In addition, several different factors will affect the likelihood damage of the IF-MX_2 nanoparticles under strong shockwave impacting. First one is the inner oxide residue core (Fig. 2.23a), the uncomplete reaction will form a uneven structure which reduce the shock recovery ability. And for the exterior edging geometry (Fig. 2.23b), it will concentrate the force into the angle of the surface and damage the particle. Moreover, the overall dimension (Fig. 2.23c) will lead the shape of the particle not to form a perfect sphere structure and reduce the property. They have further concluded that the best anti-shock IF-WS_2 structures are the perfectly spherical particles with the small size and completely hollow core. These findings have shown huge potentials for ballistic armoury applications. These materials not only offer great shock absorbing performance to protect against high temperatures and high dynamic pressures, but also could stop bullet penetration being tough materials themselves. Indeed, they have recently further verified the shock-absorbing performance in an Al matrix composite, which could turn the IF-WS_2 nano-armour science fiction into an engineering reality.

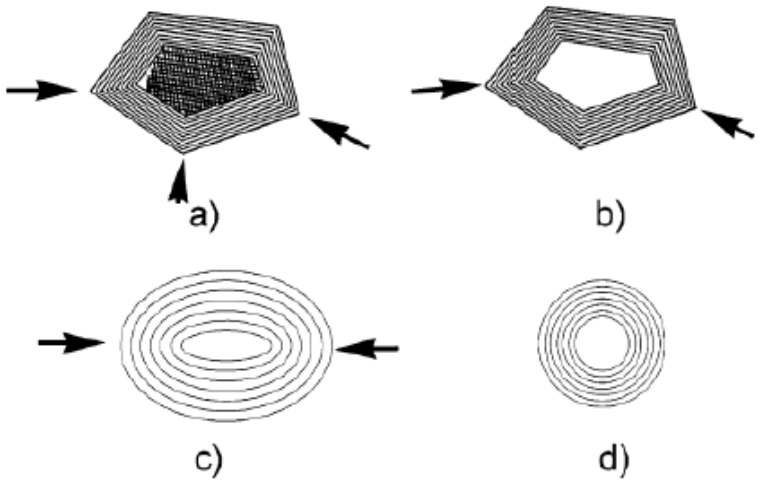

Fig. 2.23 Illustration of the likelihood damage of IFs under shockwave pressure. a) the uncomplete reacted oxide residue core will form an uneven structure; b) for the exterior edging geometry, the angle of the surface may easily damage; c) the overall dimension particle has always not the perfect sphere structure[151]

2.7.4 Thermal properties of IF nanoparticles

There are numerous of reports about the thermal stability of IF nanoparticles and nanoflakes of WS_2, MoS_2 and NbS_2 *etc.*, which are surveyed by TG-DTA under oxidising and inert atmospheres respectively[152, 153]. The results have showed that MX_2 nanoflakes have higher thermal stability than their corresponding IF forms, whereas the decomposition temperatures exhibit a similar trend for all MX_2 nanoparticles. For example, the IF-WS_2 decomposition temperature in open air is around 350~400 °C, and approximately 1350 °C under N_2. The size of the particles shows almost no influence on the decomposition temperature. After decomposing in inert gas atmosphere, the original IF-WS_2 nanoparticles initially became a mixture of 2H-WS_2, W and $W_{18}O_{49}$, and finally were all converted to nanoflakes. This result indicates that the IF structures do not have the same stability as the flakes at high temperatures.

2.8 PEEK (Poly ether ether ketone) and its relevant composites

2.8.1 PEEK (Poly ether ether ketone)

In the past decade, the fast-growing needs for advanced materials promote the development of high performance polymers, towards a diverse range of applications for aerospace, automotive, and microelectronic industries. High glass transition temperatures, toughness, anti-oxidative and thermal stability, and low dielectric constant are the main requirements for high performance polymers. As a semi-crystalline thermoplastic polymer, poly(ether ether ketone) (PEEK) is one of the excellent candidates to meet those requirements, belonging to the polyaryletherketone (PAEK) family[154-157]. It was first synthesized by the Imperial Chemical Industries (ICI) in the beginning of 1980s. The outstanding mechanical properties show almost 100 MPa for tensile strength and over 3GPa for Young's modulus. Further stable chemical properties, such as relative high melting points (~343°C), lower thermal conductivity rate and anticorrosion of strong acids in high temperature, make this material really promising.

Generally, polymer of PEEK is synthesized by the step-growth polymerization process of alkylated bisphenolic salts. The typical chemical synthesis process of PEEK is shown in Fig. 2.24 with the reaction between the 4,4'-difluorobenzophenone and hydroquinone disodium. This reaction can react around 300 °C in some polar aprotic solvents, like NaF[157].

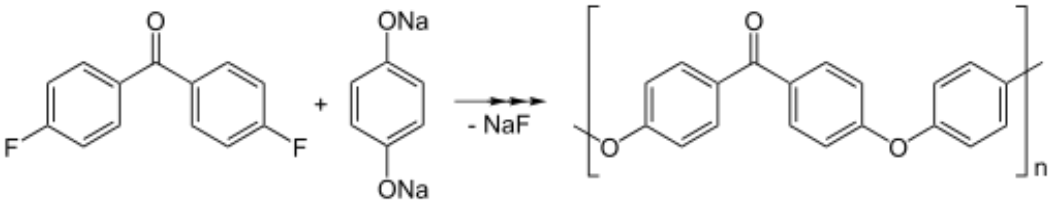

Fig. 2.24. The typical chemical synthesis process and structure of PEEK[157]

2.8.2 CNT, Graphene and Metal oxide reinforced PEEK composites

Novel PEEK based nanocomposites with different contents have been investigated in the last few decades. Díez-Pascual *et al*. illustrated that the SWCNT-reinforced PEEK composites have considerably high storage modulus and glass transition temperature with very low CNT content[158]. Tewatia *et al.* prepared the graphene reinforce PEEK composites and investigated the specimens from powder to laser sintered. Apart from the tensile strength improvement, the porosity and maximum pore size relationship, which is increasing with amounts of graphene increase, was first demonstrated[*159*].

In addition, Díez-Pascual demonstrated that ZnO nanoparticles prepared by the cryogenic ball-milling and compressed moulding could achieve good dispersion in and interfacial adhesion with the polymer matrix, which significantly improved the tensile strength and Young's modulus to a maximum of 5.2 GPa[160]. Furthermore, he also reported that TiO_2 nanoparticles reinforced PEEK was an outstanding implant material, with great biomechanical properties[161].

2.8.3 IF-WS_2 reinforced PEEK composites

To make PEEK even better and meet the requirements for more demanding applications, the combination of PEEK with various fillers to make advanced composites is a logical option. Given the merits of IF-WS_2 nanoparticles discussed earlier, the combination of PEEK and IF-WS_2 is thus very attractive. Naffakh *et al.* have reported the processing of novel PEEK/IF-WS_2

nanocomposites, and obtained promising results only at IF-WS_2 concentration of up to 2%[162]. In particular, Hou *et al*. in Nottingham have incorporated IF-WS_2 into PEEK coatings using an aerosol-assisted deposition, and their results showed a significant improvement during wear test, with over 60% reduction in the coefficient of friction at only 2.5% of IF-WS_2 addition[163]. And they also attempted to prepare the 20 wt% loose coating outside the metal surface to reduce the COF significantly. However, for the bulk sample, at higher concentrations, nanoparticles agglomeration become severe[164]. This is a big challenge needs to be tackled. Further systematic characterisations are required in order to understand the interface structures between the PEEK matrix and the IF-WS_2, and to achieve higher filler contents in the nanocomposites.

2.9 Summary

In this chapter, the recent studies of the carbon coating metal oxide and its corresponding polymer composites have been summarised, including the metal oxide coated CNT composites. Review on some the mechanical, chemical structure and properties of INT and IF-MX_2, especially the IF-WS_2, has been undertaken. The crystal structures, synthesis and properties of the IF-WS_2 were introduced. They are considered as idea solid-state lubricants and have further applications as lubricating additives and shock absorbing protective amour. The understanding of tribological mechanism is discussed and further study and improvement in these areas will be tremendously interesting. Therefore, my project is to link those novel nanoparticles into the new high performance polymer matrix, especially by using the PEEK. Their properties and related nanocomposites showed promising potentials either in mechanical applications or for thermal conductivity improvement. Last but not the least, the combination of IF-WS_2 and PEEK to make composite could lead to super tribological property, exhibiting a great future.

Chapter 3. Experimental methodology

3.1 Introduction

In this chapter, the materials and generic methods applied to the synthesis of several types of carbon-coated (C-coated) nanoparticles and techniques used to fabricate their derivative nanocomposites will be presented. In addition, the general techniques utilised to characterise the morphology, structure, and related properties of these nanoparticles and their polymeric matrix nanocomposites will also be described.

3.2 C-coated nanoparticles preparation

3.2.1 Materials

All the metal oxide particles, including ZnO (100~200 nm, measured by BET), TiO_2 (5~20 nm), CeO_2 (~100 nm), Cr_2O_3 (~200 nm), ZrO2 (30~60 nm) and Y_2O_3 (~50 nm), and styrene (analytical reagent 99.99%) were purchased from Sigma-Aldrich. Other solutions such as ethanol and acetone (analytical reagent 99.99%) were bought from Fisher-Scientific. Argon were purchased from BOC, UK.

3.2.2 Rotary Chemical Vapour Deposition (RCVD) furnace

The chemical vapour deposition (CVD) method had been applied to form the nano graphitic coating. To reduce the agglomeration, realize continuous manufacturing and achieve large scale synthesis of those NPs, we have developed a Rotary Chemical Vapour Deposition (RCVD) system by modifying the Xu's method[31, 138]. We have added the liquid injection control part and improved the balance system to make it more practical. Further detailed associated with the construction, testing and refinements in this work are illustrated in Fig. 3.1a and b. Especially in Fig. 3.1c, the tiny pipe on the left side is the liquid injection tube which is connected to an automatic syringe pump. On the right side, the modified motorized roller with double rubber belt is applied to the original Al roller, which could improve the stability of the dynamic system. Additional information about the coating process is displayed in Fig. 3.1b. The vapour nano carbon fragments formed during the CVD stage will be deposited smoothly on the surface of the NPs with the mechanical rotary movement.

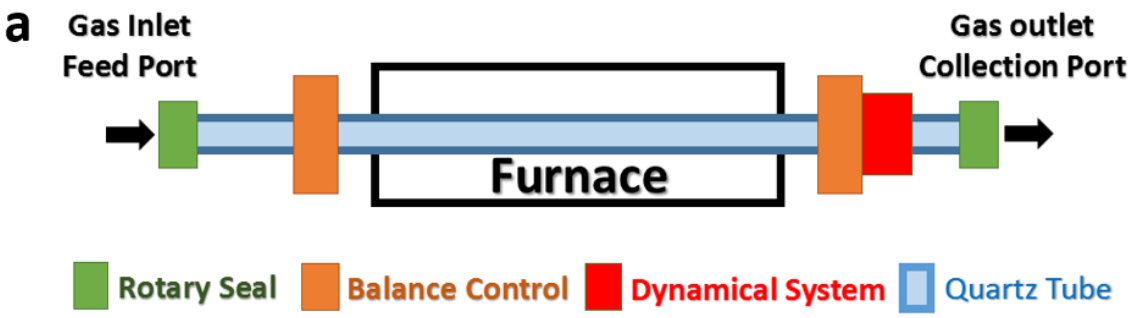

a. Sketch of the modified RCVD system

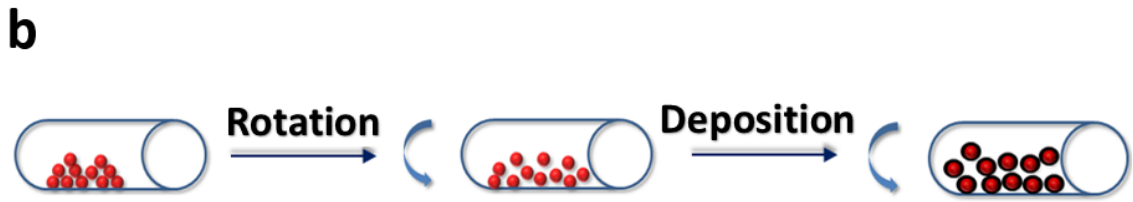

b. Illustration of the C-coating processes during the RCVD synthesis

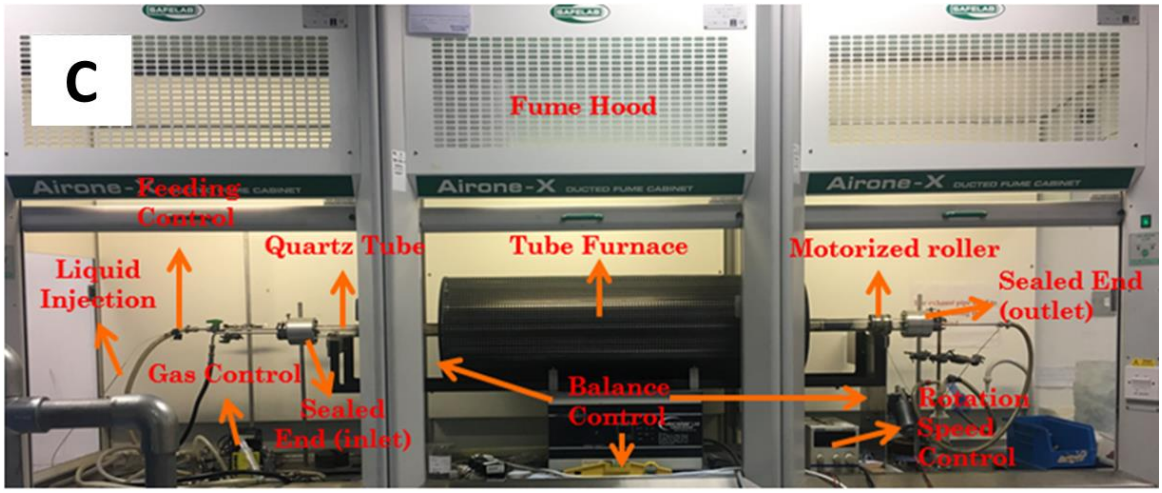

c. Images of the RCVD system

Fig. 3.1 The original/modified Rotary Chemical Vapour Deposition (RCVD) system

3.2.3 Preparation of C-coated NPs

The C-coated NPs were synthesised by dispersing 10~50 g of certain NPs into 100 ml ethanol under vigorous magnetic stirring for 1 h without any surfactant, followed by ultrasonic probe dispersion for 30 min. The resulting mixture suspension was first dried at 80 °C in a long tube furnace (VecStar Ltd.) to obtain dry powder, which was then grinded into fine powders by using an agate mortar, and finally transferred into the inlet part of the long quartz tube (2-meter-long with an inner diameter of 35 mm). The carbon precursor was prepared by ultrasonic mixing of acetone and styrene solutions with a volume ratio of 4:1. The reaction zone of the system was sealed by the designed rotary seals at both ends. The rotary system was heated under Ar flow of 100 ml/min, and 2 ml/h of the carbon precursor was introduced into the reaction zone for 15 to 60 min, at temperatures varying from 550 to 1000 ^{o}C (optimised temperature is about 800 ^{o}C), and then naturally cooled down to room temperature under Ar protection. The final chemicals were named as MO_X@C-T, where the M = Ce, Cr, Zr, Y, Ti and Zn *etc.*, X = 1, 1.5 and 2, and T represents the temperature applied.

3.3 Fabrication procedure of Nylon 12 nanocomposites

3.3.1 Materials

In this thesis, the nylon 12 was purchased from EOS Ltd., German (Polyamide (PA) 2200, melting point (T_m) 178~180 ^{o}C, the particles size <0.1 mm, and the density of 1.01 g/cm^3).

3.3.2 MO_X@C-Nylon 12 nanocomposites

In order to demonstrate the processing potential of the C-coated metal oxides for reinforcing nylon 12 in nanocomposites, ZnO@C NPs were chosen as an example. Choosing nylon 12 as the matrix is due to its flexible processability and for the easy comparison with many existing literatures. A simple mixture re-melting technique was used to create a thin composite film, which would allow us to carry out sufficient investigations to reach a convincing conclusion.

In detail, the fabrication involved a few steps, as follows:

a) Wet-powder premixing

A 1:1 mixture of ethanol and distilled water was used as the solvent to disperse the powders. ZnO@C NPs and nylon 12 powder were separately dispersed in 100 ml of the solvent, followed by 1 h vigorous magnetic stirring. Then the two resulting suspensions were mixed together and subjected to powerful ultrasonic probe treatments for 15 min.

b) Powder drying

The well-mixed suspension was heated at 100 ^{o}C under vigorous magnetic stirring treatment for 1 h on a hot plate, in order to remove most of the solvent. Further drying at 120~140 ^{o}C in an oven for 24~48 h resulted in completely fried and well-mixed powders.

c) Fabrication

The mixed powders were transferred onto a glass slide, sitting on a hot plate, with a top surface temperature of 190~210 ^{o}C. After a few minutes, the powders were melted completely to form a thin film, and the glass slide was then moved away and cooled naturally. Upon cooling down, the thin film was easily peeled off from the glass slide, and the ZnO@C-Nylon 12 nanocomposite was resulted.

3.4 PEEK matrix nanocomposites

3.4.1 Materials

Poly ether ether ketone (PEEK) was ordered from VICTREX PEEK Polymer Ltd., UK, model PEEK-450PF (10 um), with a glass transition temperature (T_g) of 147 ^{o}C, melting point (T_m) of 343 ^{o}C, and density of 1.32 g/cm^3. The WO_3 NPs (30~80 nm) was purchased from Changsha Jinkangxin Chemical Ltd., and the Ar and H_2S gases were purchased from BOC, UK.

3.4.2 Preparation of IF-WS_2 NPs and its C-coated NPs (IF-WS_2@C)

a) Synthesis of IF-WS_2 NPs

First of all, the IF-WS_2 NPs were produced by the solid-gas reaction in the RCVDs, where the WO_3 NPs were the precursor which reacted with H_2S under Ar atmosphere. Upon the end of sulfurization process, the H_2S gas was switched off and the furnace temperature was kept at 750~800 °C with the

rotary speed between 150~220 rpm. We also designed a spare collection part of the long quartz tube for the continuous synthesis. Further treatment was washing the resulting NPs with CS_2 solution to remove the surplus S on the surface of the IF-WS_2 NPs.

b) Synthesis of IF-WS_2@C NPs

For the C-coating process, it was similar to the metal oxide coating process. The liquid carbon source (ratio of styrene and acetone is 1:4) was injected at a rate of 1.2-2.4 ml/h for 0.5~1 h, and the vaporised carbon source was carried by pure Ar into the hot zone at a flow rate of 100 ml/min. The obtained uniform nano-sized graphitic C-coated IF-WS_2 NPs were named as IF-WS_2@C-T NPs, where the T is the reaction time in minute.

3.4.3 Fabrication procedure of IF-WS_2/PEEK nanocomposites

Taking the 4 wt% IF-WS_2 NPs to reinforce PEEK matrix as an example, we demonstrate the synthesis procedure as below.

a) Wet-powder mixing

This step is similar to the fabrication of the MO_X@C-Nylon 12 nanocomposites. In this case, 28.8 g of PEEK-450PF powder and 1.2 g IF-WS_2 NPs were dispersed separately in a 75 ml 1:1 alcohol-water solution. After vigorous magnetic stirring for 30 min, the polymer suspension was then mixed with the IF-WS_2 suspension, which was then subjected to ultrasonic probe treatment for another 30 min.

b) Drying

The well-mixed suspension was heated at 100 ^oC under continuous magnetic stirring for 0.5~1 h, to partly remove the solvent, and a complete removal of the solvent was achieved at 200~240 ^oC for 24~48 h in an oven.

c) Fabrication

The powder mixture was transferred onto a glass slide of 380 to 400 ^oC, sitting on a hot plate. As soon as all the powders were completely re-melted to form a uniform thin film, the slide was removed from the hot plate to cool down naturally, and the composite was then obtained.

3.4.4 Fabrication procedure of IF-WS_2@C-PEEK nanocomposites

For the C-coated IF-WS_2 NPs to reinforce PEEK, a similar procedure was used as above, except that the mixed powder was dried in the oven at 160~180 °C, overnight.

3.4.5 Hot-press fabrication procedure

For the tribological testing, we also prepared some block samples with the size 2 cm × 2 cm × 1 cm by using the hot-press processing. The typical procedure for one complete hot-press circuit is 60 min, involving pre-heat process first, followed by the 2 min venting and 3 min pressing process in sequence with 15 MPa pressure applied, ending with 15 min water cooling to room temperature. The operations were carried out at 400 ^{o}C.

3.5 Material characterisations

In order to gain insight about the relevant morphology, structure, composition, crystallinity and interface feature, as well as to elucidate the growth mechanism of the resulting C-coated NPs and their nanocomposites, a combination of complementary characterisation techniques has been used in this thesis. X-Ray diffraction (XRD), transmission electron microscopy (TEM), Fourier transform infrared spectroscopy (FTIR) and Raman spectroscopy were used to investigate the structural features. Scanning electron microscopy (SEM), atomic-force microscopy (AFM) and X-ray micro-tomography (Micro-CT) were used to visualise the morphology; and energy dispersive X-ray analysis (EDS) and X-ray photoelectron spectroscopy (XPS) were utilised to assess their elemental and chemical valence status.

The thermophysical characterisation of the materials was carried out using thermogravimetric analysis (TGA) and Differential scanning calorimetry (DSC) (TGA-DSC) techniques, to investigate the surface area, carbon content and thermal stability of the resultant materials. Thermal conductivity analysis (TC) was also used to study the composites.

Selected mechanical properties including tensile, Vickers Hardness and tribological performance were conducted for the nanocomposites. A brief introduction of the principles of some of the instrumentations and facilities involved in this thesis will be described below.

3.5.1 X-Ray Diffraction (XRD)

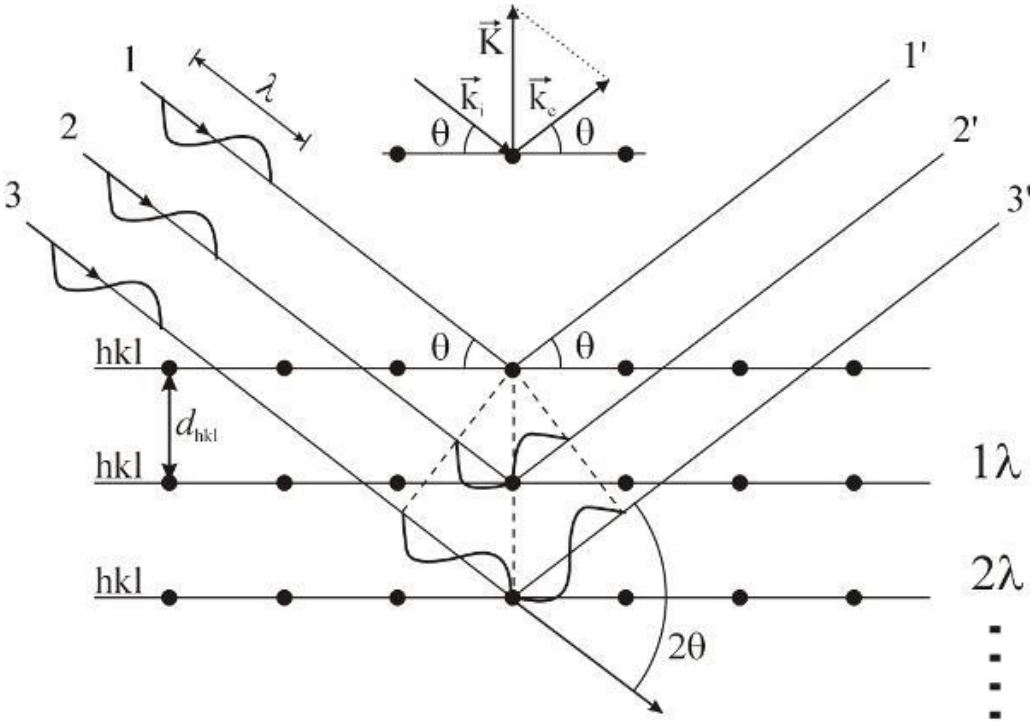

Fig. 3.2 Schematic of the Bragg's law[165].

XRD is one of the most commonly used non-destructive techniques to characterise the crystallographic structure of powder or bulk samples[165, 166]. X-ray diffractions take place when the reflected rays satisfy the condition of the Bragg's law, where the interference comes from the structure planes with a spacing *d* (*d* is also called the inter-lattice spacing). In Fig. 3.2, the incident x-ray can only be reflected by meeting the atoms in the lattice, and the reflection signal will contain the structure information by using the equation below.

$$n\lambda = 2dsin\theta \qquad (1)$$

where *n* is any positive integer; *λ* is the wavelength, and *θ* the incident angle of the X-rays.

The XRD patterns of the studied samples are obtained by plotting the angular positions and their peak diffraction intensities showing relative ratio between different structured phases. Particle size information can also be extracted from the diffraction patterns' profile. By measuring the peak FWHM (Full Width at Half-Maximum) and using the Debye-Scherrer formula, one can estimate the particle sizes, from micrometer scale down to nanometer scale.

In this thesis, all XRD measurements, of either powder or composite thin film samples, were conducted on a Bruker D8 Advanced x-ray diffractometer. The machine was equipped with a Ni-filtered Cu Kα radiation (λ=0.154 nm), and was generally operated at a working current and voltage of 40 mA and 40 kV respectively. The scan ranging from 10 - 70° of 2θ with a step size of 0.05° was enough to obtain sufficient information for my project.

3.5.2 Scanning Electron Microscopy (SEM) and Energy-Dispersive X-ray Spectroscopy (EDS).

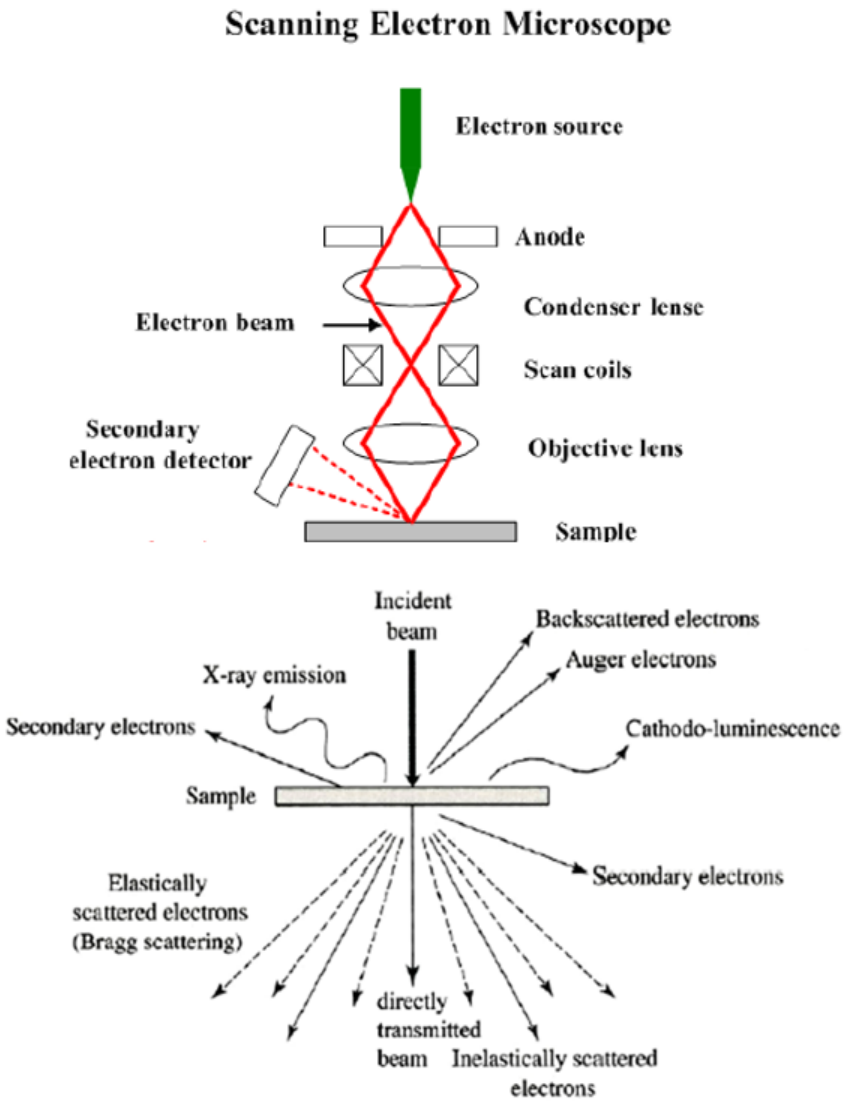

Fig. 3.3 A schematic of the interaction between electron beams and the specimen[167].

SEM is commonly used to study the sample surface morphology with much higher magnification than an optical microscope[167, 168]. Different from the optical microscope which is normally operated in ambient environment, the SEM is operated under vacuum condition. Displayed in Fig. 3.3 is a schematic of the SEM, in which an accelerated electron beam is focused by a series of electric field lenses which are consisting of the anode, condenser lens and objective lens, and it reaches the sample surface to allow interactions. Because the interaction between the electron beam and sample is quite complex, we classify the emitted electrons or rays as secondary electrons (SE), back scattered electrons (BSE), X-ray photons and Auger electrons, respectively. By investigating the signal of SE which is generated by the ionisation process, and its intensity distribution which is narrow and smooth, the surface morphology features of the sample can be detected in detail. BSE however can reveal the elastic scattering electron beam and reflect the different atomic numbers of the elements. Because of its high sensitivity to the atomic number (Z) of the specimen, the atom of a heavy element gives an intensive brighter signal than light elements. Therefore, BSE imaging is a very useful complementary technique for the identification or separation of phase distributions of known elemental compositions when visualisation is uneasy. To more accurately verify the exact elemental feature of a phase, Energy-dispersive X-ray Spectroscopy (EDS) mode can be used to analyse the X-rays produced from the interactions between the accelerated electrons and the target sample surface. EDS however has its limitation of detecting very light elements and of resolution which is determined by its micrometer scale beam sizes, although technological advances have made significant improvements recently. C or Be is normally the detectable limit for most EDS attached to SEM machines. Nevertheless, SEM-EDS has the advantage to link the morphology, grains sizes, phases and quantitative composition features together.

In this thesis, a Toshiba JSM-6390LV machine was used to appraise the powder and composite samples, and SEM images were acquired at 20 kV. An EDS, Oxford instrument Ltd. UK, was also applied to the research.

For our work, there are two kinds of samples need to prepare for the SEM investigation.

Powders:

Samples were prepared by dropping a small amount of powders on one side of the conductive carbon double tape which is pasted on the Ni/Cr sample holder by the other side. Left the holder into the gold/platinum scattering coating machine to coat 1~2 nm conductive layer to reduce the charge of electron beams, if required.

Composites:

The polymer composites are cut into 5 mm × 5 mm × 1 mm small cubic size and placed on the sample holder with double-sided sticky carbon tape. The coating processing is similar to the powder sample preparation, however it needs a relatively thick coating for the block samples, where the thickness is about 5 nm because of the low electric conductivity of polymer materials.

To avoid obtaining the bad contrast imaging of the polymer and MO_X@C or IF-WS_2 NPs composites, MO_X@C-Nylon 12, IF-WS_2/PEEK and IF-WS_2@C-PEEK nanocomposites were detected using the BSE mode to show the distribution of the relatively heavier metal elements.

3.5.3 Transmission Electron Microscopy (TEM)

The resolution of a modern TEM has gone down to nanoscale, which allows for the visualisation of very fine crystal structures, grain morphology and orientation of a sample[169, 170]. TEM requires an electron transparent specimen to achieve high quality images, normally <100 nm for inorganic samples and thicker for polymeric specimens, because different from in an SEM that the electrons were reflected, the electron beam needs to go through the sample to form an image. Fig. 3.4 shows the typical layout of a TEM. On the top, an emitter generates electrons that are accelerated by the high acceleration voltage (100-200 kV for a standard TEM).

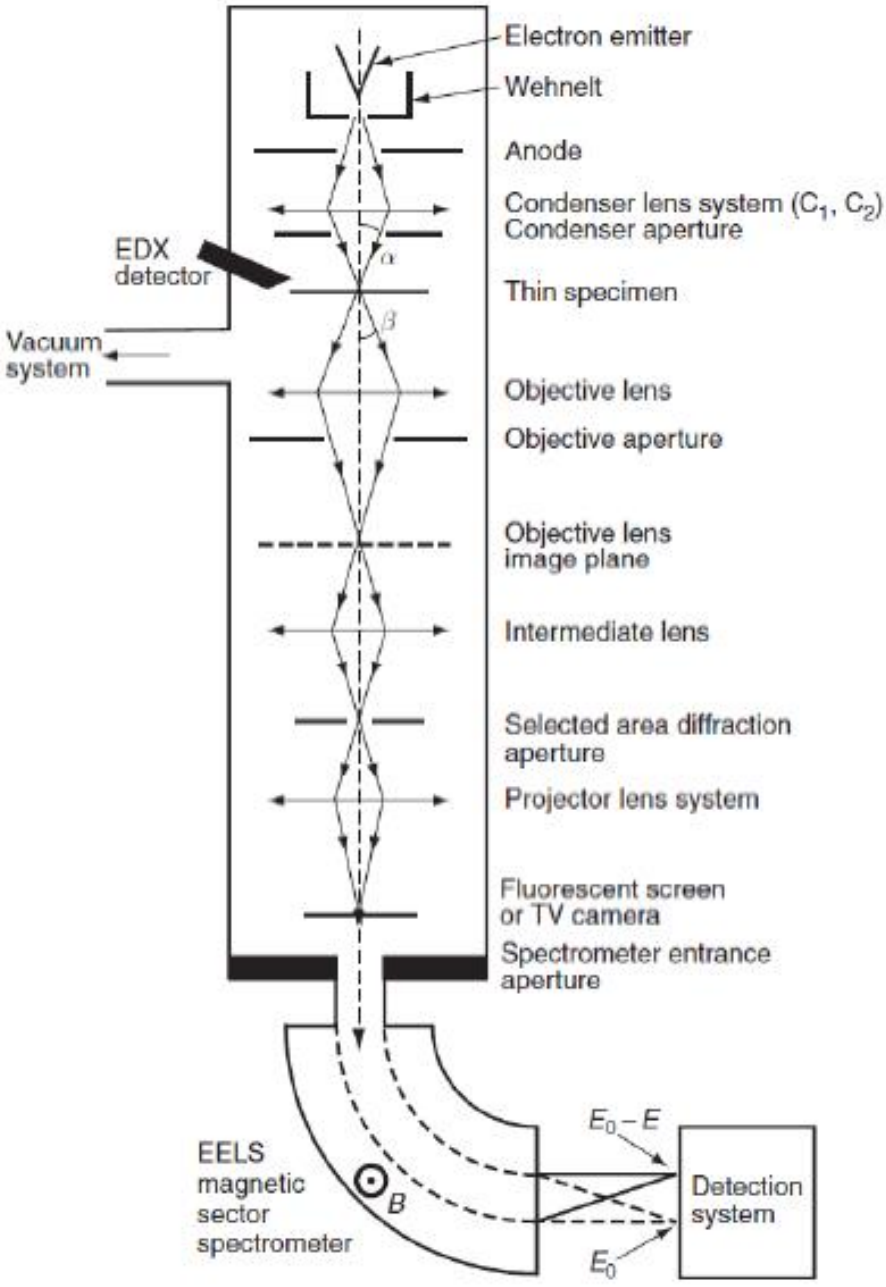

Fig. 3.4 A schematic principle of the TEM[169].

According to the de Broglie Relation, the electron wavelength is decreased significantly by increasing the beam travel speed, which leads to the detection of the sample with high resolution. The high acceleration voltage permits the high-speed electrons to penetrate the specimen effectively. In the imaging process, the electron beam passes the condenser aperture and the objective aperture, to create an image of varied signal intensity and contrast. Based on the location of the objective aperture, a bright field image or a dark field image (image of the specimen structure or diffraction patterns) can be acquired.

Selected area electron diffraction (SEAD) has applied to crystallographic analysis because the accelerated electrons show the wave-like property and the wavelength will be comparable to the space between atoms. The atoms in crystal will diffract the high energy electrons. The oxford instrument made EDS was also used during the TEM observation.

A JEOL 1400 microscope and a JEOL 2100-F TEM microscope were used in this thesis, and both equipped with a LaB6 filament. The former was operated at 120 kV to avoid polymeric sample damages, whilst the latter was operated at 200 kV for general samples to achieve high resolution images.

For powder samples, a tiny amount of the powder was dispersed into 5 ml ethanol and treated with ultrasonic bath for 15 min to achieve a uniform suspension. A few droplets of the prepared suspension were dropped onto a 3 mm diameter holey carbon-coated Cu grid (250 mesh, Agar Company).

For polymeric nanocomposite samples (both Nylon and PEEK composite), the images were obtained on the JEOL 1400 TEM, as these polymers are quiet sensitive to high energy electron beam and could be burnt during observation. The samples were cut on a microtome machine with a diamond blade into less than 100 nm thick thin films, which were then mounted onto bare copper grids, and dried in the oven at 70 ^{o}C overnight before testing.

3.5.4 Raman Spectroscopy

Raman spectroscopy is a powerful technique to evaluate the structural features of a sample by examining the vibrational, rotational, and other low-frequency modes[171-173]. Fig. 3.5 shows the schematic of how a Raman spectroscopy works. Different ranges of laser beams will excite different molecular interaction vibrations which can reveal the up or down shifts of their corresponding energy levels. When a beam of light hits the sample, most of the photons are elastically scattered and their frequencies are corresponding to the incident photons. This is also called the elastic scattering, and only a small fraction of photons (less than 1/100) is scattered with different frequencies, which are usually lower than that of the incident photons. A Raman microscope uses a pulse laser focusing

onto the surface of the sample, and by detecting the scattered light an image or spectrum profile can be obtained.

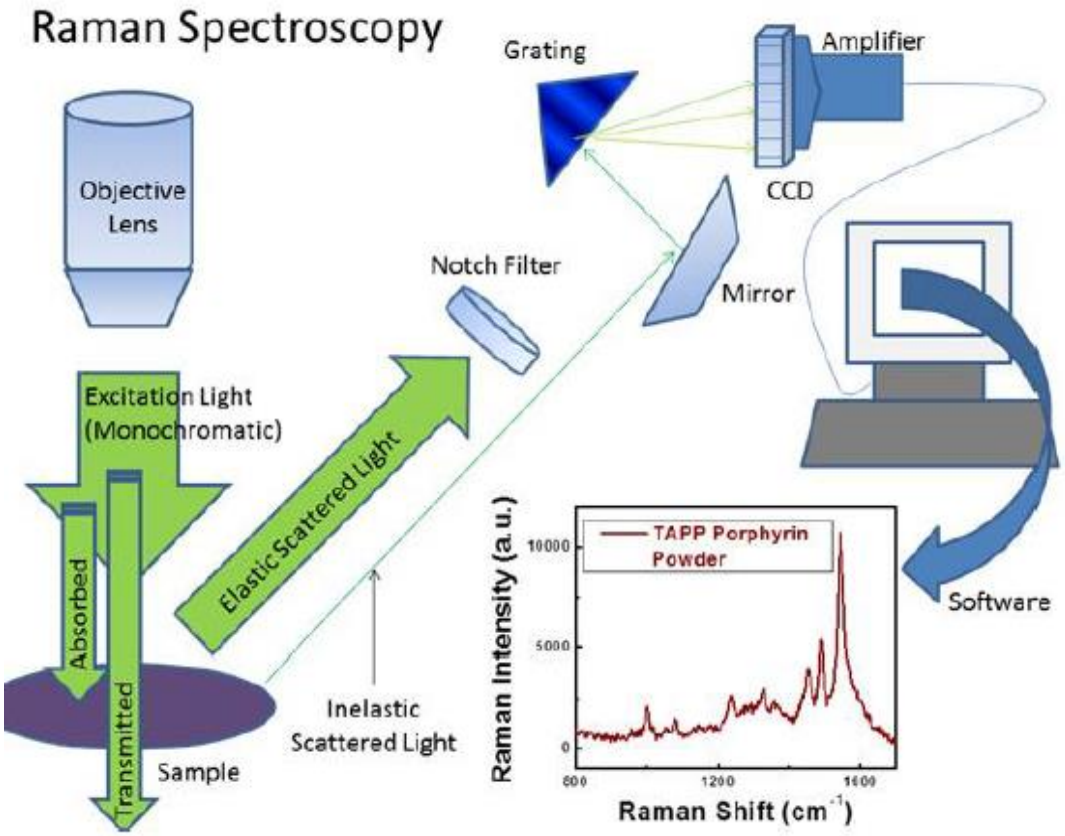

Fig. 3.5 Schematic layout of a Raman spectroscope[171].

This project used a Renishaw-1000 Wooton-Under-Edge Raman microscope in this research. It has a 532 nm laser source, a 40× optical microscope objective lens, and is capable of a spectral resolution of 1 cm^{-1}.

3.5.5 Fourier Transform Infrared Spectroscopy (FTIR)

For polymeric materials, the Fourier transform infrared spectroscopy (FTIR) is a useful technique for characterisation[174, 175]. It can detect the absorption or transmission through the sample to obtain a spectrum. Upon the infrared radiation penetrating through the sample, some of the electromagnetic waves will be absorbed by certain functional groups inside the samples. The resulting characteristic spectra of a sample can be recognised as a unique molecular

fingerprint. In Fig. 3.6, the infrared laser lights were modulated in the interferometer to be the coherent light, and after passing through the target sample in the sample chamber, the spectrum was obtained by the light detector at the end.

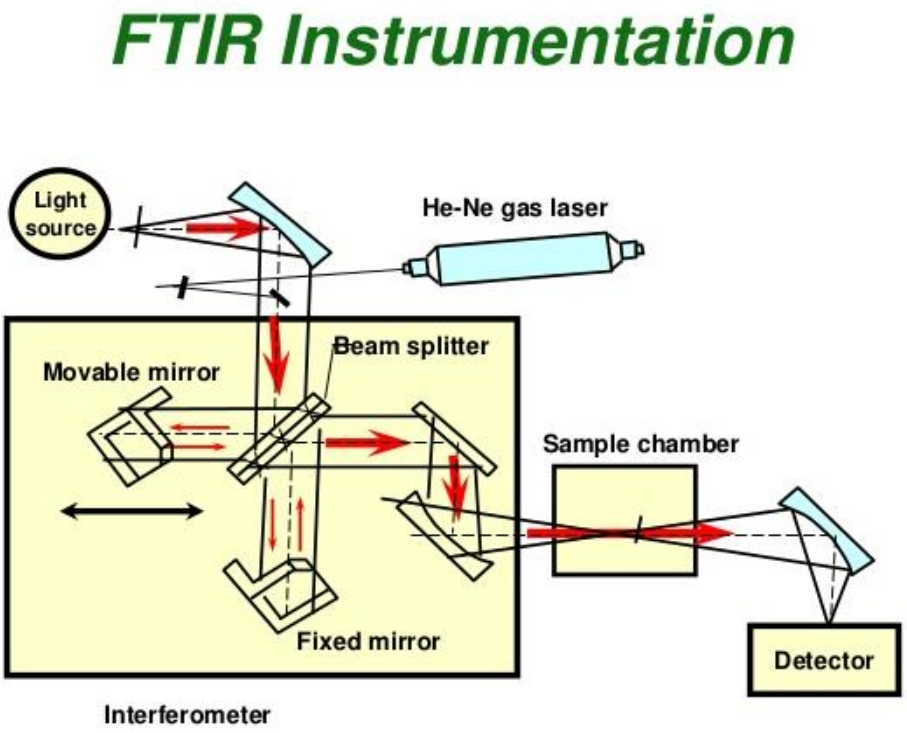

Fig. 3.6 Schematic of the layout of an FTIR spectroscope[174].

The FTIR spectra were acquired by using an Alpha Bruker system in this thesis. The machine was operated in the range of 500 to 3000 cm^{-1} to acquire the FTIR signals. For the FTIR measurements, I used thin film disks of 2 mm diameter and 50 μm thick.

3.5.6 Micro Computed Tomography Scanning (Micro-CT)

Computed tomography can reconstruct the X-ray reflected signals into a cross-section image of a real three-dimension object without damaging the original structure[176]. By stacking each cross-section image together, it recreates a virtual 3D-object. In Fig. 3.7, the X-ray will pass through the sample and display one set image on the detector with a certain cross-section, and by rotating the sample and assembling each image into a whole picture according to the designed computer system a 3D image will be created. As a non-destructive

method, the resolution of pixel size is depending on the light source and scan rates, from micro down to nanoscale.

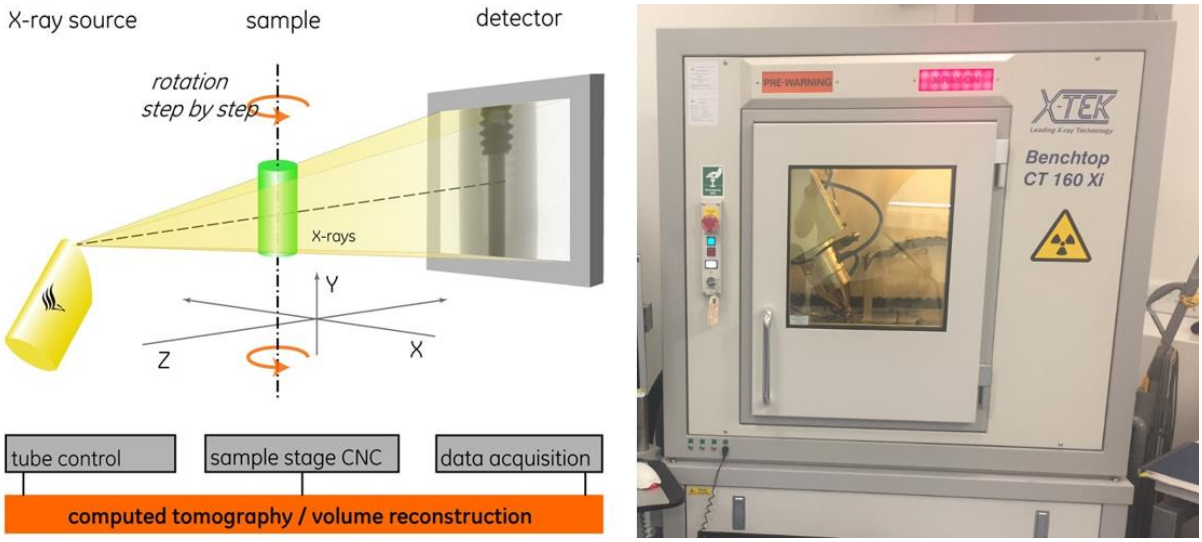

Fig. 3.7 A schematic of the principle of a Micro-CT (left) and a picture of the Benchtop Micro-CT 160 Xi scanner[176].

In this context, a Benchtop Micro-CT 160Xi scanner was utilised to investigate the porosity and the nanofiller distributions in the nanocomposites. Due to the light scattering effects of the heavy metal oxide fillers used in this thesis, although the dimension of the filler falls to nanoscale, it is possible to obtain a convincing particle distribution characteristic for the composites.

3.5.7 Atomic-Force Microscopy (AFM)

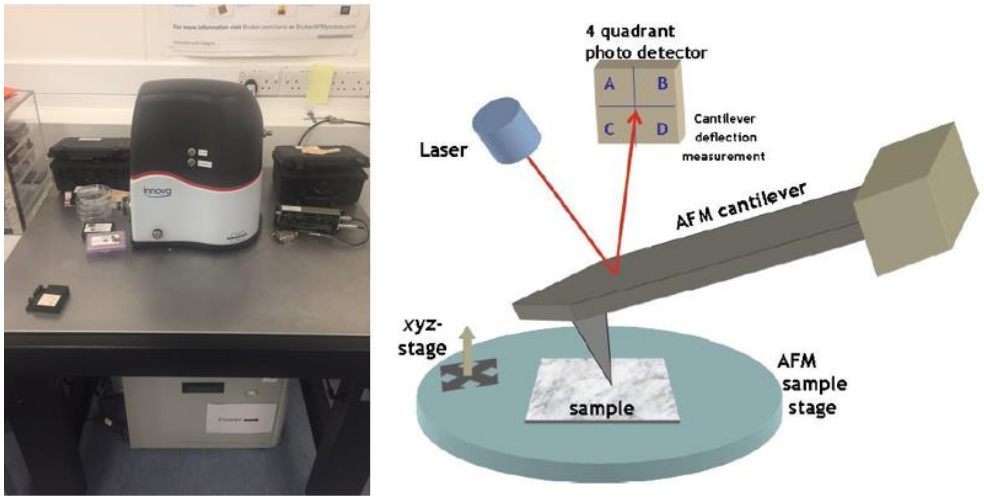

Fig. 3.8 A Bruker Veeco di-Innova AFM and its schematic principle[177].

AFM is a convenient non-destructive technique for investigating the surface morphology of materials, and it can achieve longitudinal resolutions ranging down to nanoscale[177]. Between the AFM and a sample, a tiny sensitive probe is precisely controlled both vertically and laterally to scan along the target position area of the sample. By recording the interface forces between them, an image can be constructed. Four primary imaging modes can be classified, including the contact, non-contact, tapping and lateral force mode.

In this thesis, a Bruker Veeco di-Innova AFM was used in the investigation, under the tapping mode. In Fig. 3.8, the tiny probe head was scanning the surface of the sample, and then the small movements caused by the surface undulation in the vertical direction were recorded by the laser light lever to amplify the signal change, and finally the physical signals were translated into the surface morphological image by the computer software.

3.5.8 X-ray Photoelectron Spectroscopy (XPS)

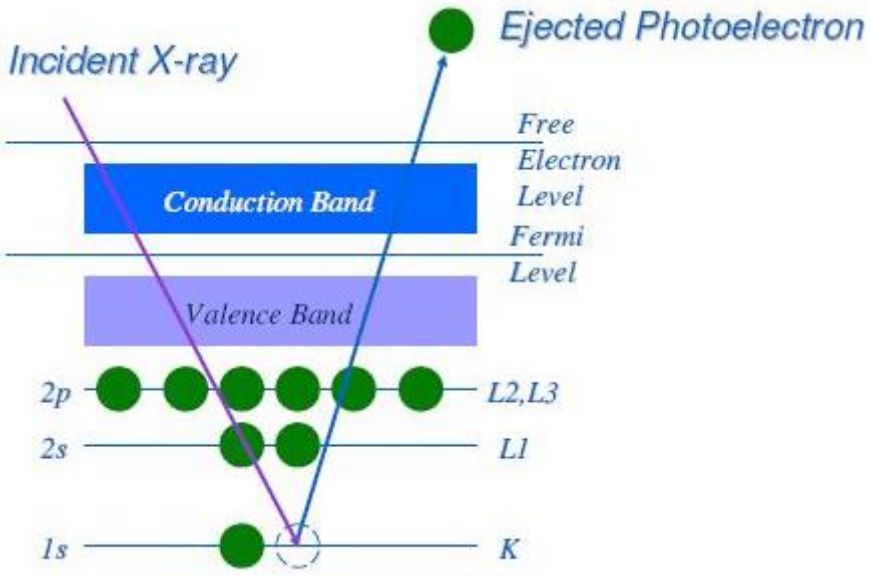

Fig. 3.9 A schematic of the XPS[178].

XPS is a spectroscopic technique that is used for non-destructive surface-sensitive elemental analysis for a wide range of materials[178]. Fig. 3.9 shows that when the surface of a sample is excited by a monochromatic Al-Kα X-ray beam it emits photoelectrons whose binding energy can be recorded and measured

using an electron energy analyser. The emission is very shallow, with a depth of top 0~10 nm. The binding energies and peak intensities of photoelectron can determine changes of the element state and chemical valence on the surface of the sample.

In this experiment, the XPS spectra were recorded on a VG ESCALab Mark II photoelectron spectroscope, at The University of Nottingham. An Al K-alpha X-ray was used as the excitation source with a wavelength of 1486.6 eV, working at an emission current of 20 mA with anode potential of 12 kV. A 40× optical lens was involved, which can confirm and choose the certain testing area. The sample was cut into 0.5 ~ 1 cm^2 in size which was placed to be analysed side up and X-rays were displaced onto the middle area of the sample to make the measurement accurate.

3.5.9 Ultraviolet–visible spectroscopy (UV-Vis)

Ultraviolet–visible (UV-Vis) spectroscopy detects the absorption or reflectance spectrum of a sample in the selected spectral region[179]. By measuring the intensity difference between the light before passing (Io) and after passing through the sample (I), an absorption spectrum can be recorded. Different light source depending on the wavelength can be used to achieve different range of spectrum, such as visible, near-ultraviolet and near-infrared.

This technique is particularly applicable to carbon based materials, because both the π-electrons and non-bonding electrons (n-electrons) contained in the molecules can absorb the spectrum energy from the ultraviolet range to visible region. However, various excited molecules have photo emissions with different lower or higher energy, which can be marked as the fingerprint peak. Bother liquid or solid samples can be investigated using this technique.

In this thesis, a liquid sample was measured. First, a small amount of nanoscale powder was dispersed into ethanol solution to create a very dilute suspension. After sonication to further disperse the particles in the solution, the suspension was investigated under the absorption mode. The wavelength ranging from 280-700 nm was measured using a Jenway 6715 UV/Vis spectrophotometer.

3.6 Thermal property characterisation

To investigate the carbon content, thermal stability and thermal conductivity of the resulting nanocomposites, a series of thermal physical properties can be obtained by the thermal analytical devices.

3.6.1 Thermogravimetric analysis (TGA) and differential scanning calorimetry (DSC)

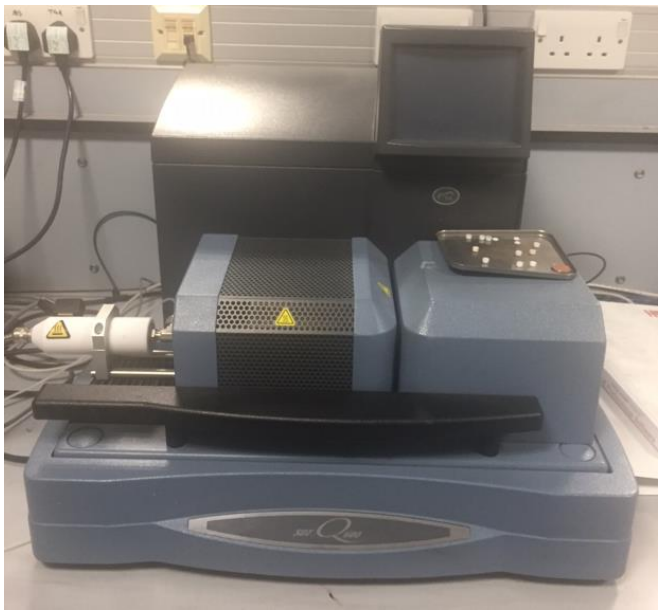

Fig. 3.10 The TGA SDT-Q600 machine (TA instrument).

Thermal analysis can offer information on the thermophysical properties of a material. The most commonly used thermal analysis techniques are the thermogravimetric analysis (TGA) and differential scanning calorimetry (DSC), and they measure the mass and heat variations with changing temperature, respectively[180, 181]. The TGA shows the weight-temperature dependant feature of a material, whilst the DSC reflects the heat differences between the sample and a reference at various temperature points. They are powerful techniques to assess materials' thermal stability, specific capacity, phase change, decomposition features, *etc*.

In this thesis, a TGA Q600-SDT instrument was used in my investigations, which can obtain the DSC data at the same time. The main working part is displayed in Fig. 3.10 with 2 separable heating chambers (blue blocks) and ceramic gas guiding head to the MS if necessary (white one on the left).

For each testing, a sample of approximately 10 mg was heated from room temperature up to 800 °C, with a heating rate of 10 °C/min under an air flow rate of 100 mL/min. The resulting data points were analysed using the TA USA Instruments software, *Universal Analysis 2000*.

3.6.2 Thermal Conductivity Analysis (TC)

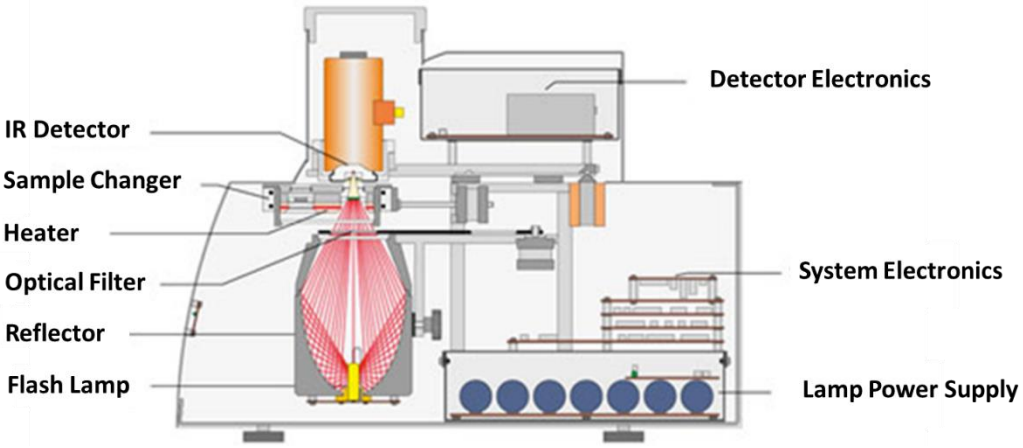

Fig. 3.11 A schematic of the Laser Flash Analysis (LFA) and the actual NETZSCH LFA 467 HypeFlash machine[182]

In this work, a NETZSCH LFA 467 HypeFlash machine (Germany) was used to evaluate the thermal conductivity of different polymeric nanocomposites[182]. The Laser flash analysis (LFA) method can acquire the thermal diffusivity data for various materials, which measures certain portion of energy before and after passing though the target sample. Fig. 3.11 shows the infrared detector cooled by liquid nitrogen on the top to obtain the thermal signal. The machine records the accurate energy changes of the flash beam from the bottom flash lamp and reflector passing through the sample in different designed temperatures. Furthermore, we could calculate the thermal conductivity with density and thickness inputs. However, the thermal conductivity is strongly temperature-dependent, because the thermal energy can be more easily transferred to heat to some extent.

For those composite samples, MOx@C-nylon 12, IF-WS_2/PEEK and IF-WS_2@C-PEEK were cut by a narrow band saw into 10 mm × 10 mm squares for the NETZSCH LFA 467 assessments. The surface and edge of the squares

were polished using mesh 600 sandpaper to achieve a thickness of *ca*. 0.5 mm to fit in one set of specimen holder. Prior to measurement, the samples were coated with a thin graphite layer via spraying graphite aerosol (200ml, GRAPHIT 33, Kontakt Chemie CRC Industries) onto them.

3.7 Mechanical property assessment and other.

The mechanical property assessments refer to tensile strength, Young's modulus, Vickers Hardness, as well as tribological performance, of both resulting Nylon-based and PEEK-based nanocomposites[183, 184].

3.7.1 Tensile test

The tensile property assessments were conducted on a Lloyd Instrument EZ20 universal tensile testing machine, using a load of 100 N. During the test, we applied a loading speed of 3 mm/min, and 5 test specimens were prepared for each sample of different concentrations of filler. The specimens were prepared to form a dog-bone shape, with a size of 50 mm × 5 mm × 2 mm. Prior to test following the ASTM D638 standard (1 mm < thickness < 14 mm, Gauge length 25~50 mm), to ensure the consistency of the testing results, all specimens were polished by using 600 mesh sandpapers to remove obvious surface defects. The tensile test can lead to the ultimate tensile strength, Young's modulus, and strain information of the specimens.

3.7.2 Vickers Hardness test

Bulk composite samples with a size of 35 mm × 25 mm × 5 mm were used to evaluate their hardness feature, A Leco V-100-AZ Vicker Hardness Tester was utilised in this context, because the Vickers Hardness testing has a large measurement range therefore it is especially suitable for polymer-based materials. A load of 500 g and a dwell time of 25 s were the test parameters. 5 repetitive measurements were recorded at room temperature for each specimen.

3.7.3 Tribological performance

A self-made rotary plate tribology testing machine at X-AT laboratory was used to appraise the tribological performance of the composites. The samples were cut into the size of 2 cm × 2 cm ×1 cm from the hot-pressed blocks which were finished by polishing using the 600-mesh sandpapers. The testing conditions were as follows: applied load, 200 N; linear testing speed, 2.70 m/s (500 rpm); testing time, 10 min; testing environments, ambient (20-25 ºC); lubricating condition, dry wear. The test for each sample was run at least 3 times.

3.8 Electrical conductivity measurement

The condensed bulk is prepared by using a small bench top press machine with loading of 15 tons in the mould, which is 20 mm in diameter and the pressure is applied to 50 kN. After measure the height of the specimen, connecting two copper sides with a multi-meter to each side individually, for 5 times.

3.9 Summery

The materials, experimental procedures and the equipment for the C-coated nanoparticle and the nanocomposite fabrication were described in the early part of this Chapter. The key techniques, as well as their working principles for the characterisation of morphological, structural and compositional features, have been introduced. Further techniques to appraise the thermophysical properties such as thermal stability and thermal conductivity of the nanoparticles and nanocomposites have also been discussed. Finally, the generic methods to evaluate the mechanical properties of the composites, in addition to the sample preparation methods, have been summarised.

Chapter 4. Synthesis of carbon-coated metal oxide (MO_X@C) nanoparticles

4.1 Introduction

As one of the most studied materials, new structures of carbon have attracted enormous research interests owing to their excellent thermal, mechanical, optical and electrical properties. These properties provide great potentials in the fields of solid lubricants, supercapacitors and battery electrodes, nanodevices and composites for engineering applications[53, 64, 80, 185, 186]. Metal oxides have super hardness and richness in material choices owing to their highly thermal and chemically stable features. They have been widely applied in catalysis, photoluminescence, composites, thermal-resisting, semiconducting industries, and in surface protection from acid and alkali corrosions. The joining of carbon and metal oxides could therefore combine the advantages of both materials in terms of their chemical, physical and mechanical properties, and therefore the investigation into such combinations in the bulk quantity of nanomaterial forms will be the subject of this chapter.

In this study, we will investigate the full potential of the RCVD process, extend and explore the C-coating in a wide range of interesting micro- or nano-sized non-magnetic metal oxides, including MO_X (M = Ce, Cr, Zr, Y, Ti and Zn, where X = 1, 1.5 and 2). We then further demonstrate the actual advantages of the resulting MO_X@C composite NPs in example polymeric composites, against the un-coated NPs. Nylon 12 has been chosen for this study because of its superb ability of loading reinforcing materials, with many examples for comparison, including carbon fillers such as CNTs and graphene.

4.2. Rotary CVD system modification----Objectives and technical requirements

The existing RCVD system that was used to synthesise IFs based on Xu's design has been modified in this work to suit for our purpose of large scale coating of NPs. In Chapter 3, we have shown both the original and modified designs. The middle part of the system is a traditional static furnace with a long quartz tube being fitted within the furnace, which is gas-tight sealed at both the

feeding end and the collection end. The rotation of the quartz tube is driven by a speed-controllable motor via the motorised rollers. A mechanical rotation is applied to the quartz tube and the particles sitting inside will be shaken and separated by the physical rotation movement of the tube, due to the friction forces generated between the lateral driven force and the gravity force, which would anti-counter the self-agglomeration and avoid sintering of the nanoparticles at high temperatures.

4.2.1 Dynamical balance control system

In the original design, the tilt angle of the quartz tube can only be controlled by the inlet part, which limits the speed of particle movement from one end marching to the other end of the furnace. In the modified system, the height of the motorised control part (outlet part) could also be easily changed by using bases of different thicknesses. Therefore, both the inlet and outlet ends could contribute to the height control of the quartz tube, either separately or jointly, to allow for the tilt angle change expanded from -5 ~ +5° to -8 ~ +8°. This improvement would allow more efficient particle production and add more versatility to our system. Fig.4.1 shows the replaceable block bases for different height requirements.

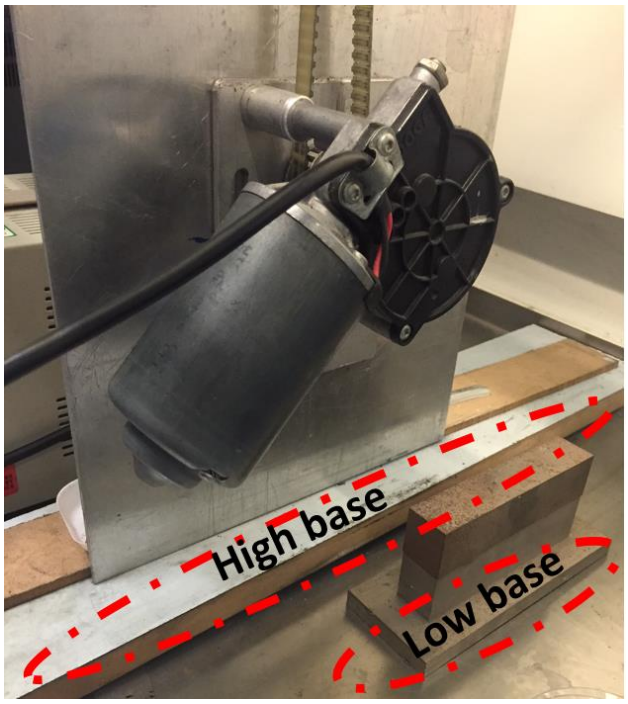

Fig. 4.1 The modified balance base at the outlet end.

4.2.2 The collection system

Because of the light weight of the MO_X@C NPs, they are prone to be blown out of the hot-zone, which will lead to incomplete reactions. A stopper has been designed and installed to avoid this happening, which will also stop NPs prematurely moving over to the collection part. Without this procedure, we found that in the continuous synthesis process of the NPs, some NPs would jam the outlet gas pipeline, causing accidents. The flexible homemade Al stopper therefore can stop the NP products blocking the gas pipelines, ensuring the free flow of the protective/reactive gases though the pipeline, and safeguard the realisation of the desired reaction to complete. In Fig. 4.2, a homemade Al particle stopper is shown, and it picot edge will fit the tube wall perfectly and hole in the middle allows for the gas to flow through.

Fig. 4.2 The homemade Al particle stopper.

4.2.3 Carbon source feeding system

In the original design, the diameter of carbon source injection pipe is about 1 mm. However, the injection rate of the carbon source is ranging from 1 to 2 ml/h. The tremendously low injection rate makes the movement of liquid carbon source (styrene + acetone) very slow in the syringe pipe, which means that the gas vaporization during the liquid transportation was uncontrollable due to the

surface tension at the end of the syringe pipe. As shown in Fig. 4.3a, we therefore applied a thinner diameter (0.2 mm) pipe to improve the feeding efficiency of the RCVD system. Furthermore, displayed in Fig. 4.3b, an extra switch at the inlet of the H_2 mass flow controller has been added to stop potential leakage from this part, with added safety than the original design.

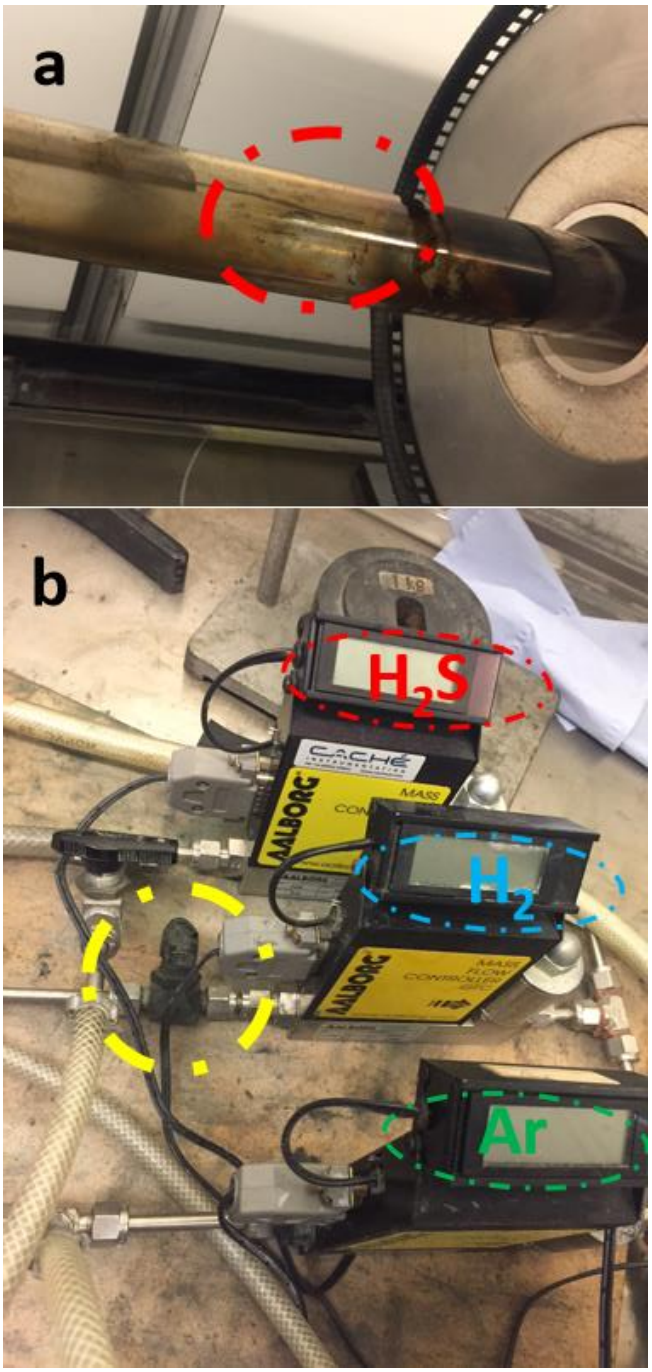

Fig. 4.3 a) The thinner injection pipe (Red circle); b) the extra switch before the inlet part of H_2 mass flow controller (Yellow circle)

4.3 Investigation on the synthesis of MO_x@C NPs

Various C-coated metal oxides were prepared by using the modified RCVD system. Prior to the CVD process, 10 g of different metal oxide NPs were dispersed respectively into 100 ml ethanol under vigorous magnetic stirring for 1 h without any surfactant, followed by ultrasonic probe dispersion for 30 min. The resulting suspension mixture was first dried at 80 ^{o}C in a long tube furnace (VecStar Ltd.) to obtain dry powder, which was then ground in an agate mortar to eliminate the bulk residual, and finally transferred into the inlet part of the long quartz tube (2-meter-long with an inner diameter of 35 mm).

The carbon precursor was prepared by ultrasonically mixing of acetone and styrene solutions with a volume ratio of 4:1. The reaction zone of the system was sealed by the designed rotary seals at both ends. The rotation system was started with an Ar flow of 100 ml/min, and 1 to 2 ml/h of the carbon precursor was introduced into the reaction zone for 10 min to 1 h, at temperatures varying from 600 to 1000 ^{o}C, and then naturally cooled down to room temperature under Ar protection. After the RCVD process, a controllable layer of carbon, depending on the reaction duration and temperature, precursor concentration and gas flow rate, *etc.,* was deposited. Various parameters have been investigated in this Chapter in order to achieve high quality coating. MOx, such as TiO_2 or ZnO, was used as the model metal oxide for the synthesis condition optimisation, and the optimised conditions were adopted for the synthesis of other metal oxides.

4.3.1 Graphitisation level *vs* temperature

Temperature is an important parameter for the CVD method. In our experiments with temperatures ranging from 600 to 1000 ^{o}C for 5 min, we found that the thickness of C-coating did not show much change. However, the graphitization level of the coating became much improved at higher temperatures, which was supported by the XRD, TGA and Raman results. On one hand, it is obvious that higher temperature would result in better graphitic structure. On the other hand, too high temperatures would not benefit the actual graphitic crystallization during our RCVD process, because violent decomposing of the liquid styrene

carbon source at higher temperature could lead to a negative influence on the ordered carbon formation. In Fig. 4.4, the HRTEM images of the C-coating on TiO_2 obtained at different temperatures are shown. It is obvious to find from the TEM image in Fig. 4.4a, the carbon coating layer synthesised under 700 ^oC showed the discontinuous distribution. Also that amorphous carbon without clear lattice pattern is clear, because of the rapid carbon accumulated instead of well-graphitised carbon forming under 900 ^oC. Hence, the optimized temperature in this research is around 800 ^oC.

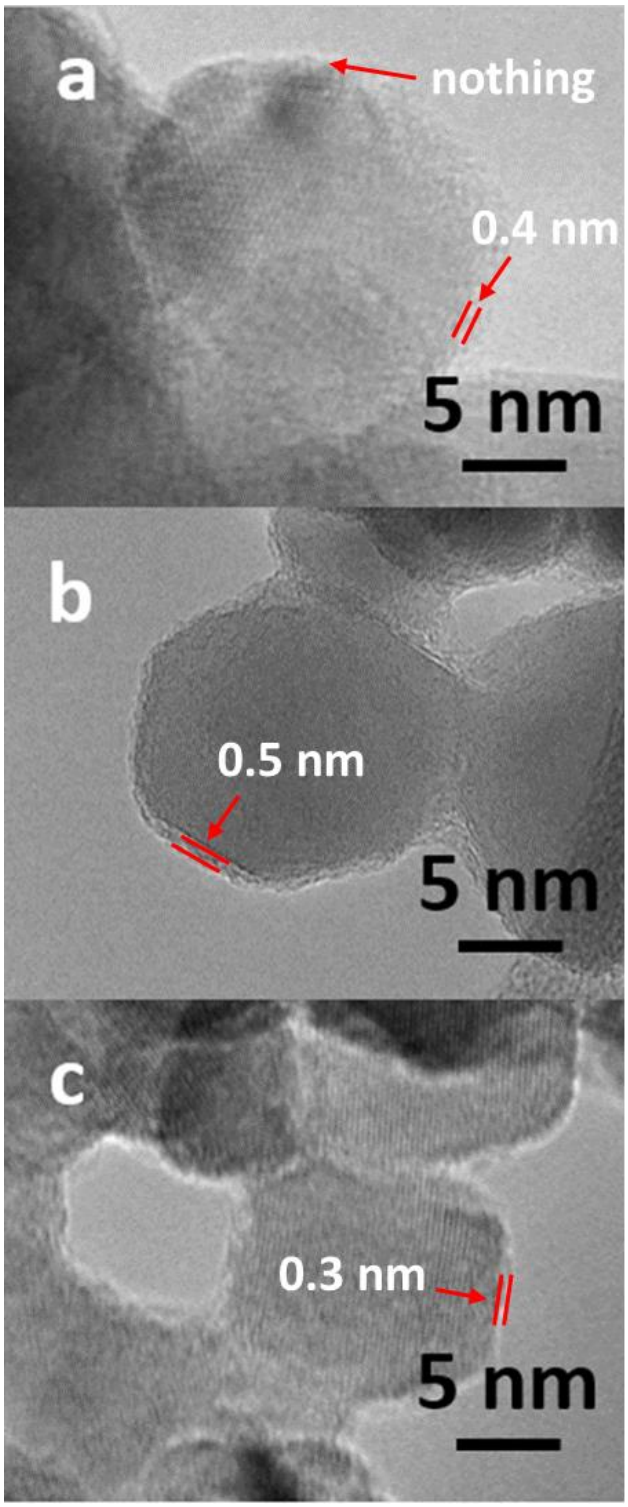

Fig. 4.4 TEM images of the C-coating on TiO_2 obtained at different temperatures: a) 700 ^oC, b) 800 ^oC, and c) 900 ^oC

4.3.2 C-coating thickness *vs* reaction time

The coating thickness in a CVD process is generally considered to have almost a linear relationship with the reaction time, or at least the deposit formed on the

substrate will grow continuously with prolonged reaction time, until reaching a certain limit[30, 31]. Therefore, by controlling the reaction time, the desired thicknesses of the C-coating on the MO_x particles can be successfully achieved.

By using the control variate method, we the prepared samples in the rotary furnace at 800 ^oC and a carbon source supply rate of 2 ml/h, with a reaction time of 5, 10, 30 and 60 min respectively. The TEM images in Fig. 4.5 show that the 5 min and 10 min samples exhibit a thin and uneven layer of coating on the MO_x surface. Longer than 30 min, the sample exhibits a smooth and complete coating around the contour of the particle, with a thickness of about 2 nm (Fig. 4.5c). An attempt explanation is as follows. At the initial stage of precipitation, the tiny carbon fragments were deposited to form a hexagon ring and act as the initial core for further carbon atoms/clusters to accumulate on the surface of the MO_x substrate. Following this stage, the growth would be continued to spread and cover the entire surface to minimise the surface energy. Meanwhile, the localised accumulation and growth to form small multiple layers of graphitic carbon was also possible. Therefore, with short deposition time, the layer is thin and sometimes incomplete. Further extending the deposition time, layer by layer deposition became possible, which is the same mode to the carbon nano-onion growth during a normal CVD process, hence leading to relatively uniform and fully covered coating.

Moreover, in a conventional static CVD process, the MO_x substrate would be laid permanently stacking together, in such a way the gaseous carbon clusters would be virtually unable to access the entire surface of the MO_x, resulting in incomplete coating or severe agglomerations by wrapping multiple particles together, which will be confirmed in the carbon membrane TEM characterisation part later, demonstrated in Fig. 4.7. The RCVD system therefore demonstrates significant advantages to achieve uniform thickness and complete coating. The optimised reaction time for about 2 nm thick coating is between 30 to 60 min, and the resulting product is shown in Fig. 4.5c.

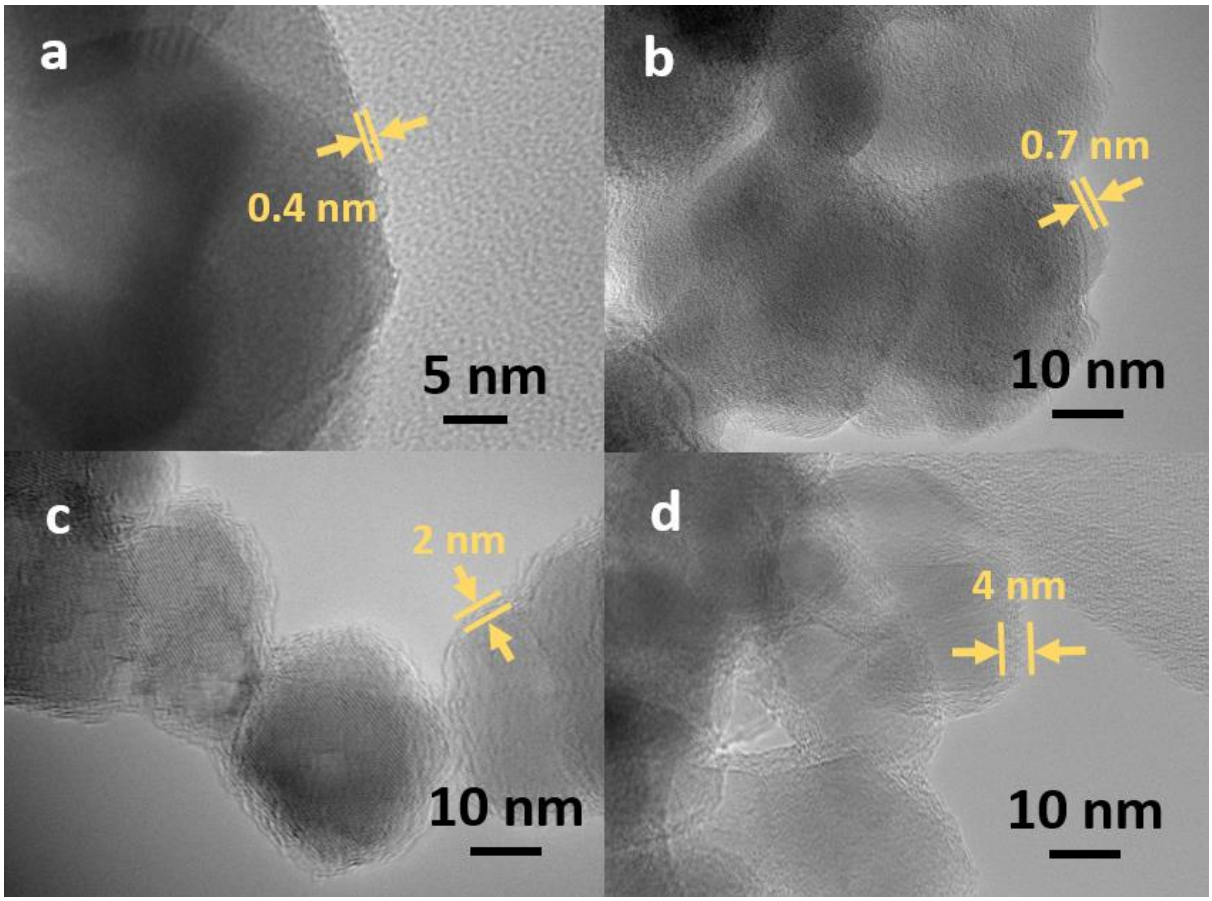

Fig. 4.5 TEM images of C-coating on which metal oxide with different reaction time: a. 5 min, b. 10 min, c. 30 min, and d. 1 h

4.3.3 C-coating thickness *vs* injection rate

A series of experiments of different injection rates of the styrene carbon source was also investigated, to find out the optimal parameter for achieving a thin and uniform coating[31]. The conditions used to investigate the influence of thickness of TiO_2@C are: 20% styrene, the reaction time between 30 to 60 min, at 800^{o}C, and under Ar. Hence, based on those data, the effect of carbon resource injection rate was further studied.

In the RCVD system, our design made sure that the carbon source solution evaporated as soon as it was injected into the furnace by reaching a pre-set high enough heating zone. To study how the injection rate affects the thickness of the C-coating, we used the following combinations of flow rates and deposition time: 1 ml/h and 2 ml/h for 10 min, and 1 ml/h and 2 ml/h for 30 min, respectively. The first 10 min maybe the initial stage for deposition, so there is

not any carbon deposition formed. As shown in Fig. 4.6 of the TEM images, the most interesting difference is happened in the 30 min deposition process. The quicker injection rate leads to a thicker C-coating, which has increased the efficiency of reaction time.

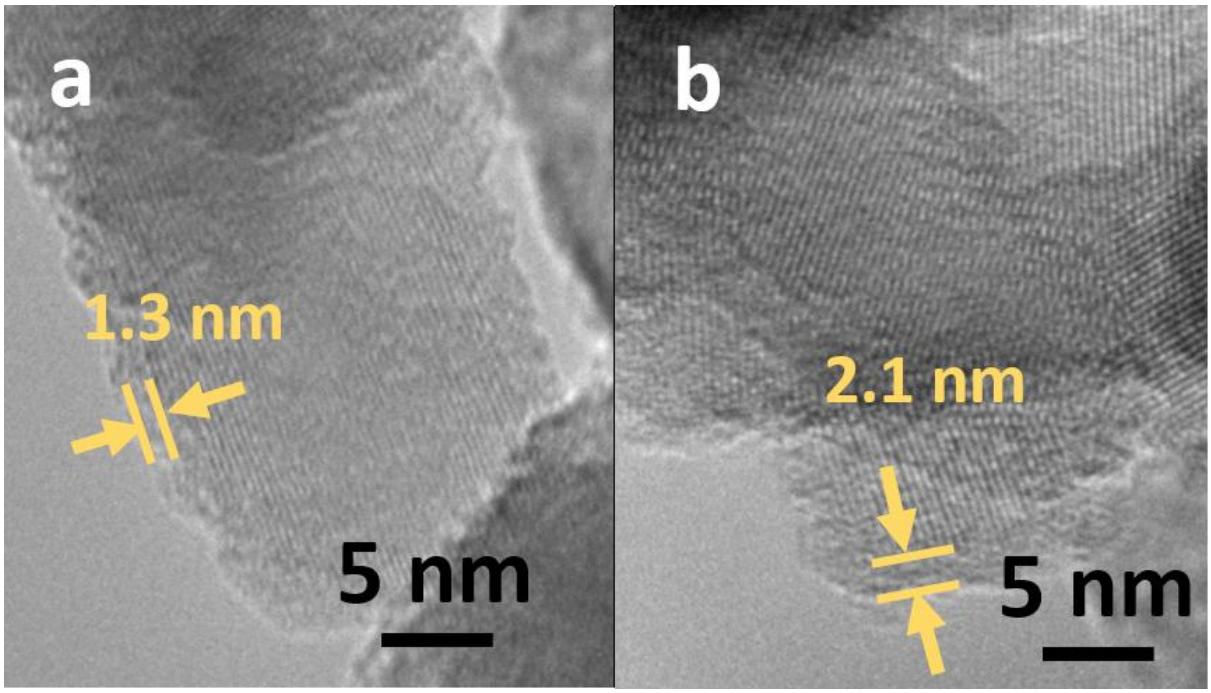

Fig. 4.6 TEM image of the C-coating on TiO_2@C. a. 1 ml/h with 30 min, and b. 2 ml/h with 30 min.

4.3.4 Pure graphitized carbon membrane

We have further demonstrated the uniform feature of the carbon shell by completely removing the ZnO core of ZnO@C NPs. The ZnO@C NPs were re-heated at 800 ^{o}C under H_2 flow, which resulted in the reduction of ZnO to metal Zn. The metal Zn evaporation left behind the carbon shells. The resulting shells are displayed in Fig. 4.7a. The majority of the empty shells exhibits an individual, complete and spherical characteristic that resembles the size and shape of the original ZnO NPs, whilst a few shells show an irregular and large structure. These large shells must have formed from two or three adjacent particles that were wrapped together. It is noteworthy that although not all the NPs are sheathed individually during the RCVD, nevertheless the overall quality of the coating is very high. Otherwise, the coating will just form a single whole shell

around the out edge of the agglomerated particles like in the static furnace (Fig.4.7b). As presented above, all the metal oxide particles are at nanoscale, which makes them prone to agglomeration at high temperature, leading to the formation of bulk coating containing a number of particles. This is one of the challenges for scale-up the production of NPs beyond laboratory level with conventional techniques. In this regard, the novel RCVDs can effectively prevent the particle agglomeration and generate individual MO_X@C NPs at large scale without damaging the original structure of the metal oxide particles. Furthermore, even though the outer shell of carbon could be some amorphous carbon too, there are no many isolated amorphous carbon spheres found as a by-product, which verifies that the chosen RCVD parameters are appropriate for the generation of graphitic coating. This result also further confirmed for results in the XRD and Raman characterisation.

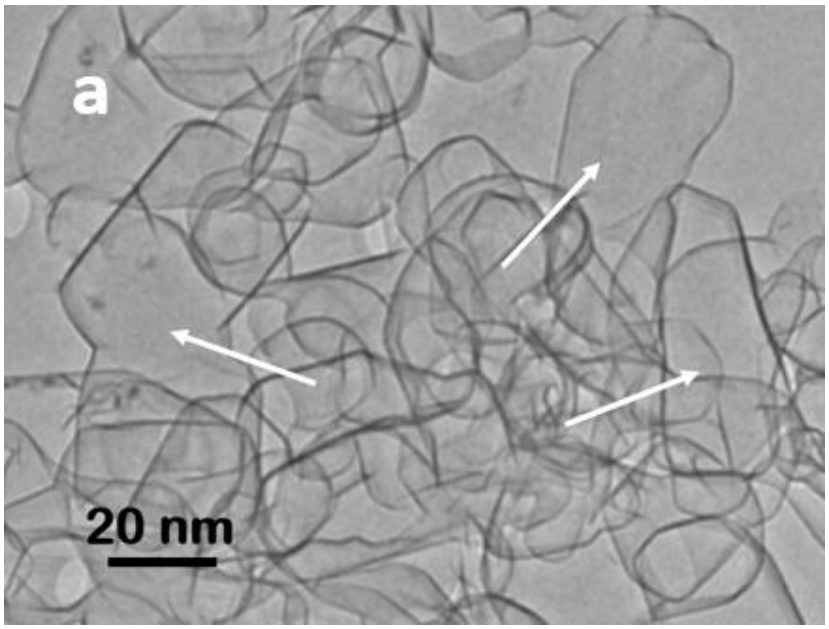

a) Carbon membrane prepared by removal the core of ZnO@C (RCVDs)

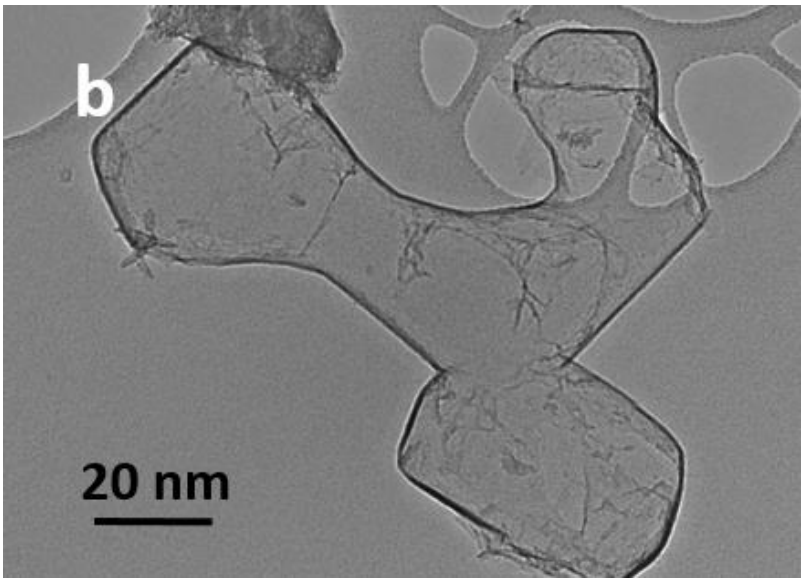

b) Carbon membrane prepared by removal the core of ZnO@C (static furnace)

Fig. 4.7 TEM images of the carbon shell after the removal of ZnO core

4.3.5 Conductivity of the TiO_2@C

The perfectly formed and connective graphitic C-coating could act like a conductive layer, which changes the bulk TiO_2 from an insulator into a conductor. By preparing the condensed bulk of TiO_2@C, a small cylinder consisting of 10 g TiO_2@C sample was compressed by using a mini-portable press machine with loading of 15 tons in the mould of 20 mm diameter and the pressure is near 50 kN and the high of this cylinder was 5.11 mm (Fig. 4.8). The average resistance was calculated as 183.23 (±2.91) Ω at room temperature (for 5 times). Hence, according to the equation of σ =L/RS (L is the length of the piece of material, R is the electrical resistance of a uniform specimen of the material, and S is the cross-sectional area of the specimen), the resistivity is thus 11.22 (±0.19) Ωm and the conductivity σ is 0.0891 (±0.0015) S/m. Compared with the pure TiO_2 sample, the conductivity of TiO_2 has been significantly improved, which is better than most semiconductors. (Density is 2.321 g/cm^3)

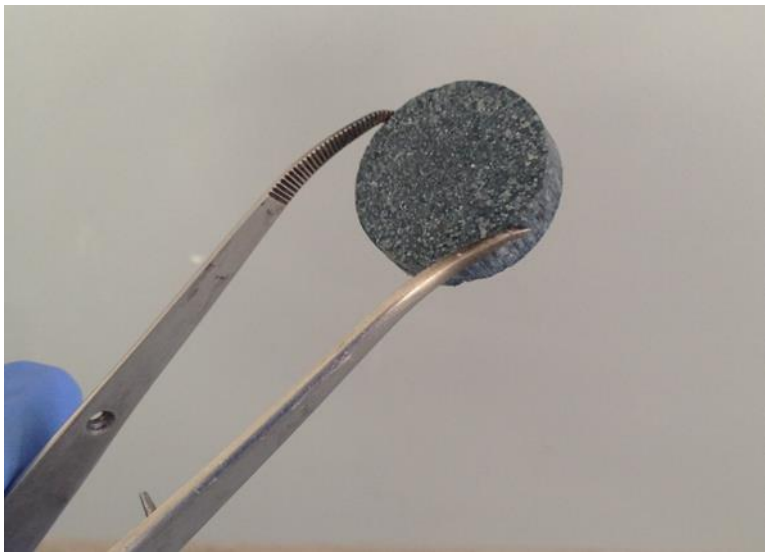

Fig. 4.8 The pressed TiO_2@C sample for electrical property testing (conductivity σ is 0.0891 (±0.0015) S/m).

4.3.6 Coating on other MO_x NPs

Based on the successful synthesis of TiO_2 and ZnO, we further extended this C-coating strategy to other metal oxides, including MO_X (M = Ce, Cr, Zr, Y, Ti and Zn, where $_X$ = 1, 1.5 and 2) under the same conditions of 30 min at 800 ^oC. The structures of the MO_X@C NPs were characterized by XRD, Raman, TEM, EDS, SEM and TGA, respectively.

4.3.7 Characterisation of MO_X@C NPs (XRD, Raman, SEM, TEM and TGA)

XRD

The XRD results are shown in Fig. 4.9a. Compared with the XRD patterns of the original metal oxides, an extra 2θ peak at around 26.2° can be observed for all MO_X@C NP samples. Different from the broad peak showing in amorphous carbon, this sharp peak around 26.2° in the metal oxide composites can be ascribed to the (002) diffraction of graphitic carbon, which suggests a high level of crystallization of the graphitic C-coating[70]. For better view, Fig. 4.9b shows the enlarged peaks from 26° to 27°. Especially, for the TiO_2 sample, the strong peak around 26° being contributed from its (110) overlaps with the (002) peak of graphitic carbon, which results in the sharpest diffraction peak with the highest intensity around 26°. For all samples, the intensity ratio of carbon to metal oxide

is quite low, implying that the amount of the carbon in the MO_X@C NPs is small therefore the coating should be extremely thin. Further confirmation is showed in Raman spectra and TEM characterisation below.

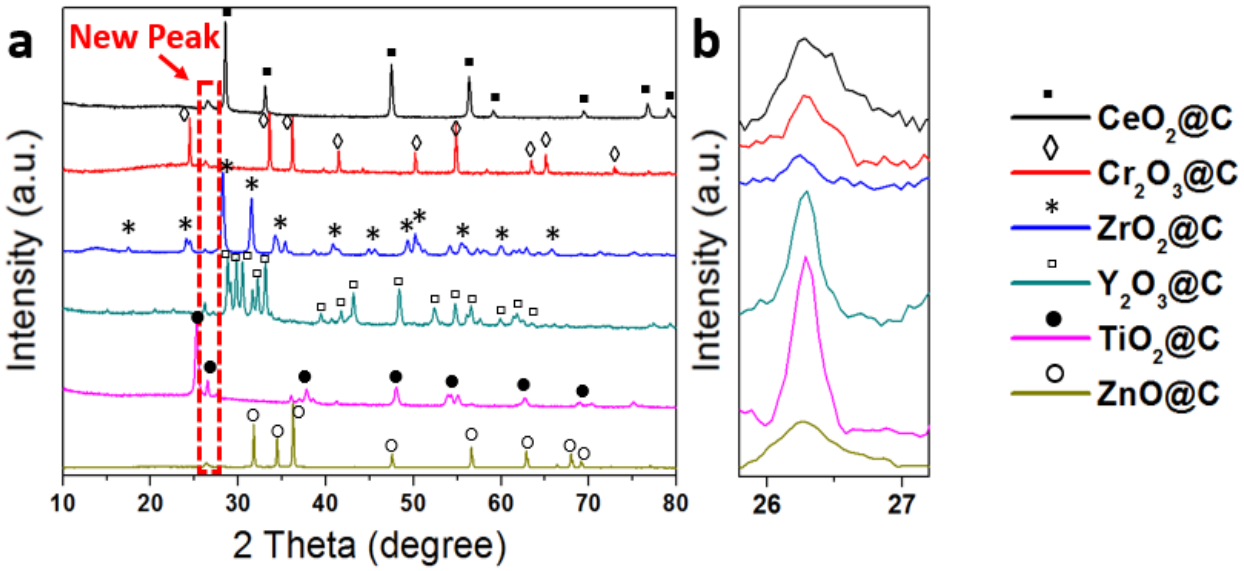

Fig. 4.9 XRD patterns of the MO_X@C NPs.

Raman spectra

The Raman spectra of those NPs are presented in Fig. 4.10. This is the semi-qualitative measurement and each data repeated 3 times with 10% intensity of laser beam and stacked the signal together to remove the influence of background noise. All the MO_X@C NPs show peaks around 1350 cm^{-1} (D band, which comes from the disordered carbon) and 1590 cm^{-1} (G band, which characterises the hybridized sp^2 of carbon), which are originated from the bond stretching of pairs of sp^2 atoms in both chains and rings and sp^2 atoms in the breathing vibration modes in rings, respectively[187, 188]. Therefore, the intensity ratio of D band to G band indicates the crystallization level of the carbon coating, by simply using the intensity value of maximum peak to calculate. *i.e.* the higher the value of I_D/I_G, the more defects the sample contains. Of those MO_X@C NPs, the ZrO_2@C NPs exhibit the lowest I_D/I_G value therefore it retains the highest level of graphitization, followed by the second sample, the Y_2O_3@C NPs, whereas the rest of MO_X@C NPs all show fairly good crystallization level.

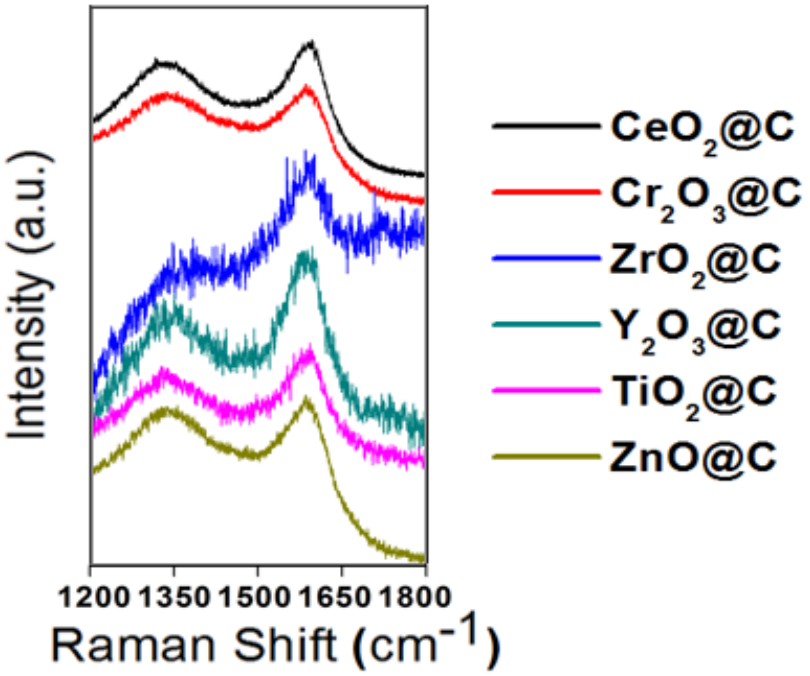

Fig. 4.10 Raman spectra of the MO_X@C NPs

SEM

The ZnO and TiO_2 NPs are the most common used materials in the lab and been chose as the sample for further demonstration. The particle morphologies of the metal oxides before and after the C-coating were examined by SEM to visualise the overall feature of the NPs, and the results of ZnO and TiO_2 are shown in Fig. 4.11. It is obvious that both types of metal oxide NPs exhibit similar particle size distribution, with/without the C-coating. There were no visible morphological differences under SEM examination for all the NPs, suggesting that the RCVD is an effective and versatile way to produce a wide range of C-coated metal oxide NPs, without changing their original morphologies and free of agglomerations.

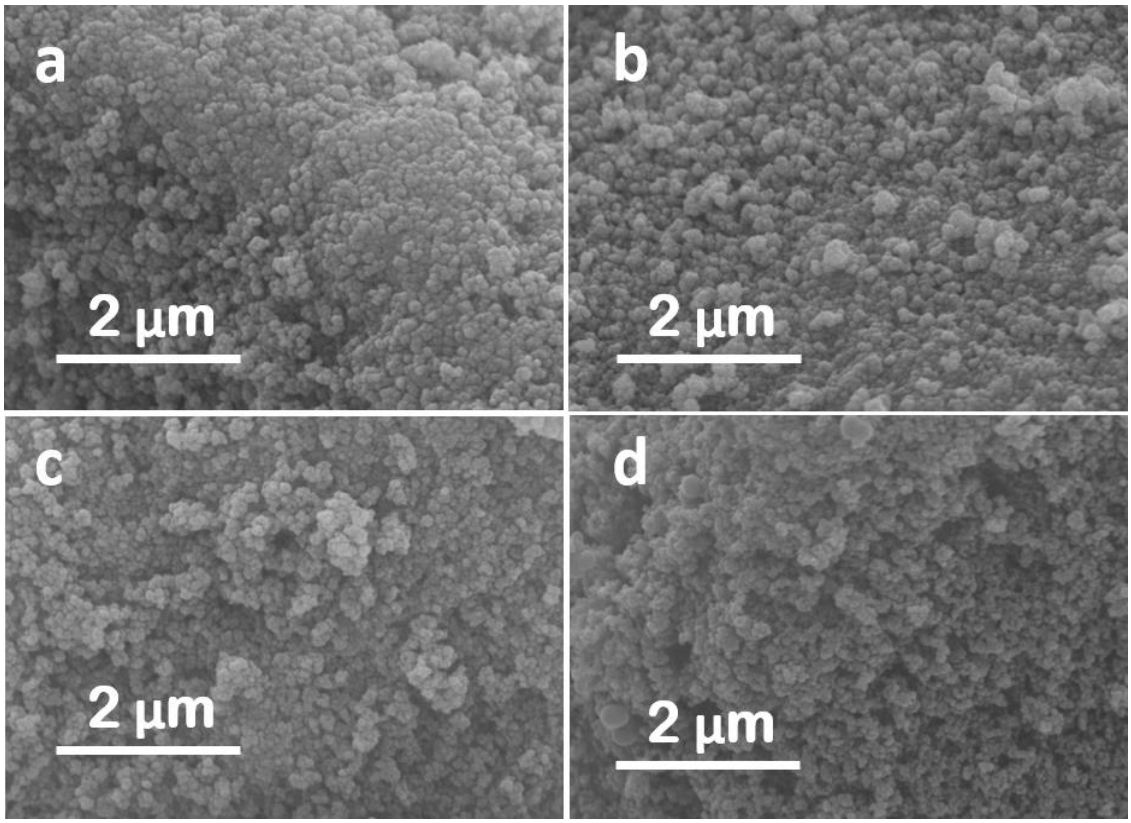

Fig. 4.11 Representative SEM images of selected NPs: (a) ZnO and (b) ZnO@C; (c) TiO_2 and (d) TiO_2@C.

TEM

Based on the TEM images in Fig. 4.12, the detailed structure and morphology features of individual MO_X@C NPs were further investigated and the resulting images are shown below. In Fig. 4.12a, the ZnO@C NPs exhibit an average particle size of *c.a.* 30-50 nm, with a bright carbon shell homogenously covering the dark ZnO core. The zoomed image of the selected area shows that the thickness of the coating is less than 2 nm, in which the lattice fringe is approximately 0.34 nm, corresponding to the (002) graphitic carbon.[70] This observed very thin coating is consistent with the weak (002) XRD peak intensity mentioned above. The EDS line scan clearly demonstrates that the C-coating is smoothly sheathed the entire particle surface. In particular, the almost constant C intensity signals while measured crossing the particle confirm that the coating has a uniform thickness. The TiO_2@C NPs exhibit similar morphology and structures to the ZnO@C NPs, as shown in Fig. 4.12b.

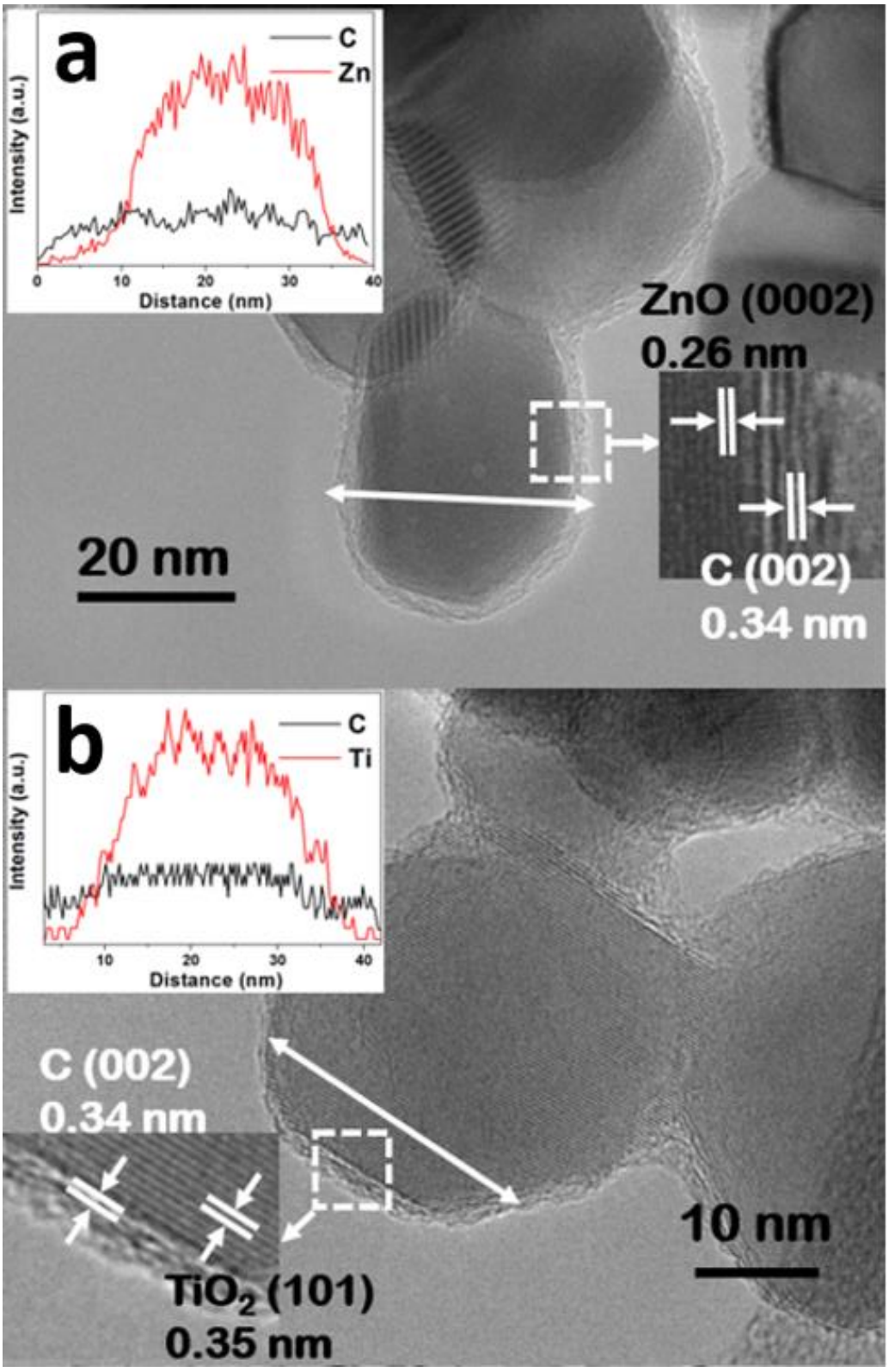

Fig. 4.12 TEM images of (a) ZnO@C and (b) TiO_2@C NPs. The insets are the corresponding EDS-line scan patterns

TGA

The TGA profiles of various MO_X@C NPs is shown in Fig. 4.13. The ZnO@C NPs show the highest starting degradation temperature point (T_S), which is selected by the slope of the tangent of the weight loss curve became negative, at 463 ^oC, whilst the CeO_2@C NPs have the lowest T_S at 361 ^oC, and the other NPs are around 390-400 ^oC. The ending degradation temperatures point (T_E) is chosen by the slope of the tangent of the weight loss curve back to zero again. For these MO_X@C NPs are between 550-570 ^oC, except CeO_2@C NPs which is at 500 ^oC. Therefore, the slopes of weight loss are quite complex, associated with the onset T_S. These profiles show different starting and ending degradation temperatures, and different degradation speeds, which are reflection of the graphitisation levels, as highly graphitised carbon will be oxidised slowly at higher temperature. The degradation is due to the oxidation or burning of the outer carbon shell into CO_2. These weight loss characteristics are comparable to or even better than many other forms of nanostructured carbon materials, such as graphene and carbon nanotubes, hence the coating layers demonstrate the high quality of graphitic feature.

From the Raman spectra, the ZrO_2@C NPs have relatively better crystallisation with the lowest I_D/I_G (= 0.58) than the other NPs (Raman Spectra in Fig. 4.10). However, their T_E does not appear to be the highest, only sitting in the middle, and is comparable to that of Cr_2O_3@C and TiO_2@C NPs. The quality of the C-coating is not only associated with the crystallization level, but also influenced by other properties of the core material. Such as ZnO@C NPs, although its XRD profile shows the broadest (002) peak and its Raman spectrum has a higher I_D/I_G value (=0.96), both results suggesting relatively poorer crystallised coating than others, but it exhibits the highest T_E.

The carbon interface bonding property of the MO_X@C NPs are different from each other, which could affect both the T_S and T_E. In other words, the carbon coating is not only the physical deposit process, but also contains the chemical bonding. We believe that the different thermal stabilities among these coated NPs could be associated with the metal oxide core, which has different surface chemical property and crystalline structures.

i.e. the coating would have a higher graphitization leave and stronger adhesion property with the core, resulting in high T_E. In the case of ZnO NPs, it has a lattice constant of 0.325 nm, which matches very well with the 0.34 nm layer spacing observed in the coating, which promotes the coating growth and the formation of a strong adhesion to the ZnO core. Therefore, the ZnO@C NPs exhibit the highest T_E.

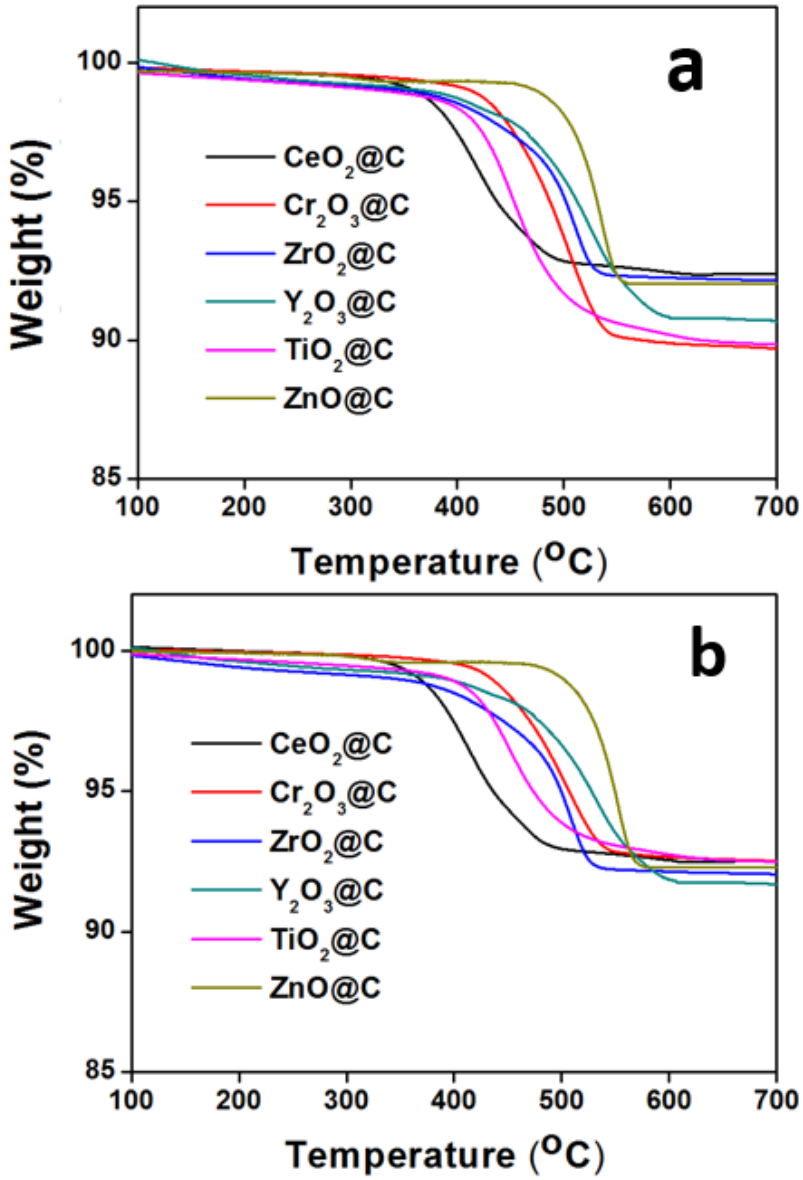

Fig. 4.13 (a) The original and (b) axis normalised TGA curves of different MO_X@C NP specimens.

To contrast the coating amounts against different metal oxides is quite complicated, because the NPs have different densities (*i.e.* different numbers of NPs for 10 mg samples used for TGA), therefore the percentage of weight loss does not necessarily to be a direct reflection of the carbon weigh loss for one particle. By assuming a uniform particle size and particle stacking density, we can approximately normalise the percentage of the weight loss shown in Fig. 4.13a, and have obtained Fig. 4.13b for different MO_X@C specimens by using the ZnO NPs as a standard. The normalised results have shown that the residual weights for all MO_X@C NPs are *ca*. 92%. Therefore, the C-coating on different NPs is nearly constant. This analysis offers further evidence that the RCVD process can precisely control the carbon coating thickness, to produce MO_X@C NPs at large scale.

4.4 Conclusion

In this Chapter, the details of modification of Xu's furnace were described. We have also systematic investigated the potential impact factors for the C-coating, such as graphitisation level vs temperature, carbon coating thickness vs reaction time, coating thickness vs injection rate, graphitized carbon membrane, and the electrical property of typical carbon coating metal oxide--TiO_2@C. The structures of the MO_X@C NPs were analysed by XRD, Raman, TEM, EDS, SEM and TGA respectively, in the latter part of this Chapter to thoroughly characterise the morphological, structure and thermal properties. Out results have shown that the C-coating composite NPs have formed an entire individual carbon membrane outside the particles, which displayed excellent properties in the thermal stability and additional electrical conductivity. These results also suggest that these new C-coated NPs could be ideal reinforcements for the fabrication of new nanocomposites.

Chapter 5. Fabrication of MO_X@C NPs reinforced nylon 12 nanocomposites

5.1 Introduction

Metal oxides (MO_X) are widely used in composite preparation, due to their super hardness, richness in material and property choices, and chemically stable features. Polymer materials are also widely used in different industrial and domestic sectors. By introducing small metal oxide particles into a polymer matrix, much improved mechanical properties such as tensile strength and hardness, even the thermal properties, can be obtained. The most commonly investigated commercial polymer is nylon-based materials[17, 81-84]. However, one of the toughest challenges for preparing non-magnetic MO_X nanocomposite in nylon is the NPs dispersion issue, where M = Ce, Cr, Zr, Y, Ti and Zn, and X = 1, 1.5 and 2, and their interface behaviour is still not completely understood. These challenges require further investigation. For the objective of this chapter, because of having successfully created various carbon coating NPs, we report a method to fabricate the MOx@C NPs reinforced nanocomposites and demonstrate the properties for the composites.

5.2 Preparation of nylon 12 nanocomposites

ZnO is regarded as the most common and promising material in many application areas, such as in semiconductors, electronics, photonics, piezoelectric and nanocomposite preparation. ZnO-reinforced polymer composites have attracted intensive investigations due to their high performance in chemical industry and their low cost[96, 189]. As a widely used engineering polymer with low cost, nylon 12 has superb capacity of loading reinforcing materials for previous research. Therefore, nylon 12, ZnO and ZnO@C NPs as the typical examples have been chosen as the matrix and reinforcement phases in this study.

As detailed in Chapter 3, an extremely simple and direct fabrication method was used to prepare the ZnO NPs reinforced nylon 12 nanocomposite, as well as the ZnO@C NPs reinforced nylon 12 nanocomposite. After heat treatment at 120 ^{o}C in a temperature-controlled oven for overnight to release the residual

stress, samples of different sizes were cut for further experiments, including tensile test, Vickers hardness test and thermal conductivity property assessment.

5.3 Investigation of nylon 12 nanocomposites

5.3.1 The ZnO NP dispersion

Using ZnO as a typical example to provide an understanding of the key dispersion parameter for future composite fabrication, we studied the dispersion property of the NPs in water based suspensions by using UV-Vis spectroscopy, and the results are shown in Fig. 5.1. The suspensions of ZnO and ZnO@C NPs were prepared with the assistance of 1 wt% of SDS (Sodium Dodecyl Sulfate) surfactant. To evaluate the coating influence on the sediment rate (opposite to dispersion) of these insoluble NPs in water, a higher adsorption is an indicator of thicker suspension correlating to a uniform dispersion, whereas a lower adsorption indicates a clearer suspension which means a rapid sediment as a result of agglomeration. A strong ZnO UV-Vis peak at 325 nm was chosen as a standard peak in this study, and the peak ratio when samples were kept stationary for several time was then compared with the original standard adsorption peak. At the beginning, both samples show comparable adsorption. After 1 h, the absorbance intensity of the ZnO@C NPs remained as high as 98%, whilst the plain ZnO only maintained 42% of its original intensity. After 24 h, the plain ZnO NPs were completely dropped to the bottom of the container and there was hardly any adsorption observed in the spectrum; however the ZnO@C NPs suspension remained over 85% of its original intensity. This result has clearly demonstrated that the surface modified C-coated NPs have significantly improved their dispersal ability with suitable surfactant. The C-coating on the NPs has offered important potentials for eliminating the agglomeration issues associated with NPs, with a similarly modifiable behaviour to those of the well-documented carbon nanotubes, so that mature surface modification strategies are readily available for achieving strong interface bonding and good dispersions. This excellent surface tuneable feature of the C-

coating offered by the RCVD process could open new opportunities for the fabrication of nanocomposites.

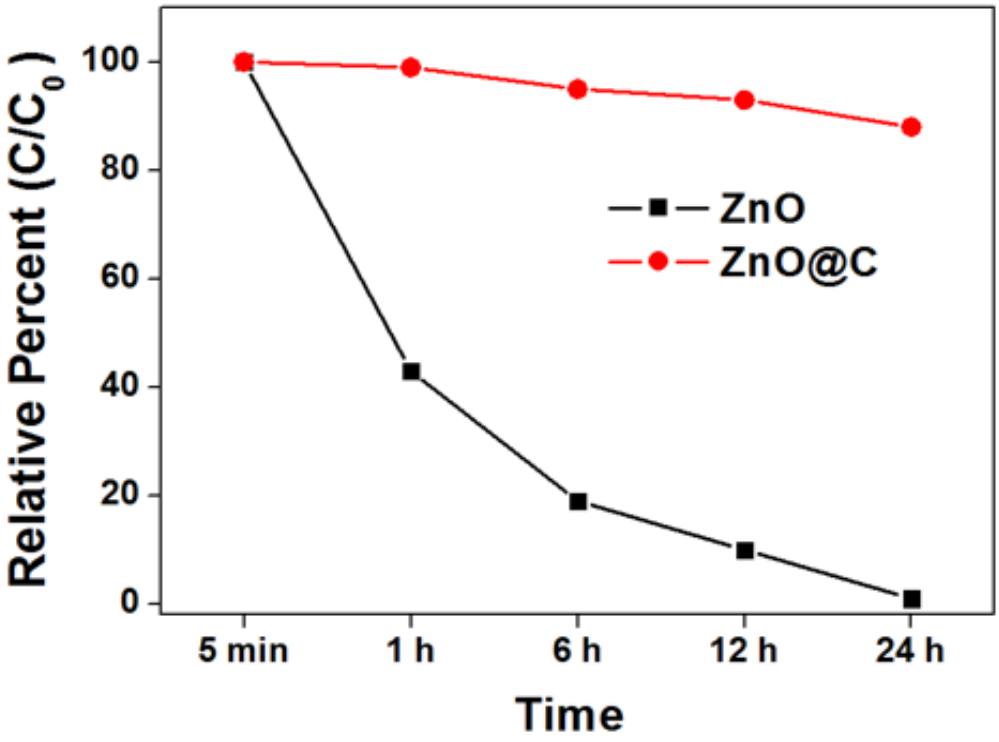

Fig. 5.1 A comparison of the intensity of the UV-Vis absorbance spectra between plain ZnO and ZnO@C NPs.

5.3.2 Tensile strength

To further validate the improved dispersal behaviour towards potential composite fabrication, we embed the ZnO NPs into nylon 12, in an effort to ascertain any advantages in the thermal and mechanical properties for the C-coated NPs over the naked NPs. By using the simple water/ethanol solvent direct mixing method, we fabricated the ZnO@C NPs-reinforced nylon 12 model composites, in comparison to the plain ZnO NPs-reinforced samples. We focused our investigation mainly on the evaluation of the key mechanical properties of the composites, to validate the role of the C-coating in the composites.

Further validation was achieved in the tensile strength between the ZnO-nylon 12 and ZnO@C-nylon 12 nanocomposites at a filler content from 1 to 4 wt%, and the results are presented in Fig. 5.2a. Compared with the plain nylon 12 sample, the ultimate tensile strength of both the 2 wt% composites was increased to 54.5 MPa and 59.6 MPa, which corresponds to an improvement of 16% and 27% for ZnO and ZnO@C, respectively. By modifying the surface chemistry of the ZnO with the carbon coating, it can not only affect the NPs dispersability in water during the powder mixing stage and finally in the composites, but also the carbon layer can improve the interface adhesion with the nylon 12 matrix. At 4 wt% however, the ZnO@C-nylon 12 sample exhibits lower ultimate tensile strength than the ZnO sample. It is well-documented that the enhancing effect of spherical NPs is not that obvious, therefore the 27% improvement at an optimal addition of 2 wt% of ZnO@C NPs is very impressive.

However, in Fig. 5.2b, the elongation rate for ZnO@C-nylon 12 nanocomposite shows the worse property than ZnO-nylon 12. When the content is 1 wt%, the elongation for the ZnO displays the 5% improvement, rather than the ZnO@C become 6% worse. Till the content reached 4 wt%, the difference between those two samples become minimum.

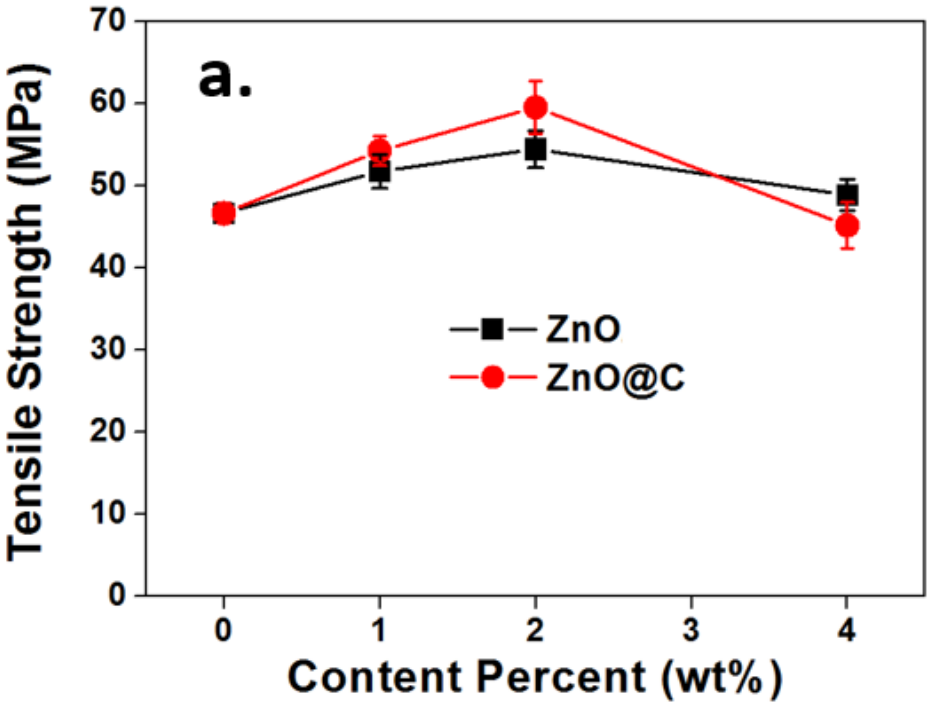

a. Ultimate tensile strength

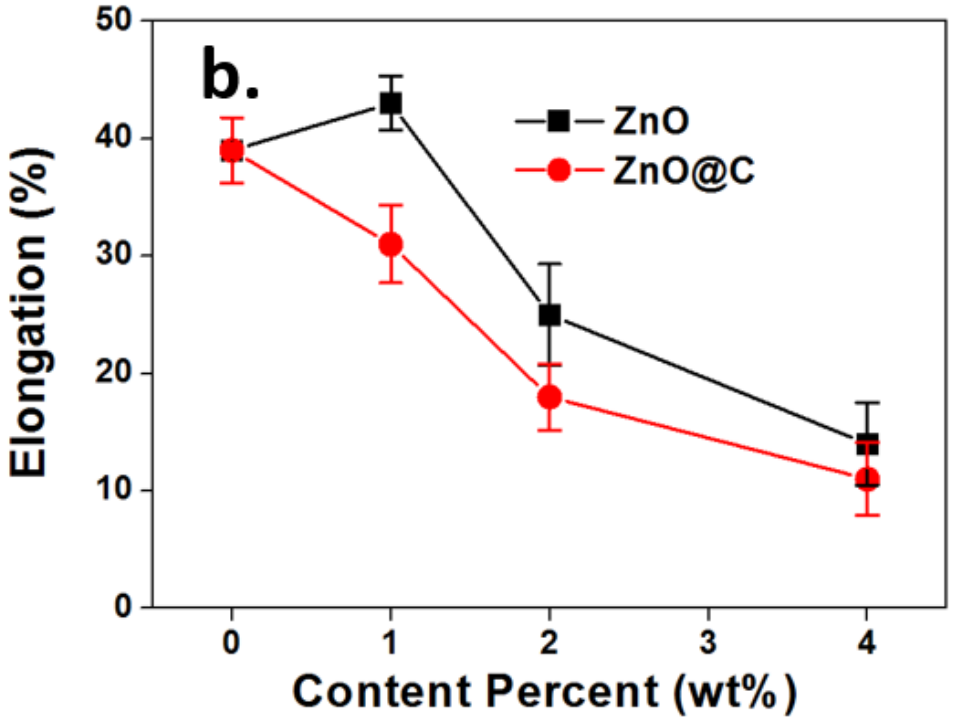

b. Elongation percentages

Fig. 5.2 Mechanical properties of the ZnO-nylon 12 and ZnO@C-nylon 12 nanocomposites with different filler contents

5.3.3 Vickers hardness testing

As shown in Fig. 5.3, the hardness values (HV) of the composites were all much higher than that of plain nylon 12. The highest HV values were obtained from the 4 wt% ZnO-nylon 12 and ZnO@C-nylon 12 samples, being 16.8 and 19.1 $HV_{0.5}$, respectively. The improvement of the ZnO@C-nylon 12 is around 28%, which is against the plain nylon 12 (14.9 $HV_{0.5}$) and the ZnO-nylon 12 is only 12% improvment. Furthermore, the increased tendency of the hardness values indicated that the embedded NPs can improve the toughness of the composite. Increasing the filler amounts, the C-coated samples showed more improvements in the hardness, which means the carbon-coated ZnO NPs exhibiting a greater improvement effect than that of the pristine ZnO NPs, which shows the extra improvement with16% at 4 wt%.

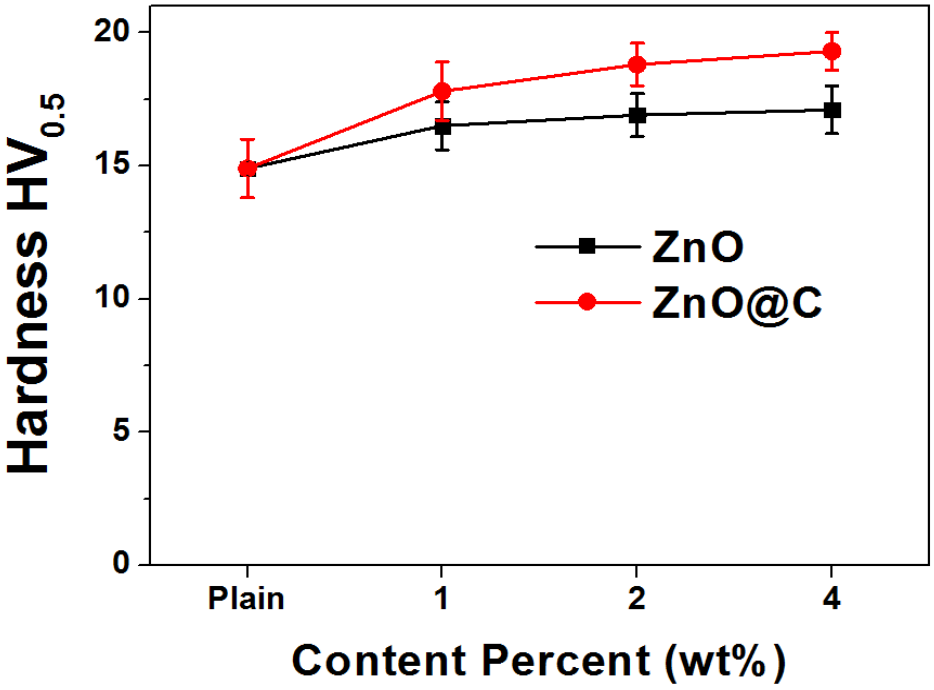

Fig. 5.3 Vickers hardness values of the ZnO-nylon 12 and ZnO@C-nylon 12 nanocomposites at different filler contents

5.3.4 Thermal conductivity

The corresponding thermal conductivities of both composites, ZnO@C-nylon 12 and ZnO-nylon 12, are shown in Fig. 5.4. At 25 ^{o}C, the thermal conductivity of the neat nylon 12 is only 0.205 $W \cdot m^{-1} \cdot K^{-1}$, which sets the standard for comparison with the two nanocomposites. With the NP addition, the thermal conductivities have been improved for both composites, as shown in Fig. 5.4a, however by different enhancing effects at different amounts of NPs. These values increase gradually with increased NP contents, but the plain ZnO NPs-reinforced composites only show a marginal improvement than at lower contents, whilst the ZnO@C NPs-reinforced composites exhibit a linear enhancement feature.

As shown in Fig. 5.4b, the thermal conductivity of the ZnO@C NPs-reinforced samples is enhanced by 22, 35 and 49% (reaching an absolute value of 0.305 $W \cdot m^{-1} \cdot K^{-1}$) for the 1, 2 and 4 wt%, respectively. At 4 wt% addition, the improvement of the ZnO@C -nylon 12 composite is almost 3 times higher than

that of the neat ZnO-nylon 12. This result directly demonstrates the positive role of the C-coating in improving the thermal properties of a polymeric composite.

It is noteworthy that the level of enhancement reported here for the ZnO@C NPs is of significance, because the 50% improvement at 4 wt% of the core-shell NPs (where the core ZnO is much heavier than carbon) is virtually comparable to the effect of graphene as a filler to reinforce nylon composite. Graphene has been reported to possess the best thermal conductivities (2000–4000 $W \cdot m^{-1} \cdot K^{-1}$) [190, 191]. Therefore, the small amount of effective carbon in the NPs has generated a huge improvement, which indicates its high efficiency. This high efficiency is most likely originated from the improved dispersion and interface bonding of the ZnO@C NPs within the nylon 12 matrix.

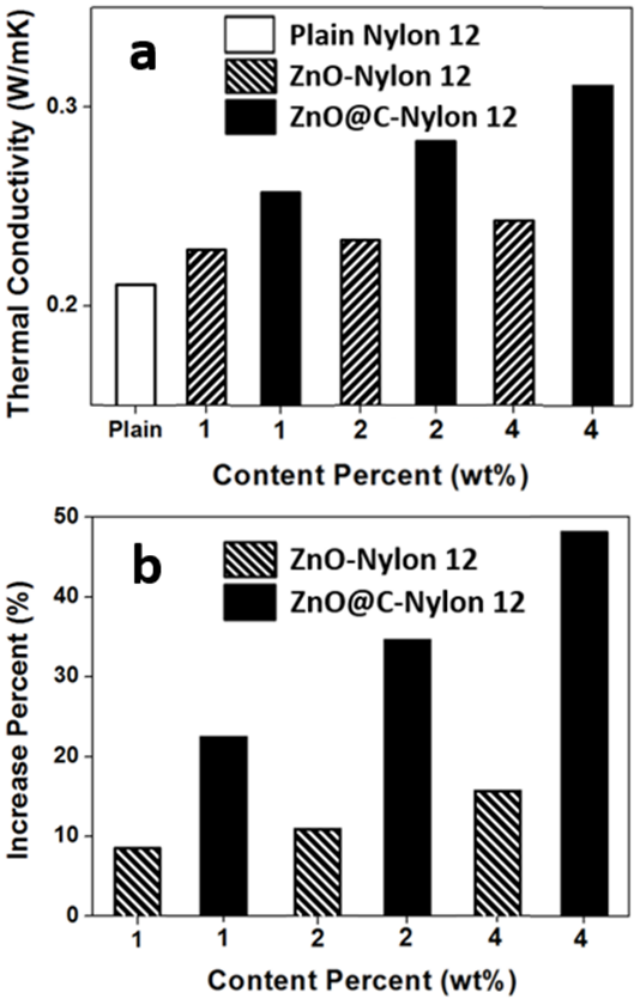

Fig. 5.4 a. Thermal conductivity, and b. The improvement (%) of ZnO-nylon 12 and ZnO@C-nylon 12 nanocomposites measured at 25 ^{o}C.

5.4 Conclusion

In summary, we have established a simple and direct method to fabricate polymer matrix nanocomposite and demonstrated the great advantages of the C-coating in improving the mechanical and thermal properties over plain ZnO NPs in the preparation of polymer composite. Using nylon 12 as the example matrix, we have investigated the typical ZnO and ZnO@C NPs as example fillers, and have shown that the C-coating effectively improves the thermal conductivity by 49%, from 0.205 $W \cdot m^{-1} \cdot K^{-1}$ for neat nylon 12 to 0.305 $W \cdot m^{-1} \cdot K^{-1}$ for a 4 wt% C-coated ZnO composite. We have further reported a 27% improvement in tensile strength at a small amount of ZnO@C filler addition and 28% improvement in hardness for the composites. These results have demonstrated the potential of the C-coated NPs in applications to enhance other polymer in composites, which will be discussed in later chapters.

Chapter 6 Fabrication of IF-WS_2 NPs and its PEEK nanocomposites

6.1 Introduction

Poly(ether ether ketone) (PEEK), a member of the Poly(aryl ether ketone) (PAEK) family, is an promising high performance engineering thermoplastic with melting temperatures around 343 °C and glass transition temperatures around 140~160 °C[162, 192]. PEEK has shown many outstanding properties such as excellent mechanical strength (tensile strength ~141 MPa), high chemical resistance to acid and alkali corrosion, low thermal conductivity (0.23 W/m·K) which could be used as an outstanding thermal insulator with good thermal stability, and especially extraordinary biocompatibility that made it suitable for medical applications in implanting of tooth and prosthesis[154, 190]. PEEK therefore has attracted huge research interest to exploit applications in areas including aircraft, automotive, fuel cell energy, and medical implants. New members of the PEEK family with specific features have been developed to suit for a broad range of applications, in terms of properties, processability and price. As one of the few high performance thermoplastic materials currently available commercially, the PEEK family are becoming more and more important for these industry sectors[155, 193]. However, some features of the PEEK could be improved, for example the intrinsically low thermal conductivity of the PEEK could limit its applications in certain components. To further enhance these performance, PEEK and its derivatives could be reinforced using advanced fillers, to meet the even critical demands for future applications[164, 194].

The inorganic fullerene-like tungsten disulphide (IF-WS_2) NPs, as the first successfully commercialised synthetic nanomaterials shortly after its discovery by Tenne *et al.*, presented the extremely good tribological properties either directly as solid lubricant or indirectly as additives in oil, and superb shock absorbing behaviour, which makes them an ideal reinforcement filler for different polymer matrices to improve the thermal, mechanical, and tribological properties of polymers[24, 194].

However, to achieve a uniform dispersion of the nanofillers within the polymer matrix is always a huge challenge due to their tendency of agglomeration originating from the Van der Waals attractions, and this is particularly true for certain fabrication processes. This explains why early studies only reported composites with IF-WS_2 NPs incorporation merely up to *ca*. 2 wt%[194]. Therefore, the continuous development of new techniques for the creation of PEEK/IF-WS_2 nanocomposites with uniform IF-WS_2 dispersion is an interesting research subject. This Chapter describes a simple and eco-friendly melting process for the fabrication of such PEEK/IF-WS_2 nanocomposites, by using a mixture of water and ethanol to disperse the IF-WS_2 and PEEK powder prior to the melt shaping process. The influence of a wide range of IF-WS_2 fillers on the properties of the resulting PEEK nanocomposites will also be investigated.

6.2 Cooling process influence for plain PEEK

For PEEK polymer materials, the aggregation of molecular chains during the crystallization process from loose powder to bulk sample always causes the shrinkage in volume, which decreases the specific volume and increases the density. In general, there is a linear relationship between the density and crystallinity for a polymer. As the density increases, the attractive force between the molecular chains increases, thus the mechanical and thermal properties of polymer are improved by increasing the crystallinity[154, 190, 193].

Normally, as the degree of crystallinity increases, the tensile strength, Young's modulus and hardness of the polymer all increase, however the brittleness of the polymer will also increase at the same time. As a result, external impact can be easily progressed along the crystal surface and cause fractural damage. Therefore, the impact resistance of a polymer could decrease with the increase of crystallinity. Different factors can affect the crystallization process of a polymer, such as the cooling rate, melting temperature, melting time and applied stress, *etc,* of which the most importance one is the sample cooling rate[157].

In this chapter, we attempted to discuss the influence of the cooling rate on the crystallinity and on the mechanical properties of the PEEK, by measuring the

time interval from the heating treatment temperature 380°C down to 140°C which is lower than the glass transition temperature around 143°C. The PEEK powder is melted on a small glass slide first and then transferred the slide onto the external cooling substrate. By using a portable infrared temperature monitor, the temperature changes of the sample surface are recorded. Because of different cooling substrate having different thermal conductivity, the different cooling rate will influence the polymer structure forming process. This difference will change the morphology of the polymer and further change its mechanical properties.

6.2.1 Different cooling processing and cooling rate control

As shown in the Fig. 6.1, the PEEK cooling on the surface of an asbestos block displayed the longest cooling time interval and the Al substrate resulted in the shortest cooling time. Those results are reasonable because the thermal conductivity of Al metal is much higher than all the other kind of substrates. In addition, the asbestos and wool bases showed almost the same influence on the final PEEK thin films, and rock stone only exhibited just a few seconds faster than the asbestos. It is believed that the too fast cooling rate would lead to a poor crystallinity in the PEEK, which will be verified later.

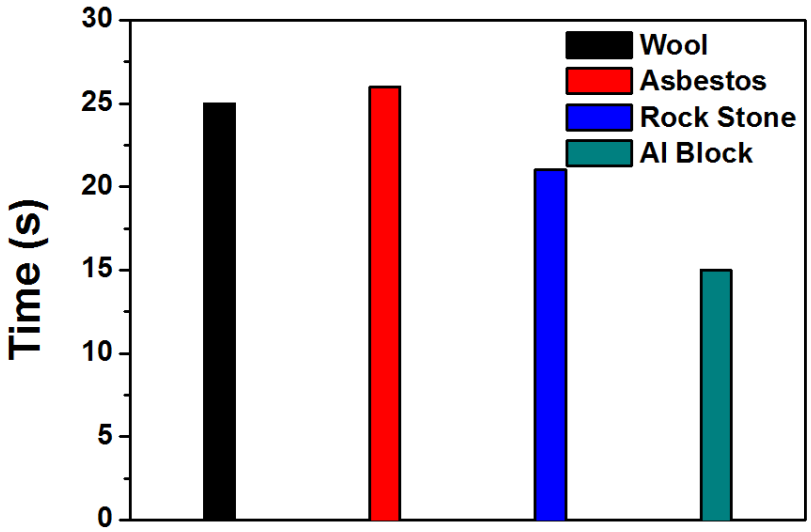

Fig. 6.1 The neat PEEK cooling time from 380 to 140°C when sitting on the surface of different substrates.

6.2.2 Morphology characterization and crystallization analysis

According to the SEM images shown in Fig. 6.2, the samples cooling on wool (Fig. 6.2a) and asbestos (Fig. 6.2b) exhibited similar morphology with a smooth surface. However, when the cooling rate increased on a rock stone surface, the morphology of the sample displayed wrinkled patterns with random directions (Fig. 6.2c), which could be caused by unbalanced cooling, and the crystals formed along the fastest cooling points on the edge on the mould. The sample cooled on Al showed a clear individually cracked pattern, Fig. 6.2d. It is believed that the fastest cooling process failed to allow the polymer to crystallise smoothly which caused the formation of small random gaps on the surface of the sample[195].

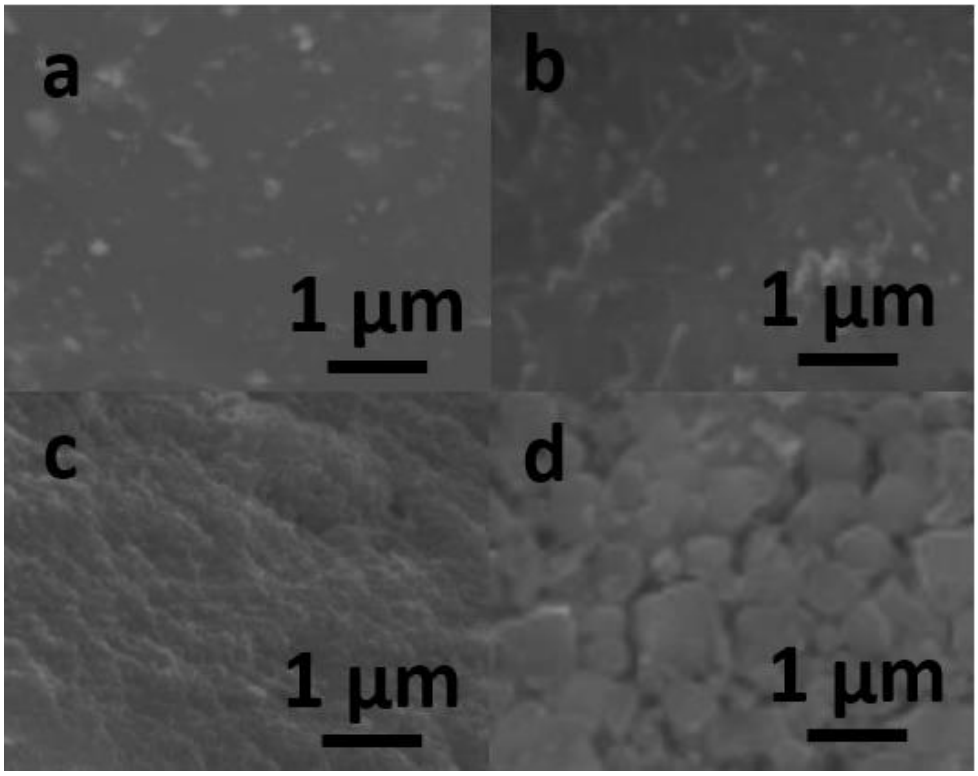

Fig. 6.2 SEM images of the plain bulk PEEK samples prepared on different external cooling substrate's surface. a) Wool; b) Asbestos; c) Rock Stone; and d) Aluminium Block.

6.2.3 Mechanical tensile testing

In Fig. 6.3, the results of the ultimate tensile strength demonstrated that the PEEK cooled on the asbestos substrate had the best tensile strength of 81.8 MPa, followed by the wool cooling sample of 79.1 MPa. Even the morphology with the wrinkled patterns, the rock stone cooled sample still showed a strength value of 76.8 MPa, which is just approximately 6% lower than that of cooled on asbestos. The sample cooled on the Al substrate exhibited the lowest tensile strength of only 69.3 MPa. The reason can be because of the incomplete crystalline structure forming inside the polymer matrix. The individual cracked structure cannot show the proper mechanical stability and display the worst value among the 4 different cooling substrates.

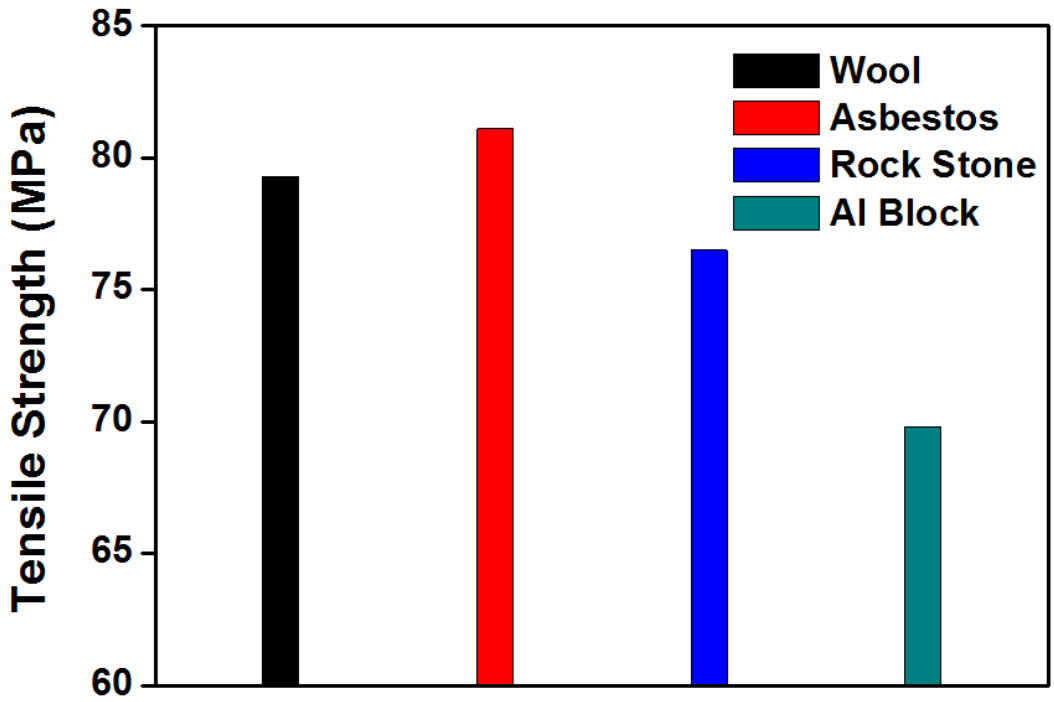

Fig. 6.3 The ultimate tensile strength of PEEK on different substance surfaces

6.3 Synthesis of IF-WS_2 NPs and their reinforced PEEK nanocomposites

The synthesis process of IF-WS_2 NPs has been detailed in Chapter 3, following the modified Xu's rotary furnace technique. The precursor powders were prepared by the simple and direct solution mixing method, prior to melting for composite fabrication.

After the mixing and drying process, the mixed composite powders were transferred onto a glass slide substrate of 380 to 400^{o}C sitting on a hot plate. After a few mins, the powders were melted completely to form a thin film, and the glass slide substrate was then removed from the hot plate onto an asbestos substrate and allowed to cool naturally. The resulting composite films could be easily peeled off from the glass, for subsequent testing.

6.4 Characterisation of IF-WS_2/PEEK nanocomposites

6.4.1 Morphology (SEM, TEM and AFM)

SEM

The SEM images in Fig. 6.4. show the spherulitic crystal structure of the PEEK-based samples. The plain PEEK, Fig. 6.4a and b, exhibits granular structures comprised clearly radial spherulites, respectively. Each lamellar particle is spreading along the radiation direction, stacking together forming radial arrays, which is a typical feature of self-assembly. For the composite samples shown in Fig. 6.4c, the IF-WS_2 particles are found to be embedded inside the spherultic structure, and a slightly different morphology against the neat PEEK is observed. Although the composite samples show nearly the same basic granular size of *ca.* 0.1 μm, their spherulite sizes become smaller compared with the neat sample, reduced from around 10 μm to about 3 μm when the IF-WS_2 was added to the matrix. Furthermore, compared with the plain PEEK, a more random distribution of the lamellar is recognised in the PEEK/IF-WS_2 composite. The incomplete small radial spherulites in the matrix have indicated that the size and direction of the spherulites are changed, as a result of the IF-WS_2 incorporation. This would have an influence on the composite properties, however there are no obvious statistic links between the IF-WS_2 content and the spherulite size. The IF-WS_2 particles existing as bright spots are confirmed by EDS analyses, as shown in Fig. 6.4d, which exhibits the obvious peaks of W and S (Au is from the thin coating)[162, 192].

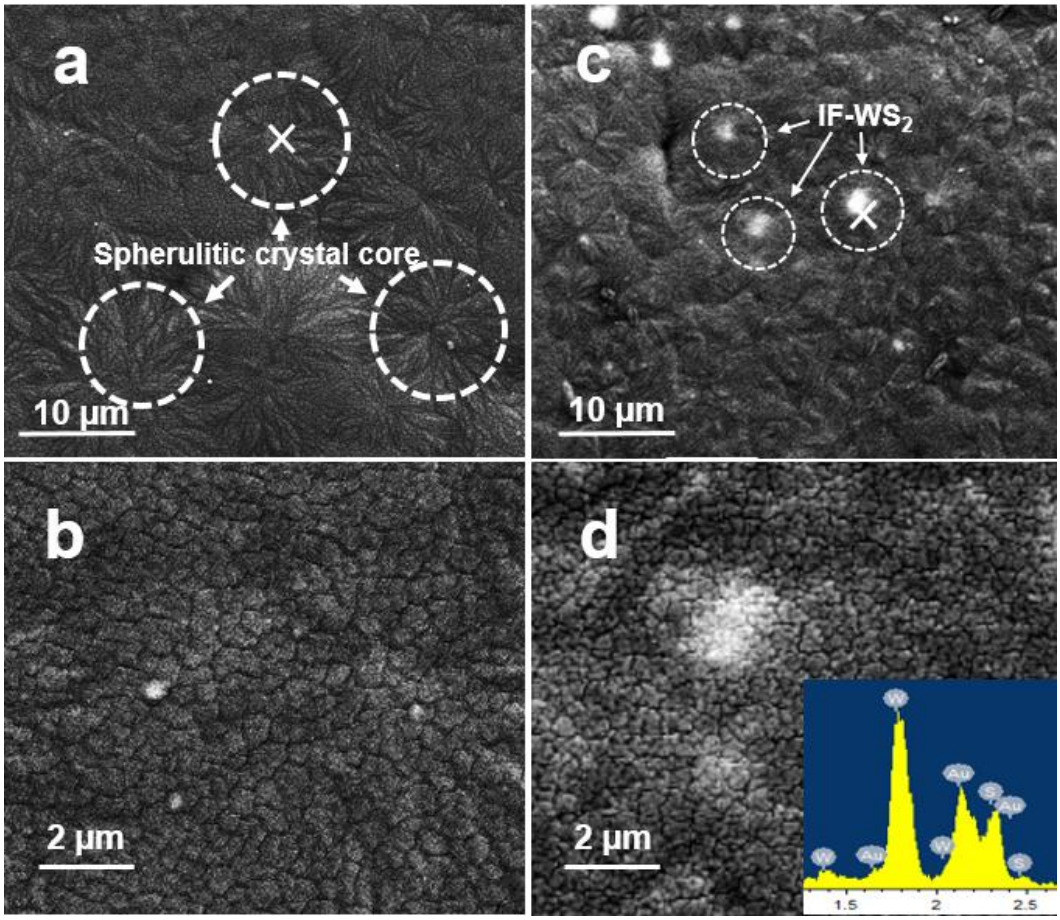

Fig. 6.4 SEM images of the PEEK and PEEK/IF-WS_2 composite samples. (a) The spherulitic crystallines of the neat PEEK (dashes circled), revealing the centre of the spherulites (marked by a cross); (b) The granular of the spherulitic structure at higher magnification; (c) Composite with 4 wt% IF-WS_2 addition, showing the IF-WS_2 particles randomly distributed within the spherulitic structure; and (d) An area containing the IF-WS_2, as confirmed by the EDS result, inset.

TEM

The polygonal structural feature of the pristine IF-WS_2 NPs is displayed in the TEM images in Fig. 6.5a and b[138, 196]. To avoid structural damage to the polymer caused by electron beams, a 100-kV acceleration voltage was used for imaging. In the TEM images, the granular structure of the PEEK is not distinguishable because of the high contrast, however the spherulitic structures are still recognisable[193]. Compared with the polymer matrix, the IF-WS_2 particles are clearly seen as dark phases, appearing as a cluster of small

agglomerations, as shown in Fig. 6.5c, because of the good penetrability of polymer material by the high-velocity electrons. In Fig. 6.5c, these IF-WS_2 NPs are obviously seen with stacked spots in the middle of the spherulites of the PEEK matrix, and the agglomerate indeed acts as a core to promote the formation of spherulites (Fig. 6.5d). Apart from the side of the IF-WS_2 arrays, there are lots of tiny dark spots with diameters around 2 to 10 nm, which indicate a higher density of IF-WS_2 NPs in these areas.

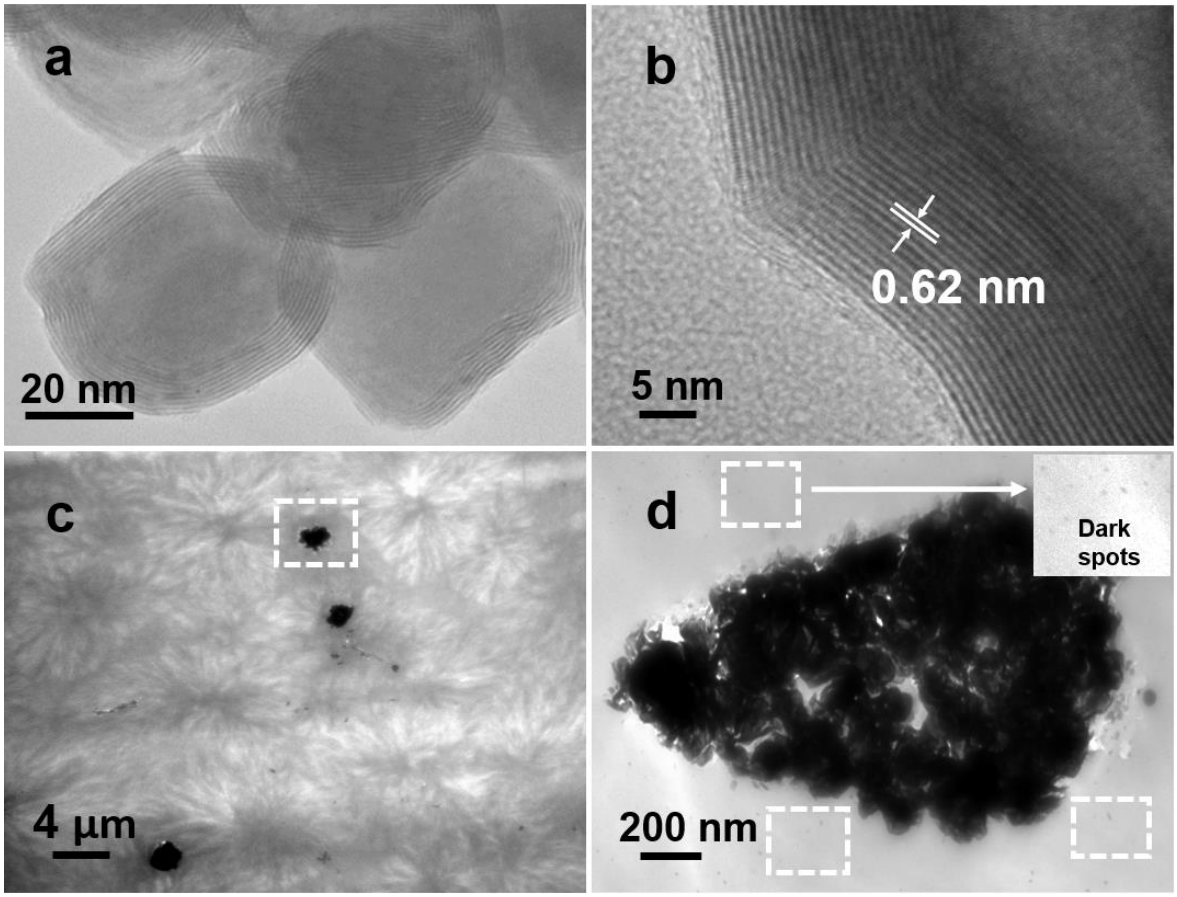

Fig. 6.5. TEM images of the pristine IF-WS_2 NPs (a, b), and the 4 wt% IF-WS_2 NPs in the PEEK matrix (c, d).

AFM

To evaluate the thickness difference between the granular crystal and the polymer matrix, the surface morphology of the composites was inspected by AFM. In Fig. 6.6a, a large layer of IF-WS_2 particles is lying on the surface of a

spherulitic crystal (according to the red line in Fig. 6.6b), which is about 75 nm above the base surface, thus matching the size of a single IF-WS_2 NP. In addition, the regions marked by the blue and green lines in Fig. 6.6a show that the IF-WS_2 NPs are partly embedded inside the PEEK matrix, because the regular lamellar structure only displays pulsed height signals of 1 to 3 nm fluctuations, even for the green line, as shown in Fig. 6.6b. The overall distribution of the IF-WS_2 NPs in the matrix appears to be quite uniform according to the AFM study, which is in consistent with the SEM results.

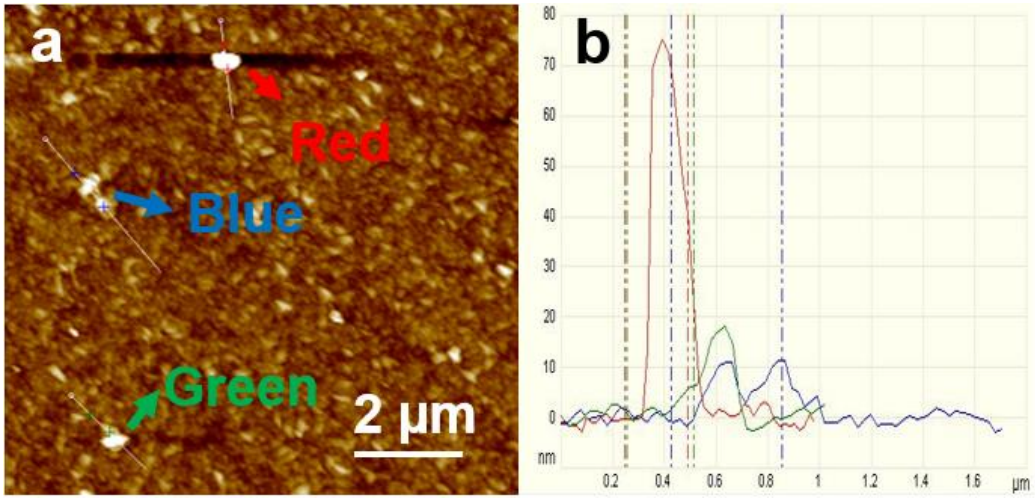

Fig. 6.6 (a) AFM image taken from the PEEK-/IF-WS_2 4 wt% composite, showing the surface morphology of the large granular crystal structures and small IF-WS_2 particles (bright spots). (b) The corresponding surface profile from the marked dotted lines in (a), showing the height differences of the IF-WS_2 cores.

6.4.2 Structure Characterisation (XRD, FTIR and XPS)

XRD

As shown in the XRD results in Fig. 6.7, relatively sharp peaks of the PEEK are observed for the crystallised samples. The (002) peak of the IF-WS_2 NPs is observed in the composites, and the intensities increase with their concentration. In both the neat and composite powder samples prior to melting (Fig. 6.7a), only broad peaks are visible, whilst they become sharper after the melting (Fig. 6.7b), and especially that the 3 peaks at 20.85, 22.83 and 28.88 of 2θ angles,

corresponding to (110), (113) and (200), are prominent[162, 197]. Further, with the increases of IF-WS_2 content, these peaks became narrower and narrower. Considering the full width at half maximum (FWHM) of (110), we believe that the original PEEK powder before melting treatment contained many fine primary crystal cores which led to the broad peaks. After forming polymer and subjecting to natural cooling process, the polymer was better crystallised and subjected to grain growth, resulting in the three obvious peaks. The peaks in the composites however, became even narrower with further reduced FWHM, indicating an even higher degree of crystallisation and larger crystallites than the neat polymer. Hence, the incorporation of IF-WS_2 NPs has demonstrated a mild influence on the crystalline behaviour of the PEEK matrix. It is likely that the incorporation of the IF-WS_2 NPs promoted the nucleation and grain growth for the PEEK polymer during the crystallization process. The IF-WS_2 particles acted as the primary site to induce the crystal core formation during the polymer recrystallization process. The more IF-WS_2 in the matrix, the more promotion effect will be resulted, thus the finer spherulitic grains and broader diffraction peaks. Because of this promotion effect, it is reasonable to deduce that the resulting composite must have simultaneously created a synergetic interface between the PEEK and IF-WS_2 reinforcement, which is essential for high mechanical and thermal performance.

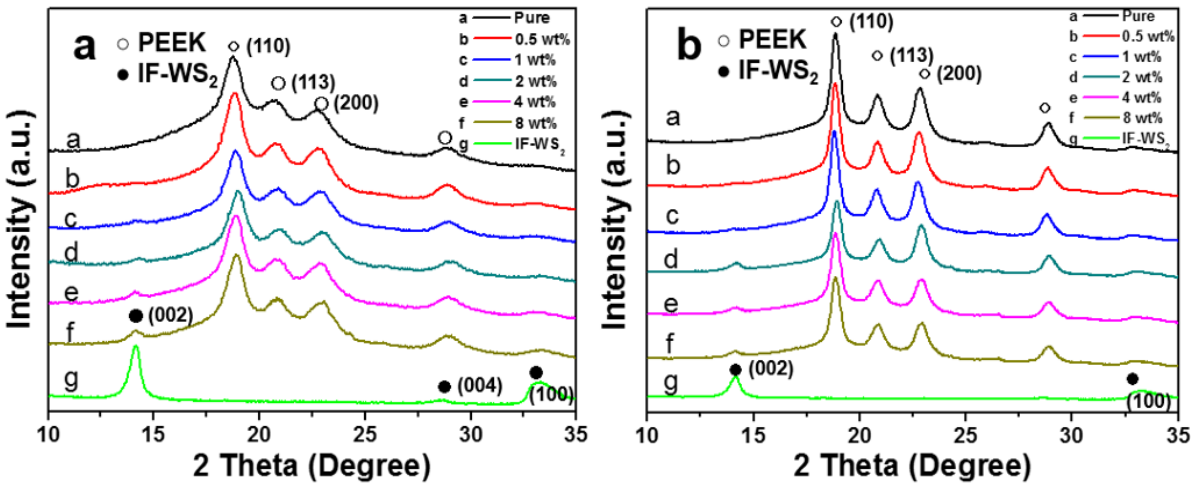

Fig. 6.7 The XRD patterns. (a) Powder mixture of PEEK/IF-WS_2; (b) Crystallised block sample of the PEEK/IF-WS_2 nanocomposite.

FTIR

Because of the lack of relevant literature, the interface of the PEEK/IF-WS_2 deserves further investigations for better understanding the principle of forming the composite. FTIR measurement was used to evaluate the bond between the PEEK and IF-WS_2, and the results are shown in Fig. 6.8. The FTIR absorbance peaks in Fig. 6.8. from high to low wavenumber are assigned as follows. The first strong peak at 1658 cm^{-1} is corresponding to the C=O stretching vibration of carboxylic acid. The other 3 peaks at 1591 cm^{-1}, 1493 cm^{-1} and 1363 cm^{-1} are originated from the C-H band of in-of-plane bending benzene vibration. The band at 1240 cm^{-1} belongs to the keto group (C=O), and the band at 1157 cm^{-1} corresponds to the ether linkage. The red dashes line pointed out in 1037 cm^{-1} band is interesting, as it is not only displayed in the plain PEEK, but also is associated with the covalent band from the C=S stretching vibration which could occur in the composite[164, 195]. Indeed, all the IF-WS_2 composites are corresponding to a little bit higher intensity of this band, which is supportive of the existence of the C=S stretching vibration in the composites. However, the intensity changes are not strong enough to define the differences between different contents composites and need further investigation in XPS. The rest 3 bands of C–H vibration at 946 cm^{-1}, 840 cm^{-1} and 764 cm^{-1} are assigned to the derived band of out-of-plane bending vibration for benzene.

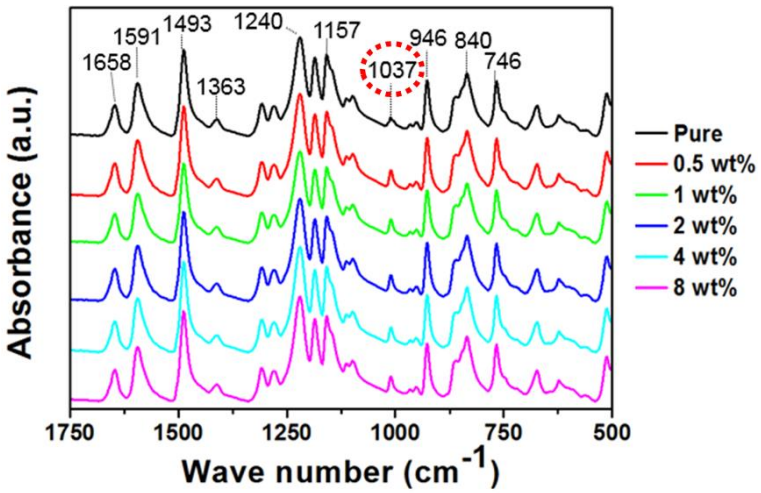

Fig. 6.8 FTIR spectra of the PEEK/IF-WS_2 nanocomposites with different IF-WS_2 contents.

XPS

We used XPS to further investigate the interface of the PEEK/ IF-WS_2, confirming the chemical bonding between PEEK and IF-WS_2 NPs. The XPS analyses were also used to explore the chemical shifting of C 1_S and S 2_P in the PEEK/IF-WS_2 nanocomposites. The result in Fig. 6.4.6a shows binding energy of C 1_S at BE = 284.8, 286.5 and 288.2 eV for the plain PEEK, which corresponds to the C-C, C-O and C=O bond, respectively[198, 199]. The peak locations of the PEEK/IF-WS_2 nanocomposite show similar features, which shows that the introduced IF-WS_2 NPs do not damage the original PEEK matrix indeed. However, the peak intensity reduction of the C=O bond from 3.56% to 2.66% with 0.9% different, by calculated the peak area change, is believed to arise from the formation of new C=S bonding with stronger signal intensity, which replaces the C=O bonding to some extent, as verified in FTIR results as the 1037 cm^{-1} peak change. In addition, the binding energies of S $2_{P1/2}$ and S $2_{P3/2}$ for the pristine IF-WS_2 NPs, as shown in Fig. 6.9b, display two peaks at 165.1 and 163.9 eV respectively[178, 200]. Compared the curves with the PEEK/IF-WS_2 nanocomposite, the S $2_{P1/2}$ line is upshifted about 0.3 eV, which can be ascribed to the charge transfer from IF-WS_2 to the ketone bonding. These chemical bonding linkages would improve the adhesion of the interface with better connections between the NPs and the PEEK matrix, which could benefit the mechanical and physical properties of the nanocomposites.

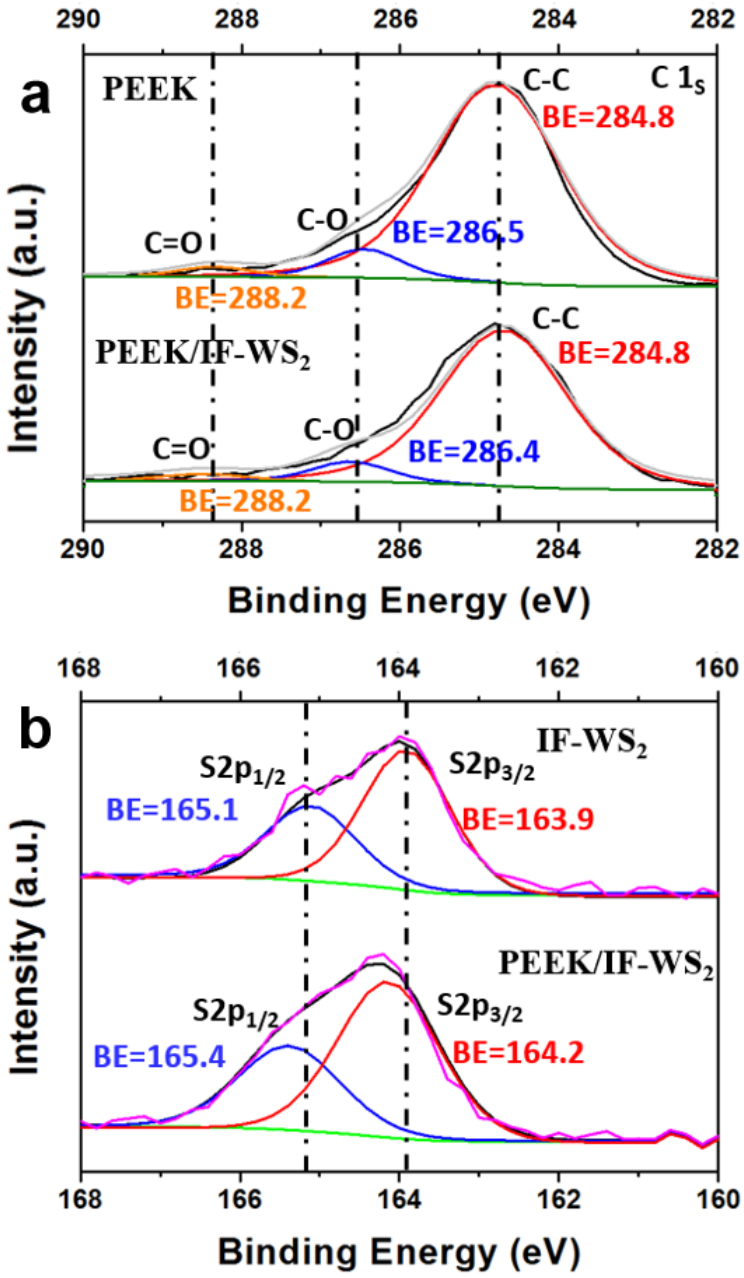

Fig. 6.9 XPS results of plain PEEK sample and 4 wt% PEEK/IF-WS_2 nanocomposite. (a) the $C1_S$ binding energy shows the main structure of the composite is not change because of the peaks position remained. However, the peak intensity slight reduction of the C=O bond is believed to arise from the formation of new C=S bonding with stronger signal intensity, which replaces the C=O bonding to some extent. (b) $S2_P$ lines are upshifted to high level, which can be ascribed to the charge transfer from IF-WS_2 to the ketone bonding.

6.4.3 Thermophysical properties (Thermal Conductivity, Thermal Stability)

Thermal Conductivity

The filler content will affect the thermal conductivity of the IF-WS_2 nanocomposite. The thermal conductivity of the composites was measured from -50 to 300 °C, and the results is shown in Fig. 6.10. At 25°C, the thermal conductivity of the plain PEEK sample was 0.248 $W \cdot m^{-1} \cdot K^{-1}$, which increased progressively for the composites with increased IF-WS_2 contents, from 26, 51, 62, 90 and 190% for the 0.5, 1, 2, 4 and 8 wt% samples, respectively[157, 162]. This result demonstrates that the IF-WS_2 NPs are an effective filler for improving the thermal conductivity of the PEEK matrix. In fact, compared with the PEEK/Graphene (GE) composite, the improvement effect of the IF-WS_2 is surprisingly greater than that of GE to PEEK in which the optimum content of 1 wt% GE led to a 53.7% improvement (0.376 W/m·K), even though GE has been reported to have the best thermal conductivities (2000–4000 W/m·K) [122]. This is most likely down to the uniform dispersion of the IF-WS_2 NPs in the matrix, and the very good interface between the filler and matrix, as validated above by both FTIR and XPS investigations.

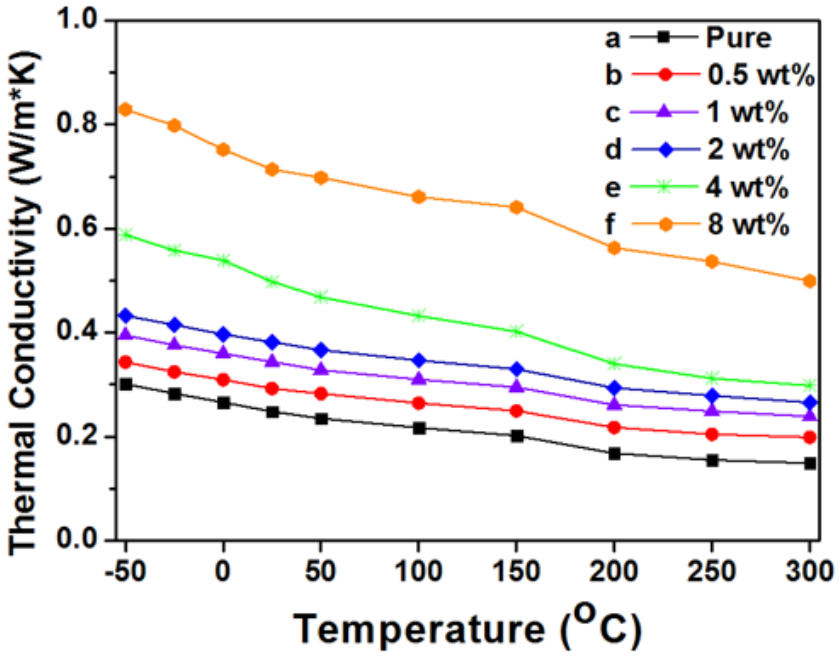

Fig. 6.10 Thermal conductivity of the PEEK/IF-WS_2 nanocomposites against the pure PEEK.

Thermal Stability

The thermal stability results of PEEK/IF-WS_2 samples are presented in Fig. 6.11a, and their corresponding DSC curves are displayed in Fig. 6.11b. These results show that all the samples are degraded over 500 ^oC and, the higher the filler content, the higher the degradation temperature and melting point. For the 8 wt% PEEK/IF-WS_2, it remains nearly 50 wt% of its original weight, rather than 0% as for the plain PEEK sample. The IF-WS_2 contents are burnt under air condition around 580 – 590 ^oC, and the heat release peak shifting to the higher temperature part has demonstrated the better stability and higher burning point.

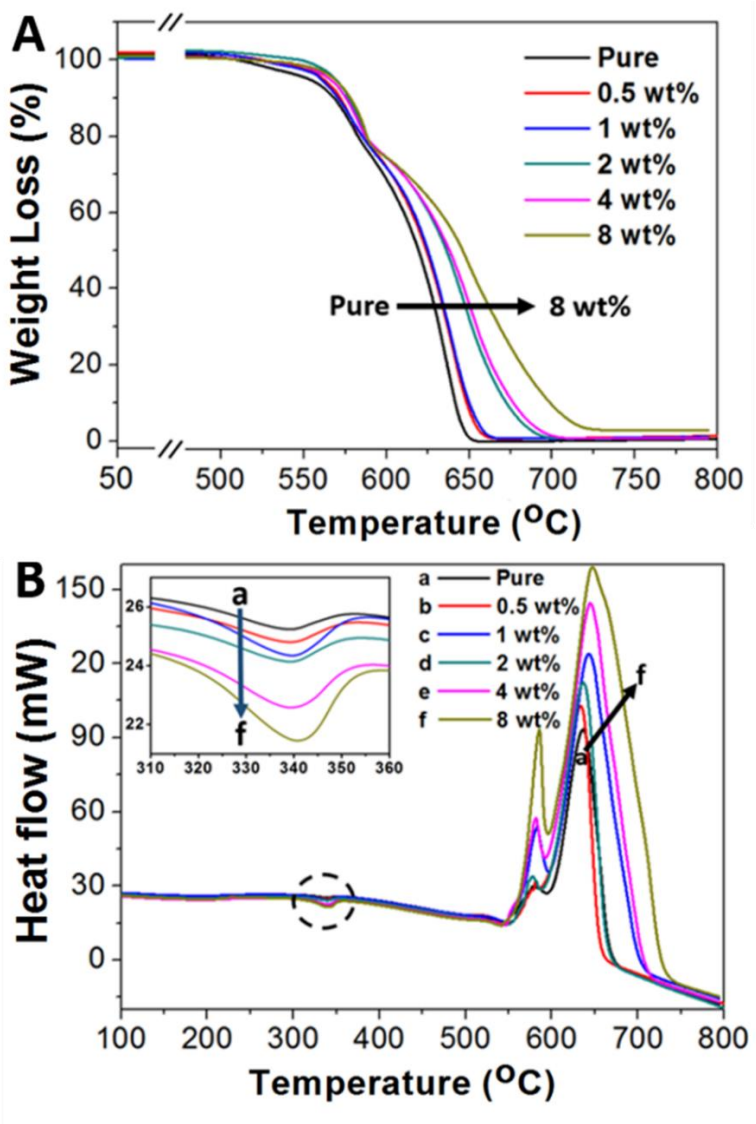

Fig. 6.11 a) TGA curves, and b) the corresponding DSC curves of the pure PEEK and the PEEK/IF-WS_2 nanocomposites.

Furthermore, the gravimetric degradation temperatures are summarised in Table 1. The degradation temperature changes, ΔT, against IF-WS_2 contents, are shown in Fig. 6.12. In Table 1, T_S represents the onset temperature of the degradation, T_{50} and T_M refer to the temperatures subjecting to 50% and the maximum degradation, respectively. The higher degradation temperatures of the composites indicate their better thermal stabilities. As exhibited in Fig. 6.12, the higher the IF-WS_2 contents, the higher the degradation temperatures. The 8 wt% specimen postponed its onset degradation temperature T_S from 498 to 552 ^oC by 54 °C, which is significant and makes them suitable for applications at much demanding environments.

Table 1 TGA results of PEEK/IF-WS_2 nanocomposites obtained under air flow at a heating rate of 10 °C·min^{-1}.

Content (wt%)	*IF-WS_2/PEEK*		
	T_S (°C)	T_{50} (°C)	T_M (°C)
0	498	619	657
0.5	508	625	662
1	515	626	663
2	532	641	701
4	541	645	703
8	552	648	738

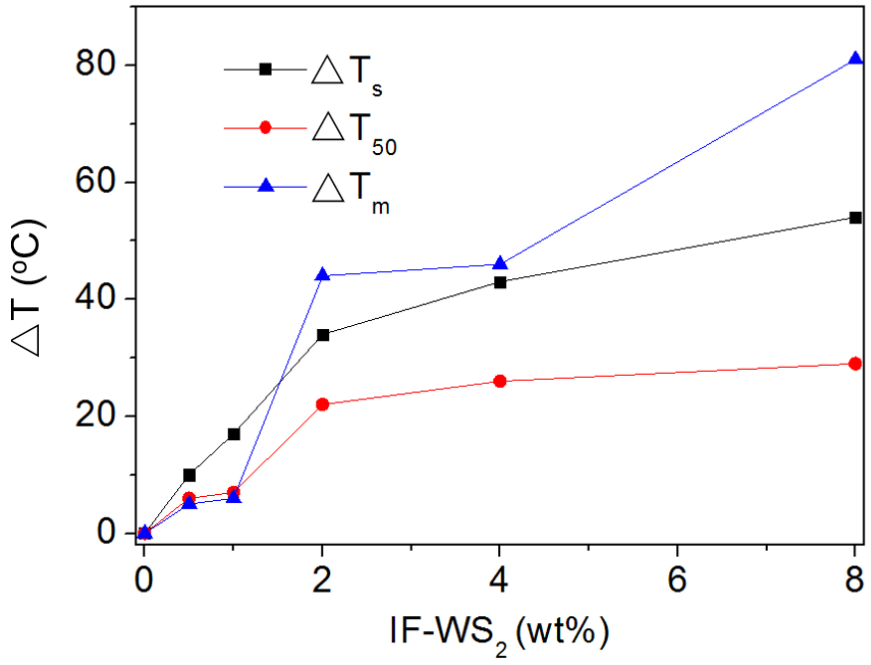

Fig. 6.12 Degradation temperature changes of T_s, T_{50} and T_m all exhibiting a positive relationship versus the IF-WS_2 contents.

Compared with the neat PEEK, the IF-WS_2/PEEK nanocomposites displayed higher degradation temperatures under air atmosphere, and by applying the Kissinger method, equation (2), we calculated the activation energy value (E_a) for the degradation in air for both samples[201].

$$ln\frac{\beta}{T_{max}^2} = -\frac{E_a}{R}\left(\frac{1}{T_{max}}\right) + ln\frac{nAR(1-a_m)^{n-1}}{E_a} \qquad (2)$$

where β is the heating rate, T_{max} is the maximum degradation temperature at different heating rates, E_a is the apparent degradation activation energy value, R is the universal gas constant and the A is a pre-exponential factor, a_m is the fraction reacted, n is the empirical order of reaction.

To calculate E_a from Equ. (2), we assumed the a_m or the weight loss percentage being constant. According to Fig. 6.13, the $ln\,(\beta/T_{max}^2)$ versus $1/T_{max}$ plots at different heating rates, we obtained E_a from the simplified linear equation: $E_a = -\mathrm{R} \times \mathrm{slope}$, 64 and 76 kJ/mol for the neat PEEK and 8 wt% PEEK/IF-WS_2 nanocomposites, respectively. Therefore, the presence of IF-WS_2 NPs has

increased the degradation activation energy, and hence improved the thermal stability of the nanocomposites.

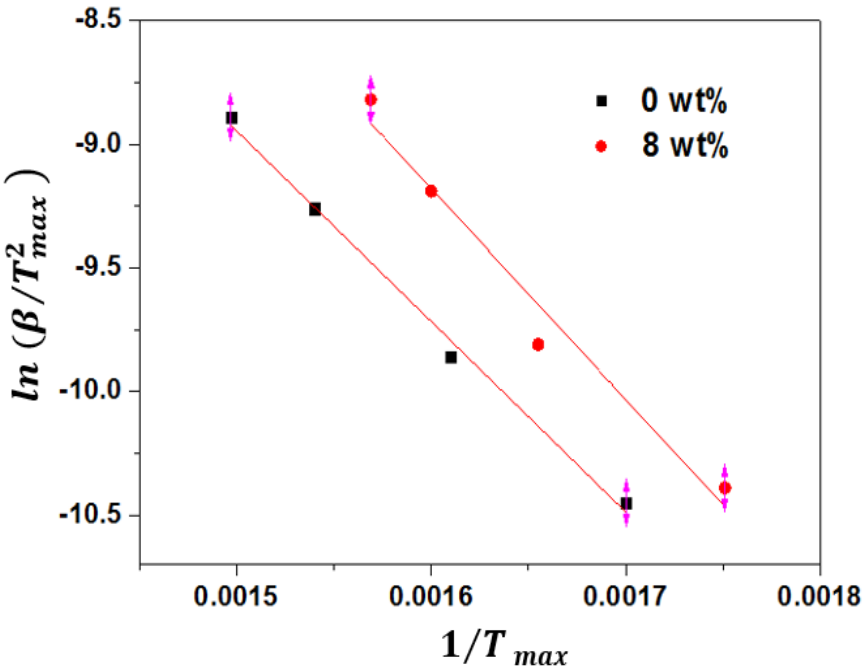

Fig. 6.13 Determination of the activation energy from the Kissinger method for the plain PEEK and the 8 wt% PEEK/IF-WS_2 nanocomposite.

6.4.4 Mechanical Properties (Hardness, Tensile Strength, Tribology)

Hardness

The hardness values plotted in Fig. 6.14 showed that all the composites became harder, and that the highest value was corresponding to the 8 wt% IF-WS_2 sample with 25.1 $HV_{0.5}$, against 18.9 $HV_{0.5}$ of the plain PEEK, which represents a notable 33% improvement. Slightly different from the trend for the tensile strength, the hardness values continued to increase with increased IF-WS_2 additions. However, the growth of the value of Vickers hardness is slow at the beginning from 0 to 0.5 wt%, and then becoming much fast between the 0.5 to 2 wt%, and the increasing speed going down again from 2 to 8 wt%. This is due to that high amounts of particles could not be dispersed completely uniformly within the matrix. From 0.5 to 2 wt%, the mixture nanoparticles were dispersed evenly so that they significantly improved the hardness. However, at

high content situation, the particles started to agglomerate together and it would reduce the efficiency of the reinforcing filler.

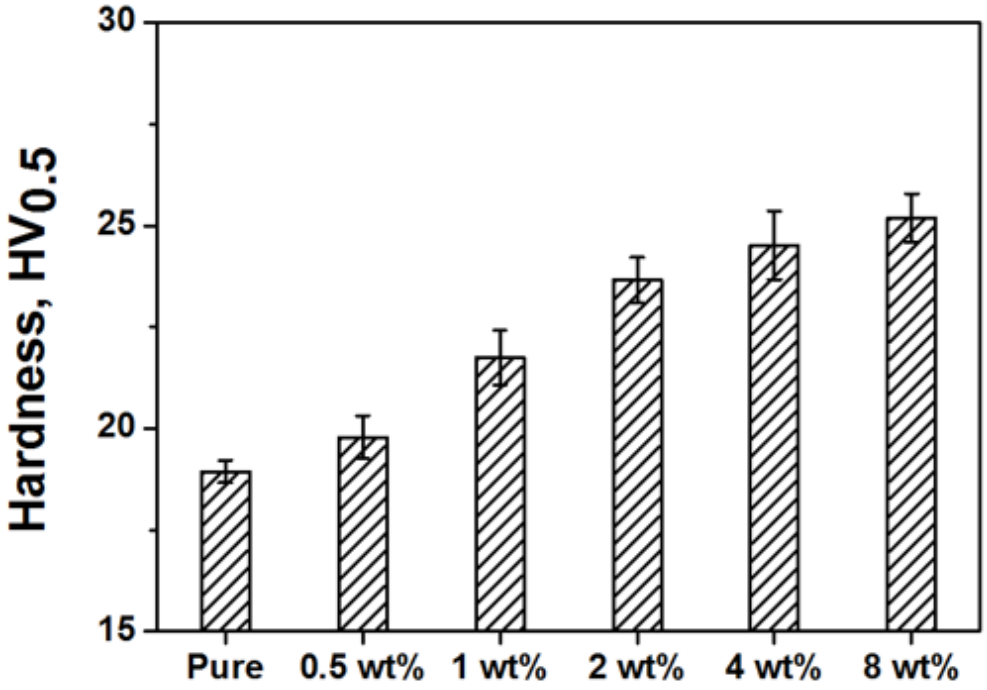

Fig. 6.14 Vickers Hardness results at different IF-WS_2 contents

Tensile Strength

The tensile strengths of composites with different IF-WS_2 contents from 0.5 to 8 wt% are presented in Fig. 6.15a, and the composites have demonstrated a small improvement of 8% against each other. However, against the pure PEEK sample, the 2 wt% composite shows a 24% improvement in the ultimate tensile strength, increased from 77.67 MPa to 96.69 MPa. Further increasing the IF-WS_2 content to 4 wt% resulted in a slight reduction in the tensile strength, which was further deteriorated at 8 wt%, although remained better when compared with the plain PEEK sample.

As shown in Fig. 6.15b, the elongation rates of the nanocomposites however, decreased from *ca.* 80% down to 13% at increased IF-WS_2 content of 0.5 wt% to 1 wt% in the composites, about 60% reduction. This downtrend became much slighter, as further increases of the filler contents of IF-WS_2 from 2 to 8

wt%, the ductility of the nanocomposites appeared to be stabilised, remaining an elongation of around 10% at final break.

The Young's modulus displayed in Fig. 6.15c and d demonstrated the similar changing trend as the ultimate tensile strength against the pure PEEK. However, at 2 wt% the improvement of the Young's modulus is around 27%, which is slightly bigger than the 24% improvement of the tensile strength, with a value of 1.82 GPa. Furthermore, the modulus decrease speed after 4 wt% was still smoother than the change of tensile strength.

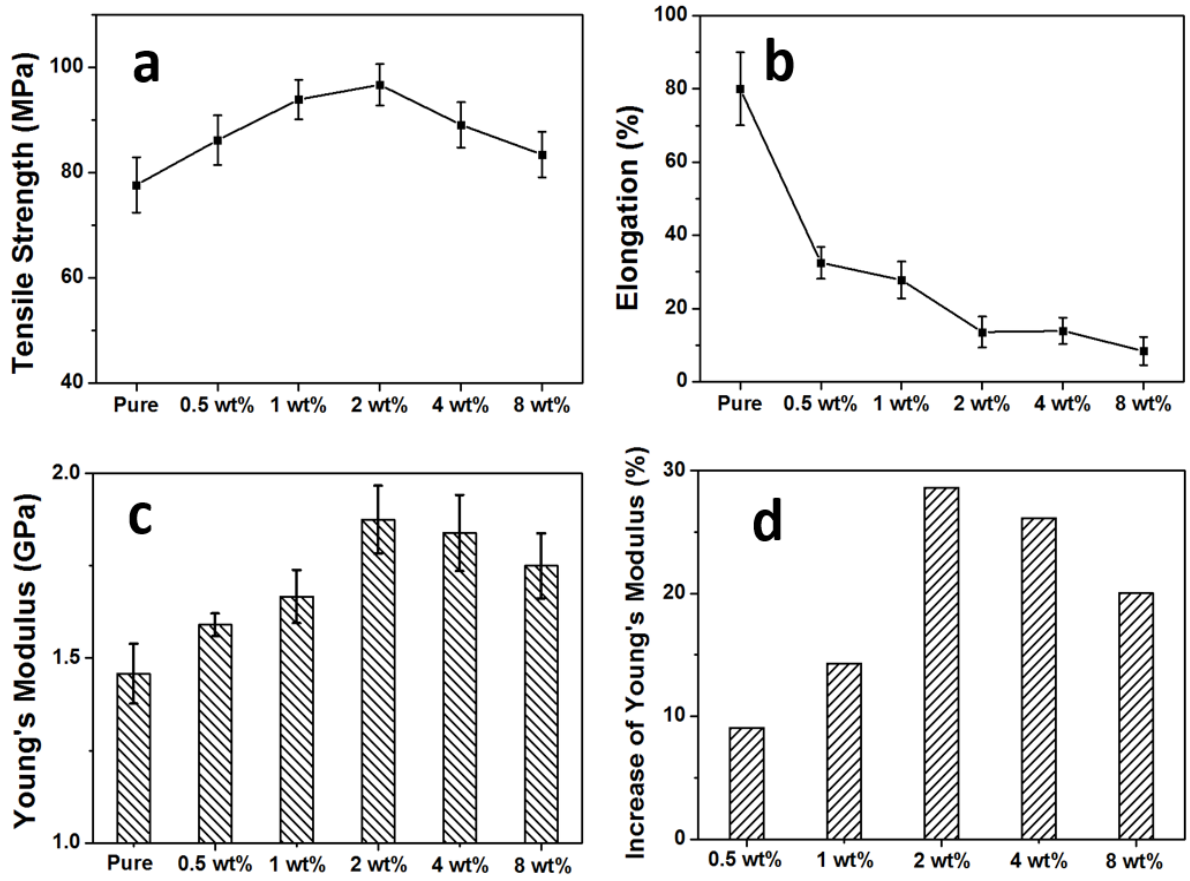

Fig. 6.15 Average tensile strength values and elongation rates at different IF-WS_2 contents.

6.4.5 Tribology analysis

Fig. 6.16a shows the coefficient of friction (COF) of the PEEK/IF-WS_2 nanocomposites with different contents, obtained under the condition of 100 rpm and a pressure of 1 bar. The XRD images shown in Fig. 6.16b has

confirmed that the IF-WS_2 NPs are evenly distributed in the matrices, and at higher filler content the peak intensity of the IF-WS_2 becomes stronger. The 20 wt% specimen shows the unstable testing result due to the loose structure of the block and it is easy to crumble into pieces in the test. Apart from the 20 wt% sample, because the sample block is relative stable during the test, the 8 wt% sample displayed the lowest COF at the beginning process with around 0.25. However, it reduces to the same level with plain PEEK after 400 sec. We expect the COF of the composite reduced significantly as Hou's reported[163], but it did not happen because their samples had no sintering process and just a coating of the board of steel. The bonding with the PEEK matrix is too strong and the IF-WS_2 NPs inside the matrix cannot be released to the surface to form a tribofilm. Furthermore, the dispersal of NPs is great, and as a result only a few IF-WS_2 NPs residual were observed on the surface area after the wear testing. However, even the improvement of the tribological property is not obvious, the COF still improved a bit and maybe it could work in the high loading ambient.

Consequently, the super-lubricating property of the IF-WS_2 did not fully exhibit. However, we believe that under larger pressure conditions, the friction will damage the surface of the PEEK block and the IF-WS_2 embedded inside will find their way out to show their superiority to help reduce the COF.

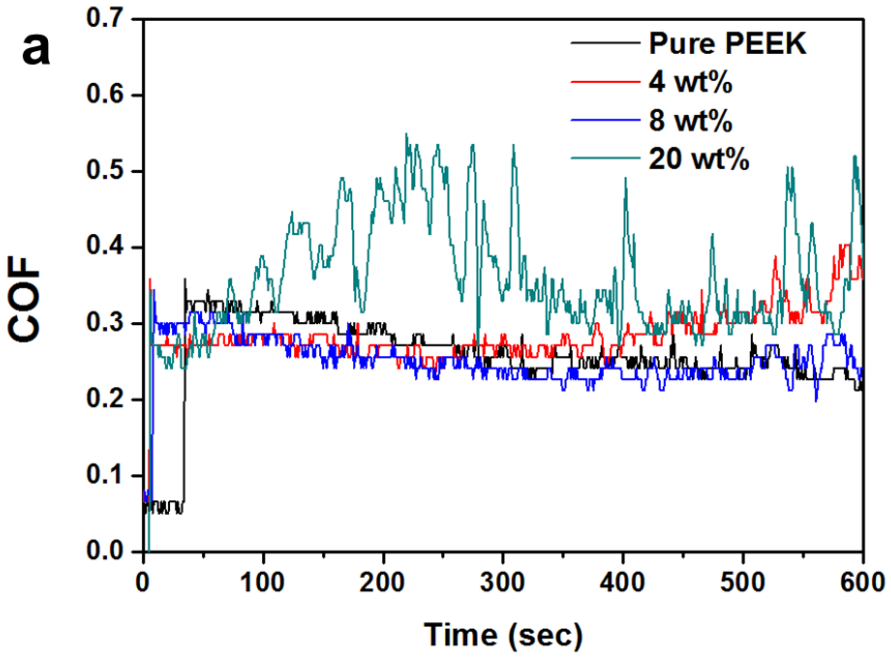

a) The COF of the PEEK/IF-WS_2 at different contents

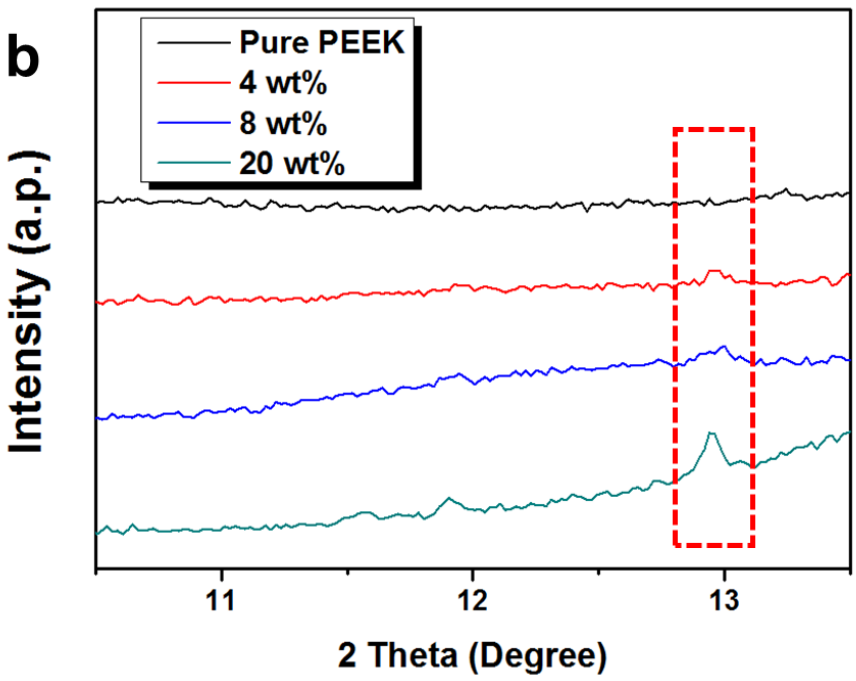

b) The XRD curves after 10 min wearing test.

Fig. 6.16 a) The COF of the PEEK/IF-WS_2 at different contents; b) the XRD curves after 10 min wearing test.

6.5 Conclusion

In summary, the IF-WS_2 NP addition in the PEEK matrix has modified the spherulite crystalline structures by way of affecting the nucleation and crystallisation, increased the overall tensile strength, hardness, Young's modulus, and improved the thermal stabilities and conductivities. Our FTIR and XPS results have further confirmed the existence of both chemical and physical bonding between the IF-WS_2 and the ketone interface in the PEEK. An improvement of 24% in the tensile strength and 27% for the Young's modules (at 2 wt%) has been obtained. A better degradation temperature of over 50 °C has been demonstrated, and such better thermal stability is originated from the increased activation energy in the composites. The thermal conductivity (at 8 wt%) is nearly 2 times higher than that of the plain PEEK material, which can greatly extend its application range.

Chapter 7. Carbon coated IF-WS_2 composite reinforced PEEK matrix

7.1 Introduction

In previous Chapter, we have investigated the simple method to fabricate binary PEEK/IF-WS_2 nanocomposites. To further enhance the potential properties of the composite, the ternary concept of PEEK nanocomposites will be evaluated in this Chapter. Amongst a diverse choice for the reinforcement, the carbon-based nanomaterials and IF-WS_2 nanoparticles have separately attracted most attentions. As the most studied materials in past decades, CNTs and graphene have been explored in various polymer matrices, including PEEK[190, 202]. Meanwhile, owing to the outstanding properties such as superb shock resistance, high thermal stability and conductivity, excellent lubricant performance, as well as that PEEK/IF-WS_2 composites have been investigated intensively, the combination of carbon with IF-WS_2 is thus an interesting selection. Furthermore, many documents have demonstrated that the 2H-WS_2/C mixed composite powders have superior electrochemical properties. It has been found that the introduction of carbon with these particles not only further will enhance the mechanical and thermal properties, but also show extraordinary semiconducting behaviour, which makes the application to develop ternary IF-WS_2@C/PEEK even more attractive.

However, even the 2H-WS_2/C mixture has experienced the issue of carbon separation from the WS_2 flakes, which complicated the situation and restricted them becoming an ideal enhancement phase for ternary PEEK composites. More difficult than the binary system, the ternary-phased nanocomposites will face severer challenges in achieving a uniform nanofiller dispersion within the PEEK matrix. Hence, preparing a WS_2/C composite reinforcement phase, rather than using two reinforcements, appears to be an effective way to counter the dispersion issue. Whitby *et al*. have reported a 2H-WS_2-coated CNT composite phase with exposed WS_2 layer to delay the oxidation process of CNTs significantly[29]. Unfortunately, even though there was a good interface bonding between the WS_2 and CNTs, the poor dispersion ability of the WS_2 within PEEK matrix still restricts their applications.

Given by abundant amount of literature associated with carbon-based CNTs and graphene, which can be used to assist in tackling the dispersion and interface issues, an alternative C-coated IF-WS_2 nanomaterials therefore would be very interesting to be explored. Indeed, Xu *et al.* have documented such IF-WS_2@C nanoparticles, and importantly they have pioneered the large scale production attempt by using a rotary tube furnace, which makes such investigation possible in our laboratory[31, 197]. Furthermore, the thermal stability of the IF-WS_2@C NPs has been significantly improved and the C-coating could help to improve the dispersion of IF-WS_2 NPs and the interface adhesion with the PEEK matrix. Those advantages imply that the IF-WS_2@C NPs are an attractive choice to fabricate ternary IF-WS_2@C/PEEK nanocomposites.

In this chapter, the high performance IF-WS_2@C-PEEK ternary nanocomposites will be prepared, in which the PEEK matrix is reinforced by graphitic C-coated IF-WS_2 composite NPs. The structures, mechanical and thermal properties of the resulting nanocomposites will be characterized systematically by using corresponding methods. We will further analyse the interface formation mechanism of the composites. We will show that improvements of the tensile strength and thermal conductivity of PEEK are originated from the homogeneous dispersion of the IF-WS_2@C NPs within the PEEK matrix. We believe that this research can be widely expanded to fabrications of other PEEK-based nanocomposites.

7.2. Fabrication and discussion of carbon coated IF-WS_2 NPs

7.2.1 Fabrication of IF-WS@C NPs

By fine tuning the RCVD process that we reported earlier, we produced the IF-WS_2 NPs first during the solid-gas reaction stage, and then achieved uniform C coating after the CVD stage. As detailed in Chapter 3, the nanoscale highly graphitic and layered C coating was achieved by using the acetone and styrene mixed solution as carbon source. By controlling the injection rate, reaction time and temperature, can optimise the quality and thickness of the C coating. After numerous experiments, we adopted an optimal set of parameters, of which the solution volume ratio is 4:1, at 2 $ml \cdot h^{-1}$ injection rate, at 700 – 900 °C and under Ar atmosphere. Especially, the 30 and 60 min durations were studied, and the resulting samples were named as IF-WS_2@C-30 and IF-WS_2@C-60, respectively.

7.2.2 Structure and morphology of IF-WS@C NPs

XRD characterisation

As shown in Fig. 7.1, the XRD patterns of the IF-WS_2@C NPs, as well as the pristine IF-WS_2 NPs, synthesised at 775°C, show that all peaks labelled with a triangle match the major peaks of IF-WS_2. The peak with the highest intensity occurred at $2\theta = 14.3°$ corresponds to the (002) of WS_2, which is also prominent in the IF-WS_2@C NPs. In the enlarged patterns on the dash square of Fig. 7.1, a tiny peak is visible at 26.2°, which is attributed to the (002) plane of graphitic carbon[31]. The low (002) intensity ratio between carbon and IF-WS_2, *i.e*. the weak (002) graphitic peak, is owing to the small amount of carbon in the IF-WS_2@C NPs. For the same reason, the carbon content difference between the IF-WS_2@C-30 and the IF-WS_2@C-60 samples cannot be clearly recognised under the XRD, due to its resolution limit.

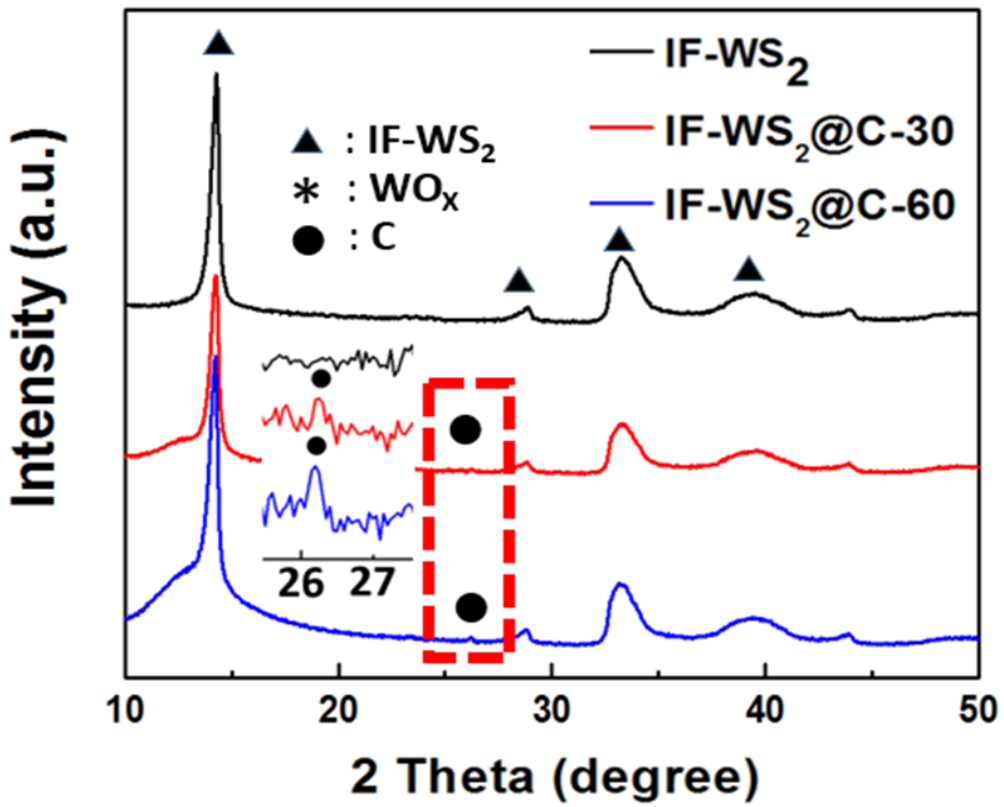

Fig. 7.1 XRD patterns of pristine IF-WS_2 and IF-WS_2@C NPs

TEM characterisation

The HRTEM images in Fig. 7.2, can reveal the different coating thicknesses between the long and short time created IF-WS_2@C NPs. As shown in Fig. 7.2a and b, both images display the bright contrast C layer and the dark IF-WS_2 core with the marked polygonal cage structure. The corresponding inset of HRTEM images in both Fig. 7.2a and b further demonstrates the lattice distance of 0.62 nm for the dark core part and 0.34 nm for the light surface layer, which is corresponding to the (002) plane of WS_2[203] and graphitic carbon respectively. The HRTEM images also show that the continuous C coating is around 1 nm thick for IF-WS_2@C-30 and 2 nm for the IF-WS_2@C-60 NPs. These results demonstrate that the quality of the IF-WS_2@C NPs produced by the current RCVD process are of high, uniform and with controllable C-coating thickness, thus we have confidence for them to be used as a composite reinforcement filler in PEEK matrix.

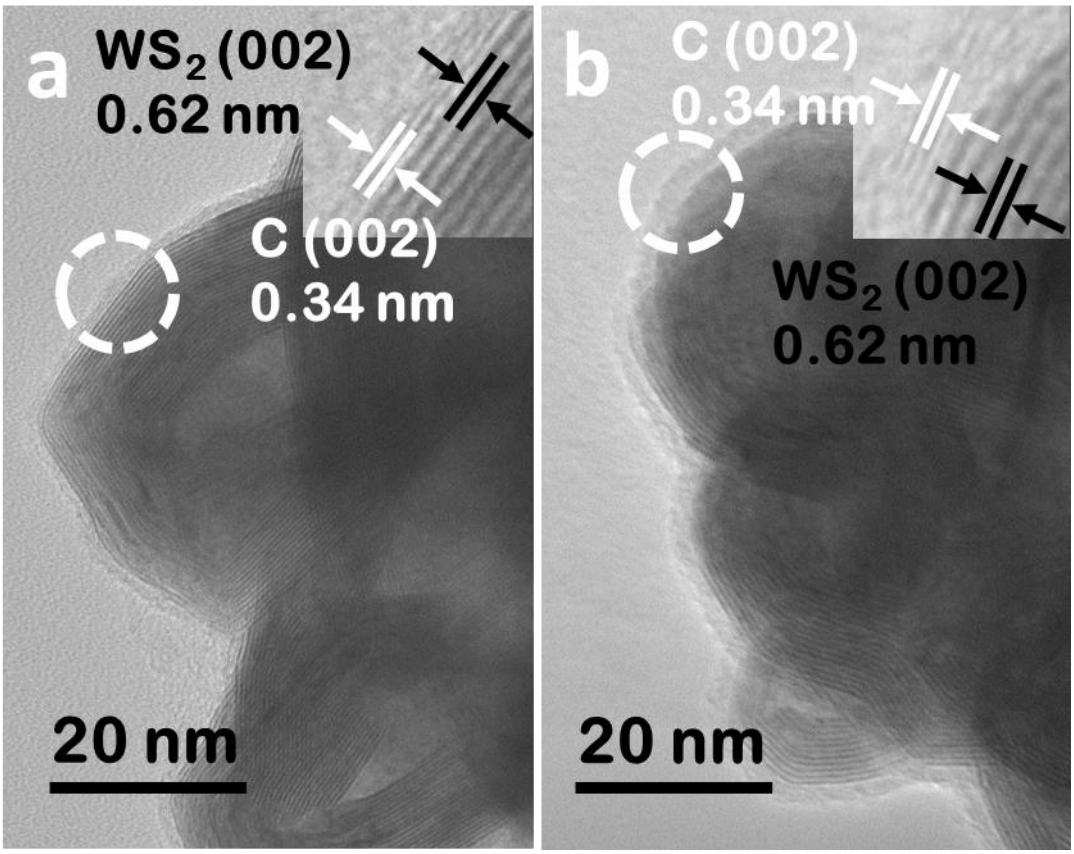

Fig. 7.2 the HRTEM images of IF-WS_2@C-30 and IF-WS_2@C-60 NPs.

7.3 Characterisation and discussion of IF-WS_2@C-PEEK nanocomposites.

7.3.1 Structure characterisation

Before the melting process, we surveyed the pure PEEK and PEEK based mixtures of different loadings of NPs by using XRD, as shown in Fig. 7.3a and b, to set a standard for comparison with their sintered composites. For the IF-WS_2@C-30-PEEK powder diffraction patterns, the strong peak at *ca*. 14° corresponding to the (002) plane of the WS_2 (Fig. 7.1) was observed in the nanocomposites, and its relative intensity increased with increased IF-WS_2 concentrations. The three peaks appeared at 20.8, 22.8 and 28.9° were the characteristic diffractions of the (110), (113) and (200) planes of PEEK,[155, 157] respectively. These peaks all became sharper and stronger after sintering for both the neat PEEK and their nanocomposites, compared with the powder mixtures, which is believed to be raised from crystal growth and better crystallisation. Almost identical features also occurred to the IF-WS_2@C-60-

PEEK samples (Fig. 7.3c and d). By examining the full width at half maximum (FWHM) of the (110) peak in Fig.7.3b and d for the sintered samples, it is clear that the peak became broader at higher IF-WS_2@C contents. A broadened peak indicated the shrinkage of the crystalline sizes. The dispersion of IF-WS_2@C NPs in the PEEK matrix would promote the nucleus formation and possibly physically hinder the growth of the PEEK spherulitic crystals. Therefore, at increased content of the IF-WS_2@C NPs, more IF-WS_2@C NPs would be able to act as tiny primary cores and promote the recrystallization of PEEK, leading to the slightly enlarged FWHM values. This result indirectly confirmed the good quality of dispersion of the NPs, because a poor and heavily agglomerated dispersion at high NP fraction would not be able to generate such a crystalline reduction impact. Direct morphological analyses will be followed.

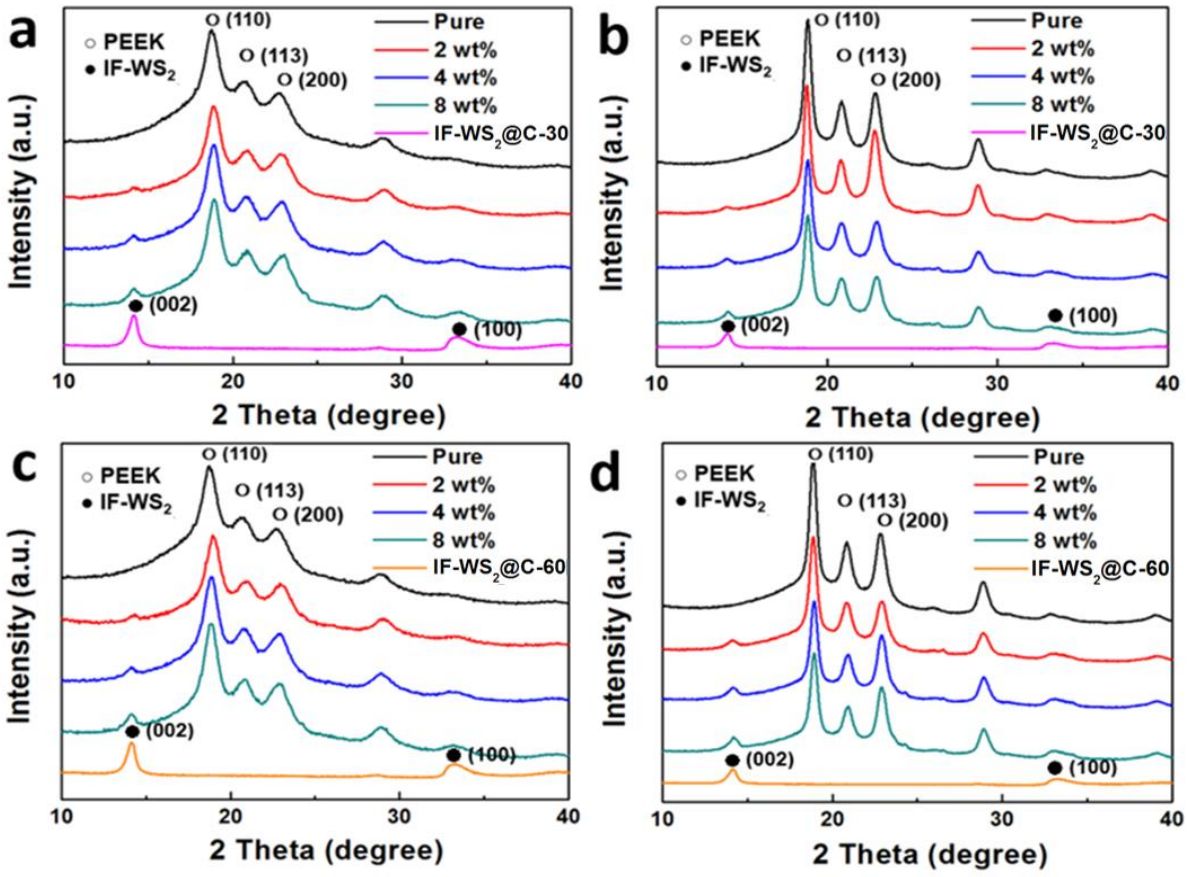

Fig. 7.3 XRD patterns of powder mixture of IF-WS_2@C-PEEK before (a, c), and after (b, d) sintering crystallisation.

7.3.2 Morphology (SEM with EDS, TEM)

SEM with EDS

The pure PEEK after melting showed a smooth surface, consisting of large irregular spherulites which formed by many tiny granular structures, as shown in the SEM images in Fig. 7.4a. The bright spots with high contrast in the back-scatter SEM images in Fig. 7.4c and d were from the 2 wt% IF-WS_2@C-30 and IF-WS_2@C-60 PEEK composites, respectively. The high contrast patterns were originated from the IF-WS_2@C NPs, as further confirmed by the mapping scan EDS in the dashed circle area (Fig. 7.4b and c). The IF-WS_2@C NPs appeared to be distributed very well within the matrix for both IF-WS_2@C-30 and IF-WS_2@C-60 NPs. At 8 wt% NPs addition, the distribution of the high contrast spots looked consistently homogenous, without obvious agglomerations. Fig.7.4e and f displayed the 8 wt% IF-WS_2@C-30-PEEK and IF-WS_2@C-60-PEEK composites. Although we could not clearly establish a statistic link between the IF-WS_2@C contents with the spherulite sizes based on limited number of images, it is evident that the bright IF-WS_2@C NPs were well-dispersed and embedded inside the PEEK spherulites. This will be further evaluated by the effect on their mechanical properties.

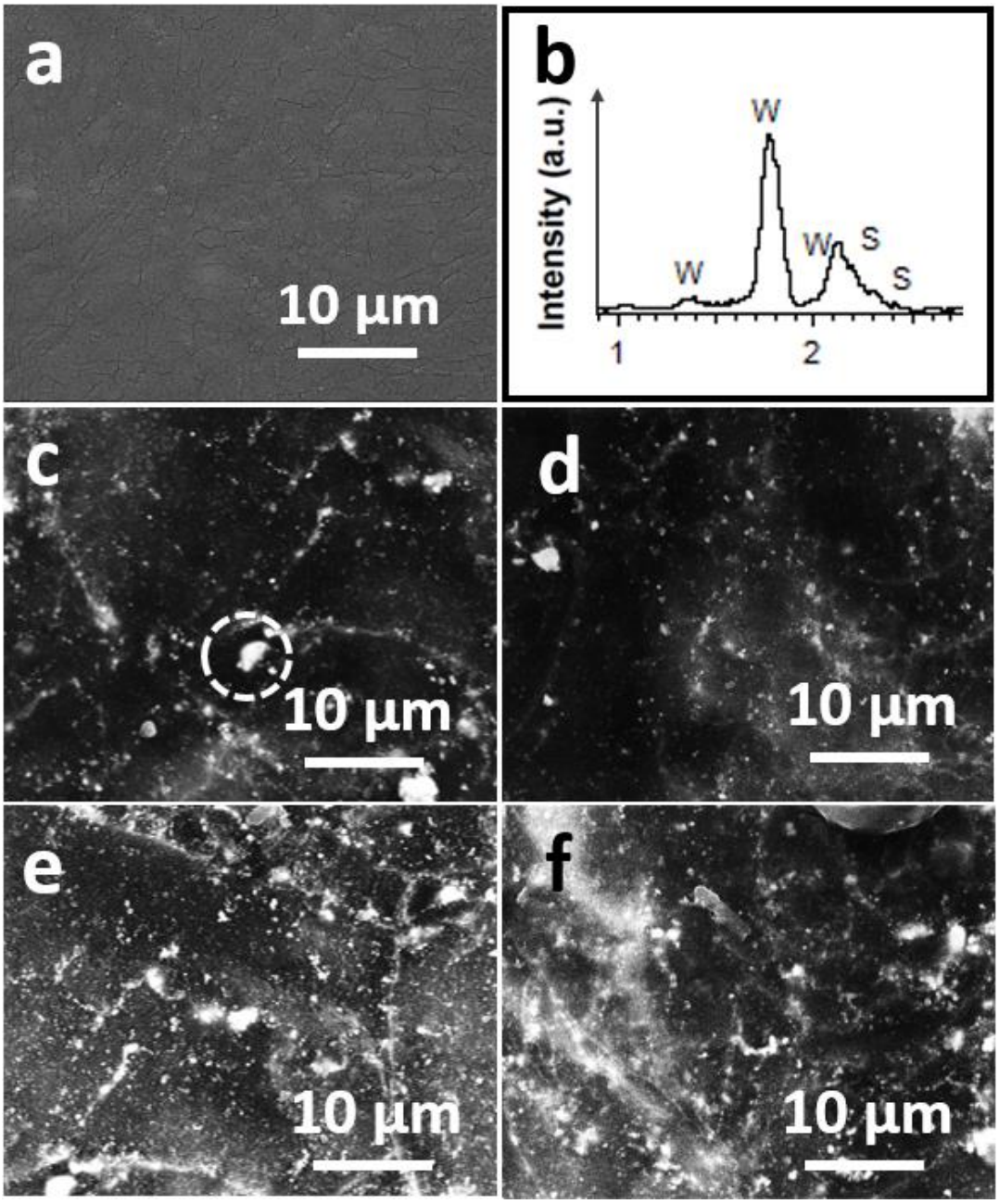

Fig. 7.4 a) Secondary SEM image of the neat PEEK after melting; b) EDS analysis recorded from the circle in c); c) and d) Back-scatter SEM images of the PEEK nanocomposites containing 2 wt% of IF-WS_2@C-30 and IF-WS_2@C-60, respectively; e) and f) Back-scatter SEM images of the 8 wt% IF-WS_2@C-30 and IF-WS_2@C-60 NPs in PEEK, respectively .

TEM

Not like the previous TEM images taking under the 200 kV acceleration voltage, the TEM in this session was operated at 120 kV, which can avoid structural damage to the polymer by the electron beam. As shown in Fig. 7.5a, the granular structure of the dark IF-WS_2@C was easily visible against the bright PEEK matrix that exhibited as irregular spherulitic structures. At low concentration (2 wt%), the IF-WS_2@C-30-PEEK exhibited a similar distribution characteristic to the IF-WS_2@C-60-PEEK sample, appearing as individual NPs (Fig. 7.5b and d) mixed with clusters of small agglomerations (Fig. 7.5a and c). Whilst individual NPs were embedded in the centre of spherulites, the clusters were also seen as the core surrounded by the spherulite, as shown in Fig. 7.5a. As displayed in Fig. 7.5e and f, even for the 8 wt% content composite, the distribution of IF-WS_2@C NPs was still fairly homogenous at the micrometre scale. The similar distribution behaviours between the IF-WS_2@C-30-PEEK and IF-WS_2@C-60-PEEK NPs have convincingly demonstrated that the C coating was indeed worked in the composites, and the carbon-PEEK interaction dominated the interface process, regardless the inside content of IF-WS_2. This result is very useful, as vast opportunities could be opened for tailoring desired properties of nanocomposites by using this facile C-coating strategy to different NPs.

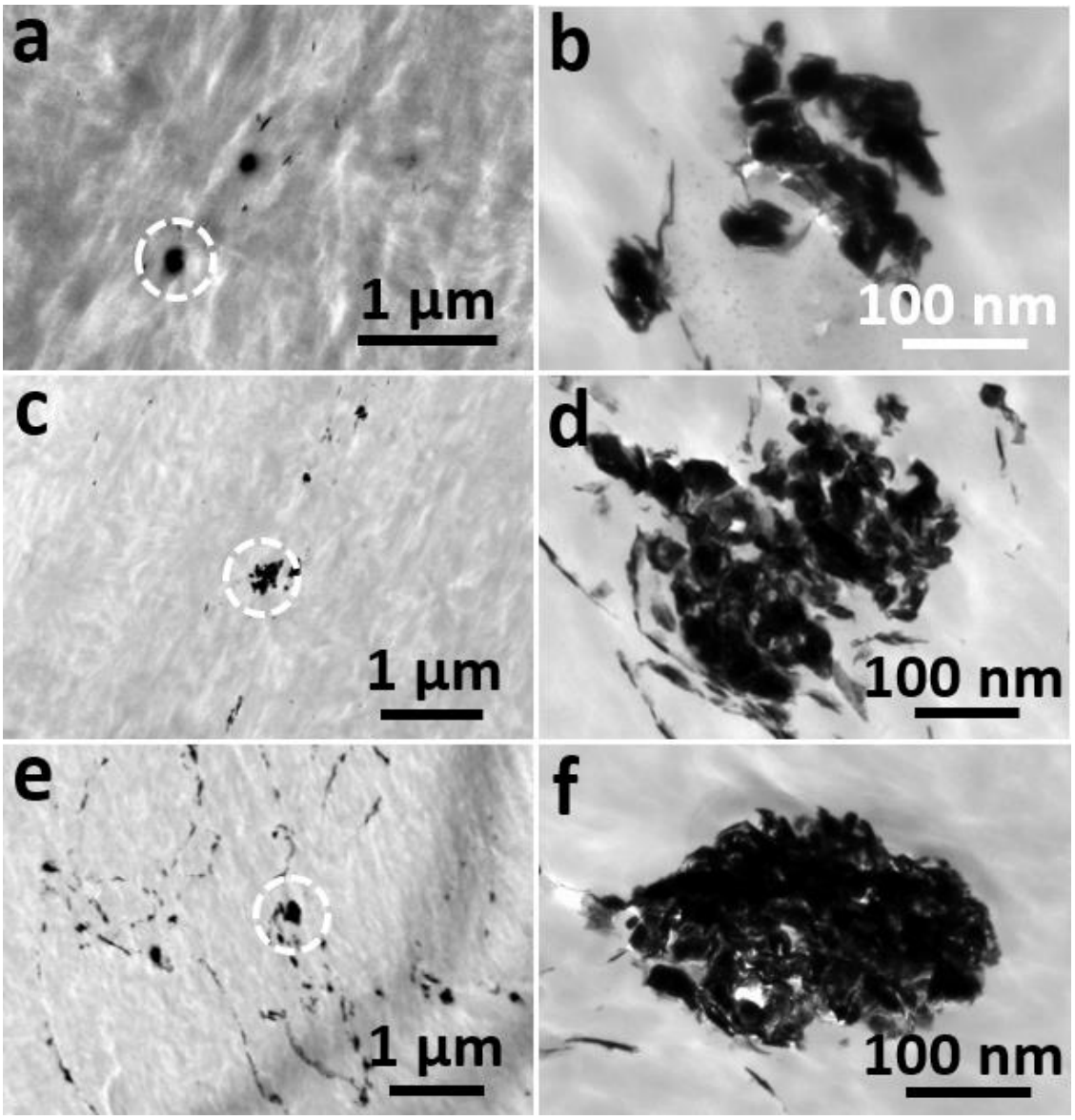

Fig. 7.5 TEM images. (a, b) 2 wt% IF-WS_2@C-30-PEEK; (c, d) 2 wt% IF-WS_2@C-60-PEEK, and (e, f) 8 wt% IF-WS_2@C-60-PEEK nanocomposites.

7.3.3 Spectra analysis (FTIR, XPS)

The interface interaction was investigated by analysing the FTIR and XPS spectra together, on two sets of samples (IF-WS_2@C-30-PEEK and IF-WS_2@C-60-PEEK) with different NP concentrations. The peaks at 1658 cm^{-1} and 1240 cm^{-1} in the FTIR spectra shown in Fig. 7.6a belong to the keto group, originated from the vibration of carboxylic acid of C=O stretching. The three peaks around 1591 cm^{-1}, 1493 cm^{-1} and 1363 cm^{-1} are ascribed to the C-H band of in-of-plane bending benzene vibration, and other peaks at 946 cm^{-1},

840 cm^{-1} and 764 cm^{-1} are assigned to the out-of-plane bending vibration of benzene ring. The band at 1157 cm^{-1} is originated from the ether linkage (C-O). All these similar FTIR spectra are based on features of the PEEK, indicating that the original PEEK structure has not been damaged by the inclusion of IF-WS_2@C NPs. The IF-WS_2@C NPs features are not reflected by this technique[85, 200]. The coated carbon outside the NPs is not noticeable by FTIR as the content is just a tiny amount and there contains no functional groups. Also because of the carbon coating separating IF-WS_2 with PEEK, the 1037 cm^{-1} is no change anymore. Thus we need further XPS study for this.

As shown in Fig. 7.6b, the XPS investigations demonstrate the elemental composition on the surface of composite and the spectra were focused on the $C1_S$ spectra of 3 samples, the IF-WS_2@C, plain PEEK and IF-WS_2@C-PEEK composites with 8 wt% NPs. The C-C bonding for all materials exhibited clearly around the binding energy BE = 284.8 eV. The ether and ketone bonds from the PEEK were displayed at BE = 286.3 eV and BE = 288.2 eV, respectively[178, 200, 204]. The tiny C=O peak appeared in the IF-WS_2@C spectrum was possibly originated from the carbon source (acetone). The most interesting phenomenon was the obviously increased intensity of the broad peak around BE = 292 eV. The IF-WS_2@C-PEEK composite exhibited a much stronger intensity at BE = 291.9 eV than either the IF-WS_2@C or the PEEK alone. The sp2 hybrid orbit of benzene plane (π-π*) in PEEK was reported a BE = 292.2 eV, whilst graphitic carbon that had a similar hexagonal-ring structure was reported to have the similar sp2 hybrid vibration mode with BE = 292.1 eV in the IF-WS_2@C sample[205]. It was uneasy to distinguish the two peaks due to the overlap, however the significantly increased intensity for the broad carbon shakeup peak at 291.9 eV in the composite was believed to be a result of interface reaction between carbon and PEEK during sintering. It was likely that when the carbon hexagonal-ring of the IF-WS_2@C NPs faced the benzene planes of the PEEK, they formed a chemical bonding via π-π stacking, hence the much larger broad peak was observed. This chemical bonding would help to create strong and stable linkages between the IF-WS_2@C and PEEK, which would be stronger than a physically bonded interface, thus improved mechanical and physical properties, which will be verified later.

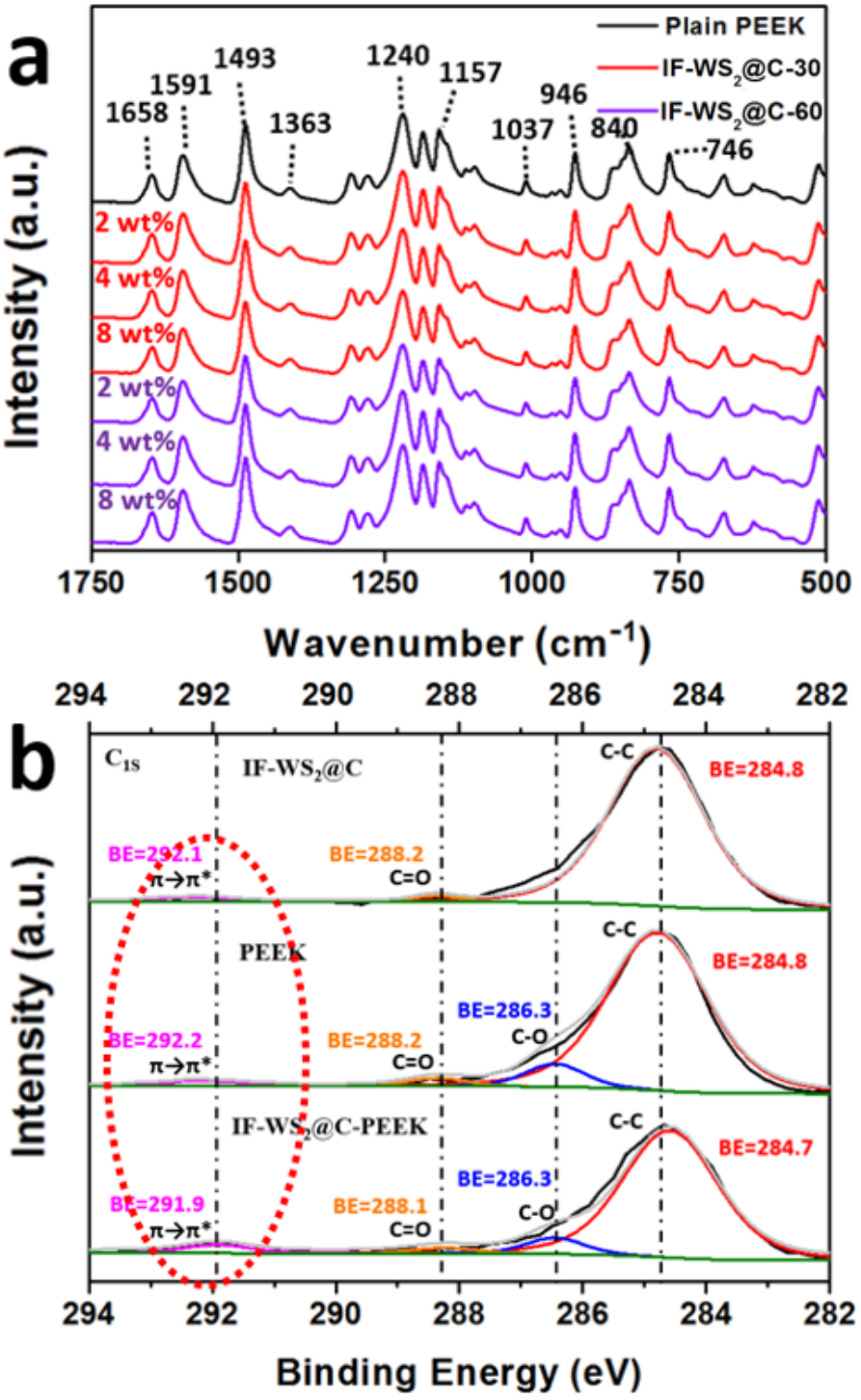

Fig. 7.6 a) FTIR spectra and b) XPS results of the C 1_S of the IF-WS_2@C-30 and its derived PEEK nanocomposites.

7.3.4 Thermal properties (Thermal stability, Thermal conductivity)

Thermal stability

The thermal stability of IF-WS_2@C-PEEK samples are shown in Fig. 7.7a and c, and their corresponding DSC curves on melting point are presented in Fig. 7.7b and d, respectively. The T_S represents the onset temperature of the degradation and T_M refers to the temperature at maximum degradation, respectively. As summarised in Table 2, the higher the IF-WS_2@C contents, the higher the degradation temperatures, the higher the starting degradation temperatures of the composites, and the better the thermal stabilities. The IF-WS_2@C-60-PEEK composites showed a slightly higher degradation temperature than the IF-WS_2@C-30-PEEK, which was due to the different thickness of their C coating. The 8 wt% addition notably postponed the onset degradation temperatures of the two C-coated composites by 57 and 60 °C, respectively. Compared with the IF-WS_2-PEEK composite (54 ^oC improvement, at 8 wt%), these results show a slight improvement. Moreover, they also exhibited a stable platform stage (Fig. 7.7a, for pure to 8 wt%) before the degradation starting period. Therefore, those results have demonstrated the role of C coating in improving the thermal stability of the composites, suggesting that these composites could widen their application potentials towards much demanding environments.

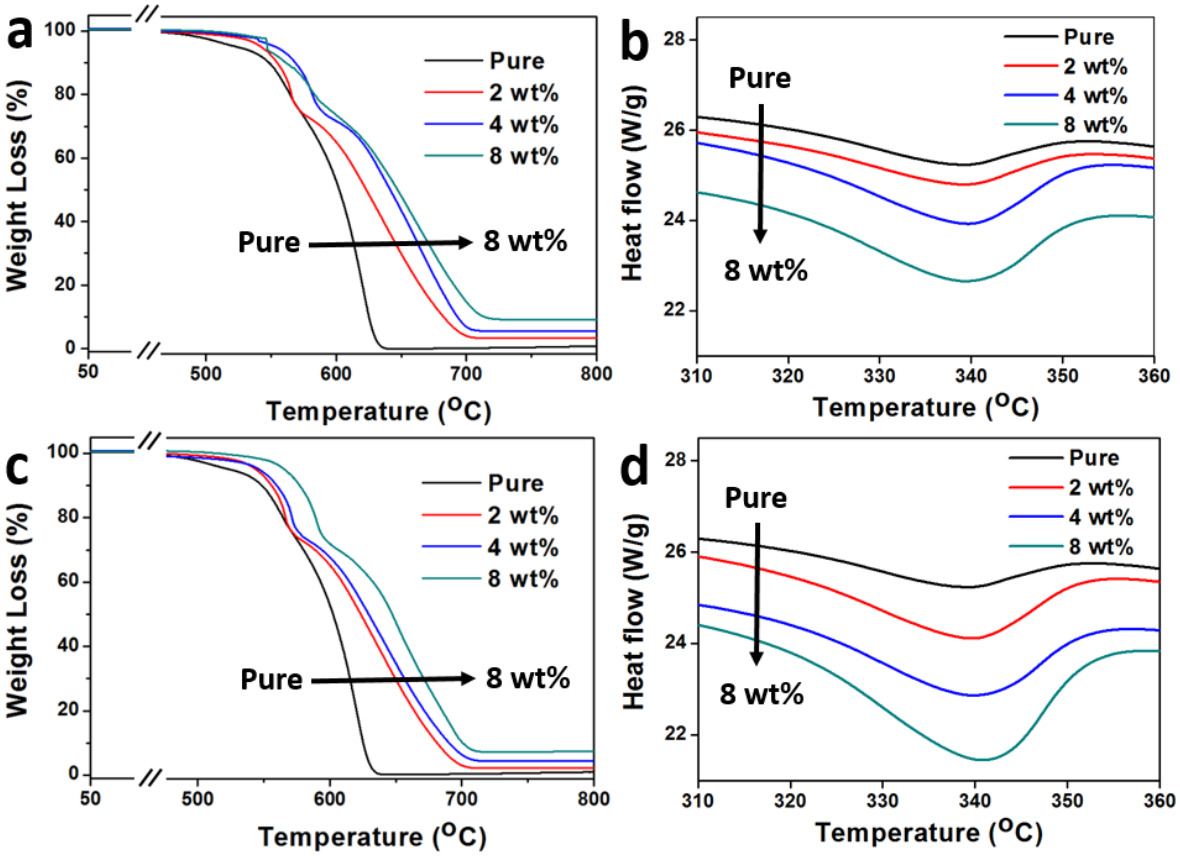

Fig. 7.7. TGA curves (a, c) and the corresponding DSC curves around the melting point (b, d) of the IF-WS_2@C-30-PEEK and IF-WS_2@C-60-PEEK composites respectively.

Table 2. Gravimetric degradation temperatures of IF-WS_2@C-PEEK nanocomposites

Content (wt%)	*IF-WS_2@C-30*		*IF-WS_2@C-60*	
	T_S (°C)	T_M (°C)	T_S (°C)	T_M (°C)
0	487	641	487	641
2	516	702	523	706
4	531	706	538	711
8	544	714	547	716

According to the TGA analysis, the IF-WS_2@C-PEEK nanocomposites exhibit higher degradation temperatures. By further applying the Kissinger method, and using the same Eq. (2) described in Chapter 6, the activation energy (E_a) of the

degradation in air for these samples have been calculated based on the data in Table. 2, to compare the thermal stability.

$$ln\frac{\beta}{T_M^2} = -\frac{E_a}{R}\left(\frac{1}{T_M}\right) + ln\frac{nAR(1-a_m)^{n-1}}{E_a} \qquad (2)$$

The two 8 wt% IF-WS_2@C-PEEK samples were measured with various heating rates of 10, 20 and 40 °C·min^{-1}, respectively. In the calculation of E_a using the equation, we have assumed that a_m is a constant, and then we can obtain a simplified linear equation: $E_a = -R \times slope$ by plotting $ln\ (\beta/T_M^2\ )$ versus $1/T_M$ at different heating rates and the results are shown in the Fig. 7.8. The apparent degradation activation energy is 61 kJ·mol^{-1} for the neat PEEK450PF and 79 kJ·mol^{-1} for the pristine IF-WS_2 reinforced PEEK composites. However, IF-WS_2@C-PEEK nanocomposites have exhibited much higher values of 93 and 97 kJ·mol^{-1} for the thin and thick C-coating applied, respectively. This *c.a*. 50% increase in the degradation activation energy, attributed to carbon coating on the IF-WS_2 NPs, also support the improved thermal stability of the nanocomposites.

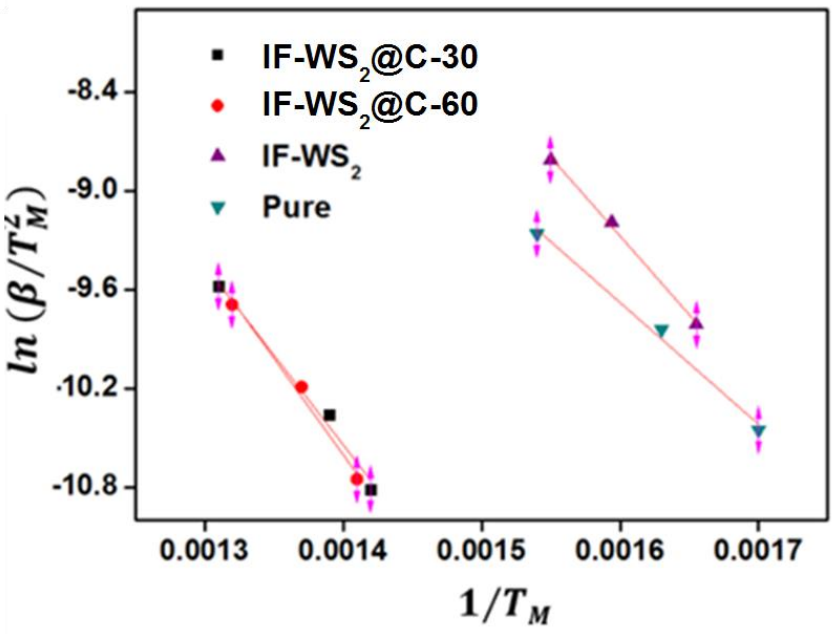

Fig. 7.8 Determination of the activation energy using the Kissinger method for the neat PEEK, 8 wt% IF-WS_2-PEEK and the 8 wt% IF-WS_2@C-PEEK nanocomposites.

Thermal conductivity

Fig. 7.9a presents the thermal conductivities of different composites evaluated at 25 °C. The neat PEEK gave a value of 0.248 $W \cdot m^{-1} \cdot K^{-1}$, in line with literature, whilst the composites all showed much higher values that increased with increasing the NP content concentration. In particular, both of two C-coated IF-WS_2 composites (IF-WS_2@C-30-PEEK and –60-PEEK) exhibited dramatically higher thermal conductivities than both the neat PEEK and IF-WS_2-PEEK composites. For example, the conductivity of the IF-WS_2@C-60-PEEK composites was measured with 61, 134 and 235% improvements, against the neat PEEK, for the 2, 4 and 8 wt% of NP additions respectively (Fig. 7.9b). This result has clearly confirmed again the effective role of IF-WS_2@C NPs in the fabrication of composites, better than the pristine IF-WS_2 NPs.

The thermal conductivity of composites is associated with the crystalline structure of the PEEK matrix, the intrinsic nature of the filler and its distribution, and importantly the quality of the interface structure. Layered carbon in the form of CNTs, graphene and even graphite all has extraordinary thermal conductivities. The presence of a very thin a few layered graphitic C-coating on the IF-WS_2 exhibits a similar structural feature to the carbon nano-onions—an analogue of CNTs, therefore is expected to benefit the thermal conductivity. It is obvious that the distribution of the filler within the matrix will also affect the crystal structures of the matrix, however the synergy between the filler and the PEEK interface is likely to have played a dominant role in this context, as proposed for many CNT-reinforced polymeric composites. As a discontinuous particulate reinforcement in this case, the interface synergy would be more important. Our TEM observation and XPS analysis above have both revealed the formation of a good interface in the IF-WS_2@C-PEEK composites. Therefore, the 235% improvement is very convincing.

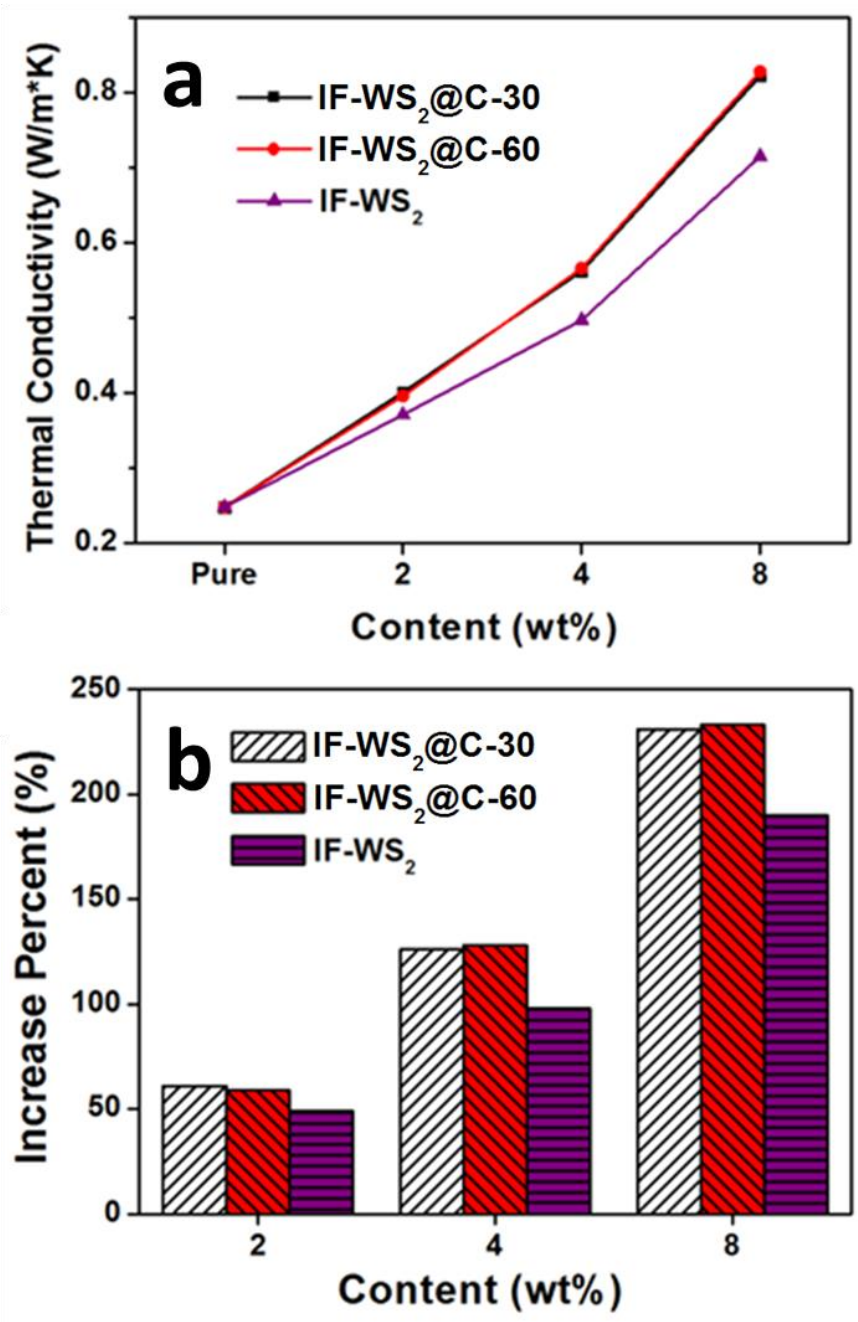

Fig. 7.9 a) and b) Thermal conductivity of the IF-WS_2-PEEK and IF-WS_2@C-PEEK nanocomposites against the neat PEEK.

7.3.5 Mechanical properties (Tensile test, Vickers hardness test)

Tensile test

Fig. 7.10a displays the ultimate tensile strength and its corresponding elongation percentage of pure PEEK, the complementary IF-WS_2-PEEK and IF-WS_2@C-PEEK nanocomposites with NP contents ranging from 2 to 8 wt%. Compared with the neat PEEK sample, the ultimate tensile strength of the 2 wt% composites increased from 78 MPa to 116 and 121 MPa for IF-WS_2@C-30-PEEK and IF-WS_2@C-60-PEEK respectively. Further increasing the IF-WS2@C content to 4 wt% resulted in a significant deterioration in the tensile strength. Because there existed some more agglomerations inside the composite to cause the weak tensile strength, which is corresponding to the TEM imaging result. However, it was still better than the plain PEEK sample. In addition, the 8 wt% composite showed serious agglomerations and exhibited the worst values. All samples showed a similar tendency in the tensile strength when increasing the filler content, but the two C-coated IF-WS_2 composites exhibited significant improvements against those neat PEEK and IF-WS_2-PEEK composites.

Fig. 7.10b shows the common situation that the composites become brittle when the filler content increases. Whilst the elongations of all composite specimens became worse than the neat PEEK, from *ca.* 60% down to 10% for IF-WS_2 and 5% for IF-WS_2@C. The IF-WS_2@C-PEEK nanocomposites showed a good dispersal ability, which confirms the better improvement in mechanical property than IF-WS_2/PEEK composite. However, due to the better dispersal ability of the IF-WS_2@C NP, the more smooth filler NPs distribution resulted in the extra decrease of elongation at 2 and 4 wt%, compared with the IF-WS_2/PEEK composite. When the filler content reached 8 wt%, all composites displayed the similar elongation rate.

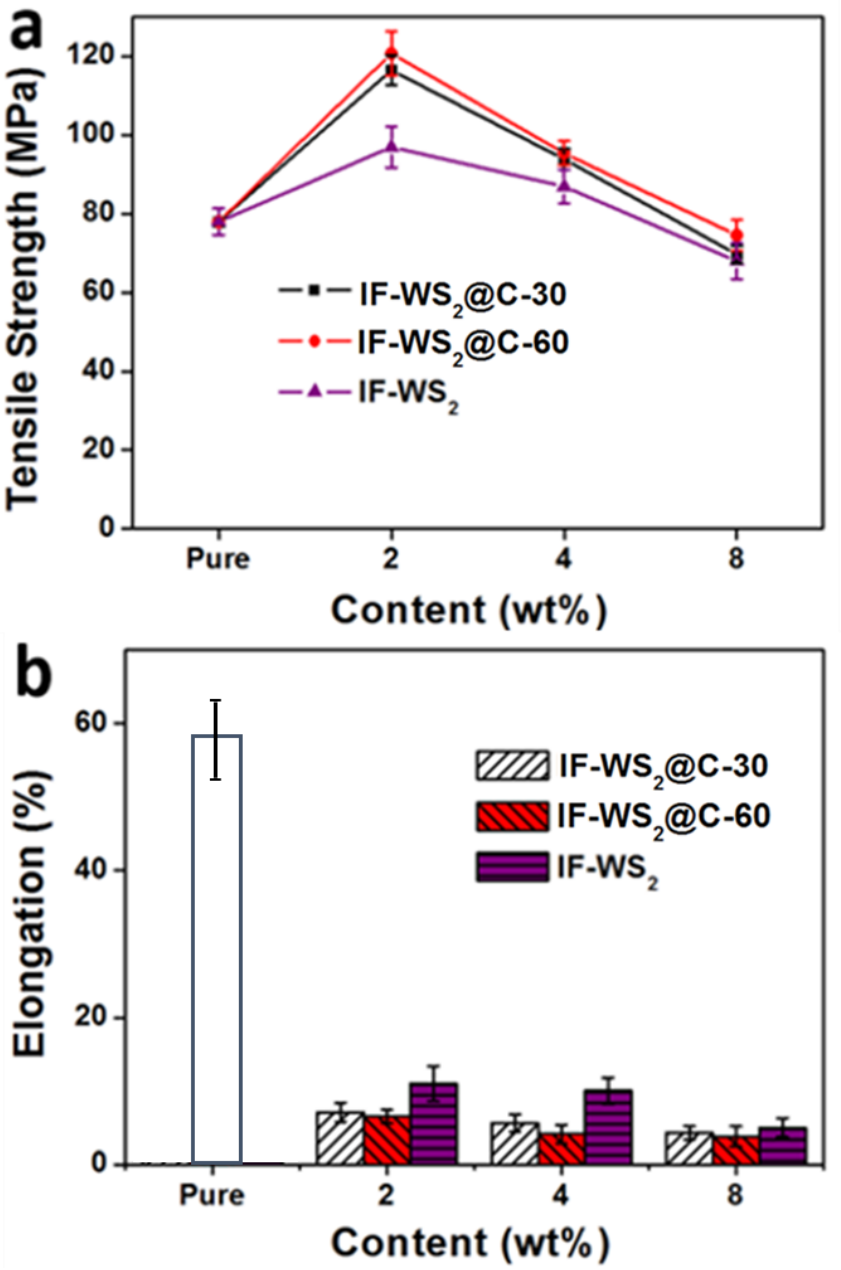

Fig. 7.10 The average ultimate tensile strength and its corresponding elongation percentage

Vickers hardness test

The Vickers hardness values (HV) with different filler contents are shown in Fig. 7.11a. All results are much higher than that of pure PEEK. The highest HV values are obtained from the 8 wt% IF-WS_2@C-30-PEEK and IF-WS_2@C-60-PEEK samples, being 27.1 and 26.9 $HV_{0.5}$, respectively, which represents an over 40% improvement against the neat PEEK (18.9 $HV_{0.5}$). Moreover, Fig.

7.11b also shows the tendency in hardness values that increases with increasing filler amounts. Meanwhile, all composites containing C-coated IF-WS_2 NPs exhibit a greater improvement effect than that of the pristine IF-WS_2 reinforcement.

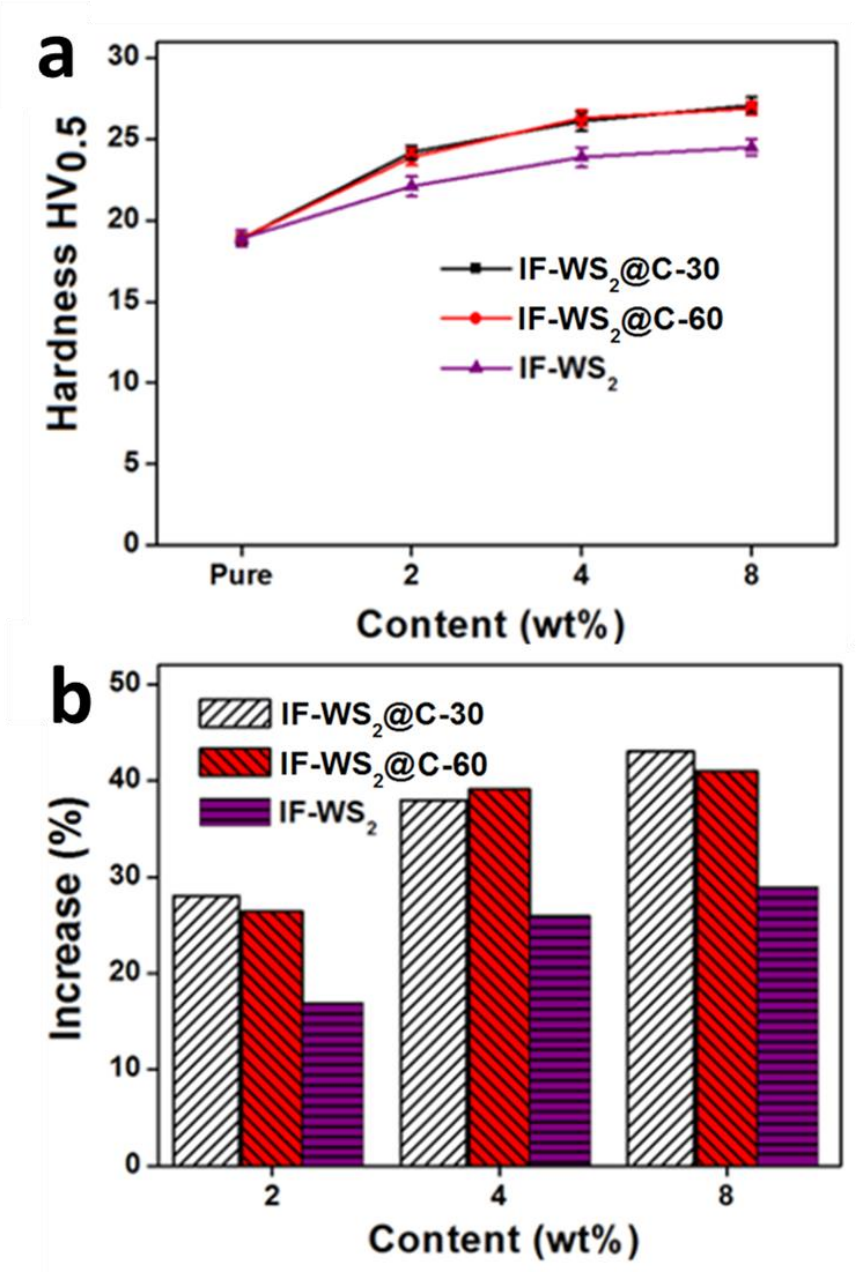

Fig. 7.11 Vickers hardness values of the specimens with different filler types and contents.

7.4 Conclusion

In summary, a novel and unique high performance thermoplastic PEEK ternary nanocomposites reinforced by nano graphitic C-coated IF-WS_2 NPs has been prepared by taking advantage of the excellent properties of both a few layered graphitic carbon and IF-WS_2. For the composites, their thermal conductivity (235%) and mechanical properties (>50% in strength and >40% in hardness) have been significantly improved. In addition, for the higher IF-WS_2@C content composites, they also exhibit higher decomposing temperatures, which implies the more stable thermal property (about 60°C). Further investigations have obtained the activation energies based on estimation by the Kissinger method being 61 and 97 $kJ \cdot mol^{-1}$ for neat PEEK and IF-WS_2@C-PEEK respectively. In addition, the interface structures have been characterised by electron microscopy imaging, EDS and XPS *etc.* We have verified that the C coating on the IF-WS_2 NPs allowed them to form a very good interface bonding when they were integrated into the PEEK matrix. At the meantime, the incorporation of the C coating also improved the dispersion ability of the IF-WS_2 NPs, further refined the crystallisation of the PEEK matrix with smaller cores by comparing the morphology change in SEM and TEM images, and promoted the formation of smaller spherulite structures, which have all contributed to the property improvements.

This study has not only established a completely new strategy to create carbon-inorganic jointly reinforced high performance polymeric matrix composite, but also has pointed out that coatings of other functional NPs could easily be realised for desired properties. This advanced IF-WS_2@C-PEEK ternary nanocomposites the significantly improved properties will greatly extend the applications of neat PEEK into more critical areas.

Chapter 8. Conclusions and future work

In conclusion, a series of nanoscale C-coated NPs has been prepared by the modified RCVDs method, and several types of polymer-based nanocomposites have been fabricated by a simple solution mixing technique, by applying the NPs created in this thesis. Their morphology, structure, mechanical, thermal and interface bonding properties have been thoroughly characterized.

In Chapters 4, we have described the general and simple method for the successful synthesis of the novel and uniform nanoscale C-coating deposited on the surface of various micro- or nanoscale non-magnetic metal oxides, including MO_x (M = Ce, Cr, Zr, Y, Ti and Zn, where x = 1, 1.5 and 2). The nearly individually and ultra-thin graphitic C-coating is 1-5 nm thick, reacted from 15 to 60 min, respectively. The resulting core-shell composite NPs have indeed combined the advantages of both graphitic carbon and metal oxides, benefiting their surface modification and dispersion in composite fabrication. And the optimal set of parameters have been obtained, as follows: acetone and styrene solutions with a volume ratio of 4:1 and the reaction temperature at 775 ^oC. We believe that the modified RCVD system is capable of scale-up MOx@C NPs manufacture to industrial level. For the TiO_2@C NPs, it changed from isolated material (TiO_2) into conductor, with the conductivity σ about 0.0891 S/m.

Further investigation in Chapter 5 is using ZnO@C NPs as an example filler in nylon 12 matrix and demonstrated the simple way to get the optimal crystallinity of polymer composite matrix is cooling down the samples on the surface of asbestos. The composite has shown that the C-coating has led to a 49% improvement in thermal conductivity (at 8 wt%), 27% increase in tensile strength (at 2 wt%) and around 28% reinforcement in hardness (at 8 wt%). This research opens up new opportunities for MO_X@C core-shell NPs to be utilised in the creation of high performance polymeric nanocomposites with specifically desirable functions based on the properties of cores.

In Chapter 6, we have successfully prepared high performance PEEK matrix polymer nanocomposite using IF-WS_2 NPs, by a simple melting process without

changing the basic structure of the original polymer matrix, and have shown the significant mechanical property improvements, where the tensile strength improved 24% (with 2 wt%, 96.7 MPa), the hardness displayed the highest increase of approximately 33% (25.1 $HV_{0.5}$ at 8 wt%) and the Young's modulus increased around 27% around 1.82GPa at 2 wt%.The XPS and FTIR results demonstrate how the IF-WS_2 NPs can be integrated within the polymer matrix with related strong chemical bonding, and also improve the way to dispersal and adhere the nanoparticles into the PEEK powder with high amount. Besides, we present the significant improvement in thermal conductivity of 190% (with 8 wt%). Moreover, for the thermal stability, the melting and degradation points have increased 49 and 54 ^{o}C, respectively (with 8 wt%).

In Chapter 7, we have successfully fabricated the novel IF-WS_2@C-PEEK ternary nanocomposites, validated the advantage of the C-coating in composite applications. The C-coating on the IF-WS_2 NPs helps to form a uniform dispersion, and eliminate the tendency of agglomeration in the PEEK matrix. The IF-WS_2@C-PEEK nanocomposites exhibit impressive improvements in both the mechanical and the thermal properties, with extraordinary 54% enhancement in the ultimate tensile strength at 2 wt% and nearly 235% increase in thermal conductivity at 8 wt%. In addition, they also show an increase in decomposing temperature (over 50 ^{o}C) at higher IF-WS_2@C contents. Further investigation reveals that the activation energies estimated by Kissinger method to be 61 and 97 kJ·mol^{-1} for neat PEEK and IF-WS_2@C-PEEK, respectively. The cause of better thermal stability has been confirmed by the stronger formation between PEEK matrix and IF-WS_2@C nanoparticles, which also for the first time has been investigated by FTIR and XPS analysis. This new strategy opens vast opportunities to combine the advantages of advanced polymer material and numerous NPs in a composite.

Based on above results, some thoughts can be proposed for the further work. These recommendations have not been accomplished in this thesis.

The surface modification of the C-coating is a very interesting field, because this method creates the opportunity to combine the large amounts of existing researches of carbon with countless non-magnetic nanoparticles together. I believe that this can provide a powerful tool for achieving novel ternary nanocomposites.

Moreover, the nanoscale C-coating process can be a decent method for the synthesis of uniform carbon membrane. The novel hollow carbon membrane with large surface area could be applied to prepare electrode materials for batteries/supercapacitors or basic substrates for super-catalyst in electrochemistry applications.

Last but not the least, even the mechanical and thermal properties are improved, the tribological properties of these IF-WS_2 composites still need further investigations to find out the mechanisms such as how to control the release of IF-WS_2 NPs onto the composite surface, to form a tribo-film. And extensive research is required to identify the optimal conditions of these ternary nanocomposites for anti-wear applications.

References

1. H. Kroto, *J. Mol. Graph. Model.*, 2001, **19**, 187-188.
2. H. W. Kroto, A. W. Allaf and S. P. Balm, *Chem. Rev.*, 1991, **91**, 1213-1235.
3. H. W. Kroto, J. R. Heath, S. C. O'Brien, R. F. Curl and R. E. Smalley, *Nature*, 1985, **318**, 162.
4. V. Georgakilas, J. A. Perman, J. Tucek and R. Zboril, *Chem. Rev.*, 2015, **115**, 4744-4822.
5. J. Lu, P. S. E. Yeo, C. K. Gan, P. Wu and K. P. Loh, *Nat. Nanotechnolo.*, 2011, **6**, 247.
6. A. K. Geim and K. S. Novoselov, *Nat. Mater.*, 2007, **6**, 183.
7. L. Liu, G. Cao and X. Chen, *J. Nanomater.*, 2008, **2008**, 12.
8. S. Iijima, *Nature*, 1991, **354**, 56.
9. S. Bhaviripudi, E. Mile, S. A. Steiner, A. T. Zare, M. S. Dresselhaus, A. M. Belcher and J. Kong, *J. Am. Chem. Soc.*, 2007, **129**, 1516-1517.
10. X. Zhao, Y. Ando, Y. Liu, M. Jinno and T. Suzuki, *Phys. Revi. Lett.*, 2003, **90**, 187401.
11. K. S. Novoselov, A. K. Geim, S. V. Morozov, D. Jiang, Y. Zhang, S. V. Dubonos, I. V. Grigorieva and A. A. Firsov, *Science*, 2004, **306**, 666.
12. A. J. Mannix, X.-F. Zhou, B. Kiraly, J. D. Wood, D. Alducin, B. D. Myers, X. Liu, B. L. Fisher, U. Santiago, J. R. Guest, M. J. Yacaman, A. Ponce, A. R. Oganov, M. C. Hersam and N. P. Guisinger, *Science*, 2015, **350**, 1513.
13. B. Radisavljevic, A. Radenovic, J. Brivio, V. Giacometti and A. Kis, *Nat. Nanotechnol.*, 2011, **6**, 147.
14. Y. Gong, Z. Wei, J. Wang, P. Zhang, H. Li and Y. Wang, *Sci. Rep-UK*, 2014, **4**, 6349.
15. S. H. Joo, S. J. Choi, I. Oh, J. Kwak, Z. Liu, O. Terasaki and R. Ryoo, *Nature*, 2001, **412**, 169.
16. Y. Li, C. Zhou, X. Xie, G. Shi and L. Qu, *Carbon*, 2010, **48**, 4190-4196.
17. S. Rhee and J. L. White, *J. Polym. Sci. B Polym. Phys.*, 2002, **40**, 1189-1200.
18. S. Yang, J. Rafael Castilleja, E. V. Barrera and K. Lozano, *Polym. Degrad. Stabil.*, 2004, **83**, 383-388.
19. B. Chen and J. R. G. Evans, *Soft Matter*, 2009, **5**, 3572-3584.
20. M. Kaseem, K. Hamad and Y. G. Ko, *Eur. Polym. J.*, 2016, **79**, 36-62.
21. B. J. P. Adohi, C. Brosseau, V. Laur and B. Haidar, *Appl. Phys. Lett.*, 2017, **110**.
22. H. J. Kim, K. Zhang, J.-M. Choi, M. S. Song and J. H. Park, *Chem. Commun.*, 2014, **50**, 2589-2591.
23. O. M. J. van 't Erve, A. T. Hanbicki, A. L. Friedman, K. M. McCreary, E. Cobas, C. H. Li, J. T. Robinson and B. T. Jonker, *J. Materi. Res.*, 2016, **31**, 845-877.
24. R. Tenne, L. Margulis, M. Genut and G. Hodes, *Nature*, 1992, **360**, 444-446.
25. L. Rapoport, Y. Feldman, M. Homyonfer, H. Cohen, J. Sloan, J. L. Hutchison and R. Tenne, *Wear*, 1999, **225–229, Part 2**, 975-982.
26. L. Rapoport, N. Fleischer and R. Tenne, *Adv. Mater.*, 2003, **15**, 651-655.
27. Y. Q. Zhu, T. Sekine, K. S. Brigatti, S. Firth, R. Tenne, R. Rosentsveig, H. W. Kroto and D. R. M. Walton, *J. Am. Chem. Soc.*, 2003, **125**, 1329-1333.
28. B. Mahler, V. Hoepfner, K. Liao and G. A. Ozin, *J. Am. Chem. Soc.*, 2014, **136**, 14121-14127.
29. R. L. D. Whitby, W. K. Hsu, C. B. Boothroyd, P. K. Fearon, H. W. Kroto and D. R. M. Walton, *ChemPhysChem*, 2001, **2**, 620-623.
30. N. W. Fang Xu, Hong Chang, Yongde Xia and Yanqiu Zhu *Inorganics* 2014, **2(2)**, 313-333.
31. F. Xu, T. P. Almeida, H. Chang, Y. Xia, M. L. Wears and Y. Zhu, *Nanoscale*, 2013, **5**, 10504-10510.
32. N. Wang, Z. Yang, K. Thummavichai, F. Xu, C. Hu, H. Chen, Y. Xia and Y. Zhu, *RSC Adv.*, 2017, **7**, 35265-35273.

33. K. Thamaphat, P. Limsuwan and B. Ngotawornchai, *Kasetsart.J.(Nat. Sci.).* 2008, **42**, 357-361.
34. J. Wang, T. Tsuzuki, B. Tang, X. Hou, L. Sun and X. Wang, *ACS Appl. Mater. Inter.*, 2012, **4**, 3084-3090.
35. D. Guo, Y. Lu, Y. Zhao and X. Zhang, *RSC Adv.*, 2015, **5**, 11738-11744.
36. P. Chu, H. Liu, Y. Li, H. Zhang and J. Li, *Ceram. Int.*, 2016, **42**, 17053-17058.
37. Y. B. Zhou, J. F. Sun, S. C. Wang and H. J. Zhang, *Corros. Sci.*, 2012, **63**, 351-357.
38. M. S. Hassan, T. Amna, S. S. Al-Deyab, H.-C. Kim, T.-H. Oh and M.-S. Khil, *Colloids Surfaces A*, 2012, **415**, 268-273.
39. C. Xiang, M. Li, M. Zhi, A. Manivannan and N. Wu, *J. Power Sources*, 2013, **226**, 65-70.
40. L. Yang, T. Huang, X. Jiang, J. Li and W. Jiang, *RSC Adv.*, 2016, **6**, 55135-55143.
41. L. Y. Yang, H. Z. Li, J. Liu, Z. Q. Sun, S. S. Tang and M. Lei, *Sci. Rep-UK*, 2015, **5**, 10908.
42. U. Kazuyuki, O. Susumu, S. Kenji and O. Atsushi, *J. Phys-Condens. Mat.*, 2007, **19**, 365218.
43. H. Khurshid, C. G. Hadjipanayis, H. Chen, W. Li, H. Mao, R. Machaidze, V. Tzitzios and G. C. Hadjipanayis, *J. Magn. Magn.c Mater.*, 2013, **331**, 17-20.
44. R. Verdejo, M. M. Bernal, L. J. Romasanta and M. A. Lopez-Manchado, *J. Mater. Chem.*, 2011, **21**, 3301-3310.
45. B. K. Dash, P. G. R. Achary, N. C. Nayak and R. N. P. Choudhary, *J. Electron. Mater.*, 2017, **46**, 563-572.
46. S. Mondal, L. Nayak, M. Rahaman, A. Aldalbahi, T. K. Chaki, D. Khastgir and N. C. Das, *Compos. Part B-Eng.*, 2017, **109**, 155-169.
47. S. Pourhashem, M. R. Vaezi, A. Rashidi and M. R. Bagherzadeh, *Corros. Sci.*, 2017, **115**, 78-92.
48. W. W. Yu, J. G. Shi and L. M. Wang, *J. Appl. Polym. Sci.*, 2017, **134**.
49. C. Ozkan, N. Gamze Karsli, A. Aytac and V. Deniz, *Compos. Part B-Eng.*, 2014, **62**, 230-235.
50. L. Ji, Z. Lin, M. Alcoutlabi and X. Zhang, *Energ. Environ. Sci.*, 2011, **4**, 2682-2699.
51. A. Ponrouch, A. R. Goni, M. T. Sougrati, M. Ati, J.-M. Tarascon, J. Nava-Avendano and M. R. Palacin, *Energ. Environ. Sci.*, 2013, **6**, 3363-3371.
52. M. S. Ata, Y. Liu and I. Zhitomirsky, *RSC Adv.*, 2014, **4**, 22716-22732.
53. J.-K. Kim, D.-S. Kim, D.-H. Lim, A. Matic, G. S. Chauhan and J.-H. Ahn, *Solid State Ionics*, 2014, **262**, 25-29.
54. J. Liu, Y. Xu, X. Ma, J. Feng, Y. Qian and S. Xiong, *Nano Energy*, 2014, **7**, 52-62.
55. A. Kalendova, D. Vesely and P. Nemec, *Mater. Res. Innov.*, 2009, **13**, 288-290.
56. D. W. Lee and B. R. Yoo, *J. Ind. Eng. Chem.*, 2014, **20**, 3947-3959.
57. C. Wang, L. Yin, L. Zhang, D. Xiang and R. Gao, *Sensors-Basel*, 2010, **10**, 2088-2106.
58. L. Petti, N. Münzenrieder, C. Vogt, H. Faber, L. Büthe, G. Cantarella, F. Bottacchi, T. D. Anthopoulos and G. Tröster, *Appl. Phys. Rev.*, 2016, **3**, 021303.
59. J. P. Petropoulos, T. R. Cristiani, P. B. Dongmo and J. M. O. Zide, *Nanotechnology*, 2011, **22**, 245704.
60. S. Chatterjee, F. Nafezarefi, N. Tai, L. Schlagenhauf, F. Nüesch and B. Chu, *Carbon*, 2012, **50**, 5380-5386.
61. L. Van Thu, N. Cao Long, L. Quoc Trung, N. Trinh Tung, N. Duc Nghia and V. Minh Thanh, *Adv. Nat. Sci: Nanosci. Nanotechnol.*, 2013, **4**, 035017.
62. R. Shah, A. Kausar, B. Muhammad and S. Shah, *Polym-Plast. Technol.*, 2015, **54**, 173-183.
63. S. Talam, S. R. Karumuri and N. Gunnam, *ISRN Nanotechnology*, 2012, **2012**, 6.
64. H. Nakano, K. Dokko, S. Koizumi, H. Tannai and K. Kanamura, *J. Electrochem. Soc.*, 2008, **155**, A909-A914.
65. S. P. Somani, P. R. Somani, M. Noda and M. Umeno, *Diam. Relat. Mater.*, 2008, **17**, 576-580.

66. M. Bystrzejewski, K. Pyrzyńska, A. Huczko and H. Lange, *Carbon*, 2009, **47**, 1201-1204.
67. J. Nie, W. Qian, Q. Zhang, Q. Wen and F. Wei, *J. Phys. Chem. C.*, 2009, **113**, 20178-20183.
68. A. Barroso-Bogeat, M. Alexandre-Franco, C. Fernández-González and V. Gómez-Serrano, *Fuel. Process. Technol.*, 2014, **126**, 95-103.
69. D. W. McKee, *Carbon*, 1970, **8**, 623-635.
70. Z.-S. Wu, G. Zhou, L.-C. Yin, W. Ren, F. Li and H.-M. Cheng, *Nano Energy*, 2012, **1**, 107-131.
71. D.-H. Yang, C. S. Park, J. H. Min, M.-H. Oh, Y. S. Yoon, S.-W. Lee and J. S. Shin, *Curr. Appl.Phys.*, 2009, **9**, e132-e135.
72. E. Flahaut, A. Peigney, C. Laurent, C. Marlière, F. Chastel and A. Rousset, *Acta. Mater.*, 2000, **48**, 3803-3812.
73. M. Inagaki, H. Miura and H. Konno, *J. Eur. Ceram.Soci.*, 1998, **18**, 1011-1015.
74. S. Yahachi, O. Mitsumasa, F. Naoya, Y. Tadanobu, T. Masato and H. Takayoshi, *Jap. J. Appl. Phys.*, 1994, **33**, L526.
75. Y. Su, S. Li, D. Wu, F. Zhang, H. Liang, P. Gao, C. Cheng and X. Feng, *ACS Nano*, 2012, **6**, 8349-8356.
76. Y. Hu and C. Guo, in *Carbon Nanotubes - Growth and Applications*, ed. D. M. Naraghi, InTech, Rijeka, 2011, DOI: 10.5772/16463, p. Ch. 01.
77. S. Banerjee, T. Hemraj-Benny and S. S. Wong, *Adv. Mater.*, 2005, **17**, 17-29.
78. P. M. Ajayan, O. Stephan, P. Redlich and C. Colliex, *Nature*, 1995, **375**, 564.
79. B. C. Satishkumara., A. Govindarajab., M. Natha. and C. N. R. Rao., *J. Mater. Chem.*, 2000, **10**, 2115-2119.
80. N. Abbas and H. T. Kim, *Macromol. Res.*, 2016, **24**, 1084-1090.
81. K. Inoue and S. Hoshino, *J. Polym. Sci. B Polym. Phys.*, 1973, **11**, 1077-1089.
82. L. J. Mathias and C. G. Johnson, *Macromolecules*, 1991, **24**, 6114-6122.
83. S. M. Aharoni, *n-Nylons: Their synthesis, structure and properties*, John Wiley & Sons, Inc., Chichester, New York, 1997.
84. C. Ramesh, *Macromolecules*, 1999, **32**, 5704-5706.
85. N. Dilsiz, *J. Adhes. Sci. Technol.*, 2000, **14**, 975-987.
86. P. Poizot, S. Laruelle, S. Grugeon, L. Dupont and J. M. Tarascon, *Nature*, 2000, **407**, 496-499.
87. S. Laurent, J.-L. Bridot, L. V. Elst and R. N. Muller, *Future. Med. Chem.*, 2010, **2**, 427-449.
88. V. Kruefu, A. Wisitsoraat, A. Tuantranont and S. Phanichphant, *Nanoscale. Res. Lett.*, 2014, **9**, 467-467.
89. M. V. Reddy, G. V. Subba Rao and B. V. R. Chowdari, *Chem. Rev.*, 2013, **113**, 5364-5457.
90. Z. Zhang, J. Liu, J. Gu, L. Su and L. Cheng, *Energ. Environ. Sci.*, 2014, **7**, 2535-2558.
91. K. Ketpang, K. Lee and S. Shanmugam, *ACS Appl. Mater. Inter.*, 2014, **6**, 16734-16744.
92. H. W. Gibson, *J. Am. Chem. Soc.*, 2010, **132**, 9929-9930.
93. N. Raman, S. Sudharsan and K. Pothiraj, *J. Saudi. Chem. Soc.*, 2012, **16**, 339-352.
94. S. Musikhin, L. Bakueva, E. H. Sargent and A. Shik, *J. Appl. Phys.*, 2002, **91**, 6679-6683.
95. Z. G. Wang, X. T. Zu, X. Xiang, J. Lian and L. M. Wang, *J. Mater. Sci.*, 2006, **41**, 1973-1978.
96. Z.-Y. Zhang, Y.-D. Xu, Y.-Y. Ma, L.-L. Qiu, Y. Wang, J.-L. Kong and H.-M. Xiong, *Angew. Chem. Int. Edit.*, 2013, **52**, 4127-4131.
97. D. Vollath and D. V. Szabó, *J. Nanopart. Res.*, 2006, **8**, 417-428.
98. H. Srikanth, R. Hajndl, C. Chirinos, J. Sanders, A. Sampath and T. S. Sudarshan, *Appl. Phys. Lett.*, 2001, **79**, 3503-3505.
99. C. Qin and S. Coulombe, *Mater. Lett.*, 2006, **60**, 1973-1976.
100. L. Martinů, H. Biederman and J. Zemek, *Vacuum*, 1985, **35**, 171-176.
101. H. Althues, R. Palkovits, A. Rumplecker, P. Simon, W. Sigle, M. Bredol, U. Kynast and S. Kaskel, *Chem. Mater.*, 2006, **18**, 1068-1072.

102. R. F. Ziolo, E. P. Giannelis, B. A. Weinstein, M. P. Horo, B. N. Ganguly, V. Mehrotra, M. W. Russell and D. R. Huffman, *Science*, 1992, **257**, 219.
103. Z. Cao, W. Jiang, X. Ye and X. Gong, *J. Magn. Magn. Mater.*, 2008, **320**, 1499-1502.
104. C. Guan, C. Lu, Y. Cheng, S. Song and B. Yang, *J. Mater. Chem.*, 2009, **19**, 617-621.
105. H. Dislich, *Angew. Chem. Int. Edit.*, 1971, **10**, 363-370.
106. J. H. Fendler, *Korean J. Chem. Eng.*, 2001, **18**, 1-13.
107. C.-C. Chang and W.-C. Chen, *Chem. Mater.*, 2002, **14**, 4242-4248.
108. M. Xiong, S. Zhou, B. You and L. Wu, *J. Polym. Sci. Pol. Phys.*, 2005, **43**, 637-649.
109. P. A. Hartley, G. D. Parfitt and L. B. Pollack, *Powder. Technol.*, 1985, **42**, 35-46.
110. R. A. Sullivan, *JOM*, 2006, **58**, 77-79.
111. G. M. Jenkins and F. X. de Carvalho, *Carbon*, 1977, **15**, 33-37.
112. Y. N. Rabotnov, A. A. Tupolev, V. F. Kut'inov, V. P. Kogaev, A. V. Berezin and V. V. Sulimenkov, *Mech. Compos. Mater.*, 1982, **17**, 455-465.
113. G. Williams, R. Trask and I. Bond, *Compos. Part A-Appl. S.*, 2007, **38**, 1525-1532.
114. Y. F. Khalil, *Sustain. Product. Consum.*, 2017, **12**, 16-26.
115. S. Bal and S. S. Samal, *B. Mater. Sci.*, 2007, **30**, 379.
116. S. Coiai, E. Passaglia, A. Pucci and G. Ruggeri, *Materials*, 2015, **8**, 3377.
117. Y. Liu and S. Kumar, *ACS Appl. Mater. Inter.*, 2014, **6**, 6069-6087.
118. S.-L. Yeh, C.-Y. Zhu and S.-W. Kuo, *Polymers*, 2015, **7**.
119. P. M. Ajayan, O. Stephan, C. Colliex and D. Trauth, *Science*, 1994, **265**, 1212.
120. V. Choudhary. and A. Gupta., *Polymer Nanocomposites*, 2011, DOI: 10.5772/18423.
121. J. R. Potts, D. R. Dreyer, C. W. Bielawski and R. S. Ruoff, *Polymer*, 2011, **52**, 5-25.
122. T. Kuilla, S. Bhadra, D. Yao, N. H. Kim, S. Bose and J. H. Lee, *Prog. Polym. Sci.*, 2010, **35**, 1350-1375.
123. S. Chatterjee, J. W. Wang, W. S. Kuo, N. H. Tai, C. Salzmann, W. L. Li, R. Hollertz, F. A. Nüesch and B. T. T. Chu, *Chem. Phys. Lett.*, 2012, **531**, 6-10.
124. E. Pop, V. Varshney and A. K. Roy, *MRS Bull.*, 2012, **37**, 1273-1281.
125. J. Jin, R. Rafiq, Y. Q. Gill and M. Song, *Eur. Polym. J.*, 2013, **49**, 2617-2626.
126. F. Wang, J. Yi, Y. Wang, C. Wang, J. Wang and Y. Xia, *Adv. Energy Mater.*, 2014, **4**, n/a-n/a.
127. M. Bockrath, D. H. Cobden, P. L. McEuen, N. G. Chopra, A. Zettl, A. Thess and R. E. Smalley, *Science*, 1997, **275**, 1922.
128. A. R. Beal and W. Y. Liang, *J. Phys-Condens. Mat*, 1976, **9**, 2459.
129. H. S. S. Ramakrishna Matte, A. Gomathi, A. K. Manna, D. J. Late, R. Datta, S. K. Pati and C. N. R. Rao, *Angew. Chem. Int. Edit.*, 2010, **49**, 4059-4062.
130. A. Margolin, R. Rosentsveig, A. Albu-Yaron, R. Popovitz-Biro and R. Tenne, *J. Mater. Chem.*, 2004, **14**, 617-624.
131. R. Tenne, *Angew. Chem. Int. Edit.*, 2003, **42**, 5124-5132.
132. S. M. Ghoreishi, S. S. Meshkat and A. A. Dadkhah, *Mater. Res. Bull.*, 2010, **45**, 584-588.
133. R. Tenne, *J. Mater. Res.*, 2006, **21**, 2726-2743.
134. A. Margolin, F. L. Deepak, R. Popovitz-Biro, M. Bar-Sadan, Y. Feldman and R. Tenne, *Nanotechnology*, 2008, **19**, 095601.
135. Y. Feldman, G. L. Frey, M. Homyonfer, V. Lyakhovitskaya, L. Margulis, H. Cohen, G. Hodes, J. L. Hutchison and R. Tenne, *J. Am. Chem. Soc.*, 1996, **118**, 5362-5367.
136. Y. Feldman, A. Zak, R. Popovitz-Biro and R. Tenne, *Solid State Sci.*, 2000, **2**, 663-672.
137. R. Tenne, *Journal of Materials Research*, 2006, **21**, 2726-2743.
138. F. Xu, N. Wang, H. Chang, Y. Xia and Y. Zhu, *Inorganics*, 2014, **2**, 313.
139. J. W. Chung, Z. R. Dai and F. S. Ohuchi, *J. Cryst. Growth*, 1998, **186**, 137-150.
140. W. Ho, J. C. Yu, J. Lin, J. Yu and P. Li, *Langmuir*, 2004, **20**, 5865-5869.
141. M. E. Sarah, C. Víctor Oliveros, N. Yifan, C. Kyeongjae and A. R. Joshua, *2D Materials*, 2016, **3**, 025015.

142. K. E. Aretouli, P. Tsipas, D. Tsoutsou, J. Marquez-Velasco, E. Xenogiannopoulou, S. A. Giamini, E. Vassalou, N. Kelaidis and A. Dimoulas, *Appl. Phys. Lett.*, 2015, **106**, 143105.
143. L. Liu, H. Qiu, J. Wang, G. Xu and L. Jiao, *Nanoscale*, 2016, **8**, 4486-4490.
144. D. Wang, Z. Pan, Z. Wu, Z. Wang and Z. Liu, *J. Power Sources*, 2014, **264**, 229-234.
145. Y. Sun, S. Wang and Q. Wang, *Front. Chem.*, 2009, **4**, 173-176.
146. Y. M. Zhao, W. B. Hu, Y. D. Xia, E. F. Smith, Y. Q. Zhu, C. W. Dunnill and D. H. Gregory, *J. Mater. Chem.*, 2007, **17**, 4436-4440.
147. O. Tevet, O. Goldbart, S. R. Cohen, R. Rosentsveig, R. Popovitz-Biro, H. D. Wagner and R. Tenne, *Nanotechnology*, 2010, **21**, 365705.
148. O. Tevet, P. Von-Huth, R. Popovitz-Biro, R. Rosentsveig, H. D. Wagner and R. Tenne, *PNAS*, 2011, **108**, 19901.
149. Y. Q. Zhu, T. Sekine, K. S. Brigatti, S. Firth, R. Tenne, R. Rosentsveig, H. W. Kroto and D. R. Walton, *J. Am. Chem. Soc.*, 2003, **125**, 1329-1333.
150. Y. Q. Zhu, T. Sekine, Y. H. Li, W. X. Wang, M. W. Fay, H. Edwards, P. D. Brown, N. Fleischer and R. Tenne, *Adv. Mater.*, 2005, **17**, 1500-1503.
151. Y. Q. Zhu, T. Sekine, Y. H. Li, M. W. Fay, Y. M. Zhao, C. H. Patrick Poa, W. X. Wang, M. J. Roe, P. D. Brown, N. Fleischer and R. Tenne, *J. Am. Chem. Soc.*, 2005, **127**, 16263-16272.
152. B. Peng, H. Zhang, H. Shao, Y. Xu, X. Zhang and H. Zhu, *RSC Adv.*, 2016, **6**, 5767-5773.
153. M. Yuzuru, O. Hidenori and K. Tsuyoshi, *Jap. J. Appl. Phys.*, 2004, **43**, L1202.
154. A. D. Schwitalla, T. Spintig, I. Kallage and W.-D. Mueller, *Dent. Mater.*, 2015, **31**, 1377-1384.
155. Y. Wang, E. James and O. R. Ghita, *Mater. Desgin.*, 2015, **83**, 545-551.
156. G. Zhang, H. Liao, H. Li, C. Mateus, J. M. Bordes and C. Coddet, *Wear*, 2006, **260**, 594-600.
157. Y. Wang, J. D. Beard, K. E. Evans and O. Ghita, *RSC Adv.*, 2016, **6**, 3198-3209.
158. A. M. Díez-Pascual, M. Naffakh, M. A. Gómez, C. Marco, G. Ellis, M. T. Martínez, A. Ansón, J. M. González-Domínguez, Y. Martínez-Rubi and B. Simard, *Carbon*, 2009, **47**, 3079-3090.
159. A. Tewatia, J. Hendrix, Z. Dong, M. Taghon, S. Tse, G. Chiu, W. E. Mayo, B. Kear, T. Nosker and J. Lynch, *Mater. Sci. Eng. B*, 2017, **216**, 41-49.
160. A. M. Diez-Pascual and A. L. Diez-Vicente, *ACS Appl. Mater. Inter.*, 2014, **6**, 3729-3741.
161. A. M. Díez-Pascual and A. L. Díez-Vicente, *ACS Appl. Mater. Inter.*, 2015, **7**, 5561-5573.
162. M. Naffakh and A. M. Diez-Pascual, *J. Mater. Chem. B*, 2014, **2**, 4509-4520.
163. X. Hou, C. X. Shan and K. Choy, *Surf. Coat. Tech.*, 2008, **202**, 2287-2291.
164. M. Naffakh, A. M. Díez-Pascual, C. Marco, G. J. Ellis and M. A. Gómez-Fatou, *Prog. Polym. Sci.*, 2013, **38**, 1163-1231.
165. M. E. Fitzpatrick, A. T. Fry, P. Holdway, F. A. Kandil, J. Shackleton and L. Suominen, *Determination of residual stresses by X-ray diffraction*, National Physical Laboratory, Teddington, UK, 2005.
166. Y. Joly, S. D. Matteo and O. Bunău, *The European Physical Journal Special Topics*, 2012, **208**, 21-38.
167. A. Argast and C. F. Tennis, *J. Geo. Edu.*, 2004, **52**, 213-217.
168. R. J. Beane, *J. Geo. Edu.*, 2004, **52**, 250-253.
169. R. M. Brydson and C. Hammond, in *Nanoscale Science and Technology*, John Wiley & Sons, Ltd, 2005, DOI: 10.1002/0470020873.ch2, pp. 56-129.
170. P. Silvester, *Journal*, 1968, **115**, 43-48.
171. P. Larkin, in *Infrared and Raman Spectroscopy*, Elsevier, Oxford, 2011, DOI: https://doi.org/10.1016/B978-0-12-386984-5.10006-0, pp. 73-115.
172. W. L. Peticolas, *Biochimie*, 1975, **57**, 417-428.
173. P. V. Huong, *Vibra. Spec.*, 1996, **11**, 17-28.

174. P. Liang, H. Wang, C. Chen, F. Ge, D. Liu, S. Li, B. Han, X. Xiong and S. Zhao, *Journal of Spectroscopy*, 2013, **2013**, 6.
175. W. Mäntele, in *Biophysical Techniques in Photosynthesis*, eds. J. Amesz and A. J. Hoff, Springer Netherlands, Dordrecht, 1996, DOI: 10.1007/0-306-47960-5_9, pp. 137-160.
176. N. Lee, S. H. Choi and T. Hyeon, *Adv. Mater.*, 2013, **25**, 2641-2660.
177. Y. F. Dufrêne, *J. Bacteriol.*, 2002, **184**, 5205-5213.
178. J. D. Andrade, in *Surface and Interfacial Aspects of Biomedical Polymers: Volume 1 Surface Chemistry and Physics*, ed. J. D. Andrade, Springer US, Boston, MA, 1985, DOI: 10.1007/978-1-4684-8610-0_5, pp. 105-195.
179. L. D. S. Yadav, in *Organic Spectroscopy*, ed. L. D. S. Yadav, Springer Netherlands, Dordrecht, 2005, DOI: 10.1007/978-1-4020-2575-4_2, pp. 7-51.
180. E. A. G. Leonard, *Textile Research Journal*, 1970, **40**, 116-126.
181. J. H. Flynn, in *Analytical Calorimetry: Volume 3*, eds. R. S. Porter and J. F. Johnson, Springer US, Boston, MA, 1974, DOI: 10.1007/978-1-4757-4509-2_3, pp. 17-44.
182. H. Xie, M. Hu and H. Bao, *Appl. Phys. Lett.*, 2014, **104**, 131906.
183. J. A. Ruud, D. Josell, F. Spaepen and A. L. Greer, *J. Mater. Res.*, 1993, **8**, 112-117.
184. A. F. Mohrnheim, in *Interpretive Techniques for Microstructural Analysis*, eds. J. L. McCall and P. M. French, Springer US, Boston, MA, 1977, DOI: 10.1007/978-1-4684-2370-9_7, pp. 117-126.
185. C. Cui, W. Qian, C. Zheng, Y. Liu, S. Yun, Y. Yu, J. Nie and F. Wei, *Chem. Eng. J*, 2013, **223**, 617-622.
186. Z. Jin, H. Chu, J. Wang, J. Hong, W. Tan and Y. Li, *Nano Lett.*, 2007, **7**, 2073-2079.
187. A. C. Ferrari, *Solid State Commun.*, 2007, **143**, 47-57.
188. L. M. Malard, M. A. Pimenta, G. Dresselhaus and M. S. Dresselhaus, *Phys. Rep.*, 2009, **473**, 51-87.
189. A. M. Diez-Pascual, C. Xu and R. Luque, *Journal of Materials Chemistry B*, 2014, **2**, 3065-3078.
190. M. Kalin, M. Zalaznik and S. Novak, *Wear*, 2015, **332**, 855-862.
191. A. A. Balandin, S. Ghosh, W. Bao, I. Calizo, D. Teweldebrhan, F. Miao and C. N. Lau, *Nano Lett.*, 2008, **8**, 902-907.
192. M. Naffakh, A. M. Diez-Pascual, C. Marco and G. Ellis, *Mater. Chem. Phys.*, 2014, **144**, 98-106.
193. Y. Wang, D. Rouholamin, R. Davies and O. R. Ghita, *Mater. Desgin.*, 2015, **88**, 1310-1320.
194. M. Naffakh, A. M. Diez-Pascual, C. Marco, M. A. Gomez and I. Jimenez, *J. Phys. Chem. B*, 2010, **114**, 11444-11453.
195. T. Wu, P. Liu, M. Shi, J. Lu, G. Ye and J. Xu, *Polym. Int.*, 2011, **60**, 1318-1323.
196. F. Xu, T. Kobayashi, Z. Yang, T. Sekine, H. Chang, N. Wang, Y. Xia and Y. Zhu, *ACS Nano*, 2017, DOI: 10.1021/acsnano.7b02943.
197. F. Xu, C. Yan, Y.-T. Shyng, H. Chang, Y. Xia and Y. Zhu, *Nanotechnology*, 2014, **25**, 325701.
198. J. M. O'Reilly and R. A. Mosher, *Carbon*, 1983, **21**, 47-51.
199. L. O. Dandy, G. Oliveux, J. Wood, M. J. Jenkins and G. A. Leeke, *Polym. Degrad. Stabil.*, 2015, **112**, 52-62.
200. P. Louette, F. Bodino and J.-J. Pireaux, *Surf. Sci. Spec.*, 2005, **12**, 149-153.
201. H. E. Kissinger, *Anal. Chem.*, 1957, **29**, 1702-1706.
202. G. Zhang, S. Guessasma, H. Liao, C. Coddet and J. M. Bordes, *Surf. Coat. Tech.*, 2006, **200**, 2610-2617.
203. W. Zhang, S. Ge, Y. Wang, M. H. Rafailovich, O. Dhez, D. A. Winesett, H. Ade, K. Shafi, A. Ulman, R. Popovitz-Biro, R. Tenne and J. Sokolov, *Polymer*, 2003, **44**, 2109-2115.
204. C. Jama, O. Dessaux, P. Goudmand, L. Gengembre and J. Grimblot, *Surf. Interface. Anal.*, 1992, **18**, 751-756.

205. S. Grimme, *Angew. Chem. Int. Edit.*, 2008, **47**, 3430-3434.